THE AUSTRALIAN NATIONAL UNIVERSITY

Hot Melt Extrusion of Carbon Fiber Reinforced Thermoplastic Composites for Injection Molding and Fused Deposition Modeling

By

Chao Hu

A thesis submitted for the degree of

Doctor of Philosophy

Of The Australian National University

12th of June 2020

Big things have small beginnings.

---------*Prometheus*

DECLARATION

I certify that the written thesis is my own research work completed at the Research School of Engineering, The Australian National University. No portion of the work has been submitted in support of an application for another degree or diploma of this or any other university or other tertiary institution. To the best of my knowledge, no contents in this thesis has been published or written by another person, except where due reference is cited in the text.

Chao Hu

12/06/2020

DEDICATION

To my family, my mom, my dad, my grandma and to the loving memory of my grandpa

for ther unconditional care, love and support

ACKNOWLEDGEMENT

It is impossible to complete the research work during the PhD study if not from the support of a host of individuals. First and foremost, I would like to express sincere gratefulness to my primary supervisor Prof. Qinghua Qin for his patient guidance, constructive suggestions and continuous support. I grategully appreciate he provided me the precious opportunity to pursue my insterest in the field of high-performance fiber reinforced composites and can always help me find right solutions when I faced various challenges and problems during my research. Apart from being a great supervisor, Prof. Qin is also a very nice friend who cares about my feelings and can always give me assistance when I had difficulties in life. I can say I wouldn't be able to complete this project without his constant supervision. Words are just not enough to show my tremendous gratitude.

I would like to extend my appreciation to my PhD advisors: Assoc. Pof. Shankar Kalyanasundaram, Assoc. Pof. Adrian Lowe and Dr. Yi Xiao for their valuable advices and helpful discussions. It is a pleasure to acknowledge Dr. Hua Chen, Dr. Felipe Kremer, Ms. Joanne Lee and Ms. Josie Smith from the Center for Advanced Microscopy for their training and guidance in SEM operation and analysis. Great thanks are also given to Dr. Zbigniew Henryk Stachurski, Mr. Jason Chen, Mr. David Tychsen-Smith, Mr. Colin Carvolth and Mr. Bruce Condon from the Research School of Engineering for teaching me how to use various instruments, including industralized twin-screw extruder, 3D printers, universal testing machine, hardness testers, DSC, etc.

I would also like to give my special thanks to Prof. Shulin Bai from Peking University, Prof. Gang Wang from Shanghai University and Prof. Faxiang Qin from Zhejiang University for their support and assistance during the 3-month academic visit of my PhD period, where I learnt a lot of useful knowledge and skills for my research project.

I would like to thank all our members in the Materials and Manufacturing Group for their helpful advices in research, especially Cheuk Yu Lee, Bobin Xin, Yuan Chai, Jiaqi Dong and Haiyang Zhou.

Last but not the least, I would like to thank my family and all friends in my life for their endless support, encouragement and accompanying.

SUPERVISORY PANEL

Prof. Qinghua Qin, The Australian National University, Primary Supervisor, Chair of Panel

Assoc. Pof. Shankar Kalyanasundaram, The Australian National University, Advisor

Assoc. Pof. Adrian Lowe, The Australian National University, Advisor

LIST OF PUBLICATIONS

1. **Chao Hu** and Qinghua Qin. Advances in fused deposition modeling of discontinuous fiber/polymer composites. *Composites Science and Technology*, 24(5), 100867.

2. **Chao Hu**, Jiaqi Dong, Junjie Luo, Qing-Hua Qin and Guangyong Sun. 3D printing of chiral carbon fiber reinforced polylactic acid composites with negative Poisson's ratios. *Composties Part B: Engineering*, 201, 108400.

3. **Chao Hu** and Qinghua Qin. 2020. Bone remodeling and biological effects of mechanical stimulus. *AIMS Bioengineering*, 7(1), 12-28.

4. Lin Qiu, **Chao Hu** and Qing-Hua Qin. 2020. A novel homogenization function method for inverse source problem of nonlinear time-fractional wave equation. *Applied Mathematics Letters*, 109, 106554.

5. **Chao Hu**, Xinwen Liao, Qinghua Qin and Gang Wang. 2019. The fabrication and characterization of high density polyethylene composites reinforced by carbon nanotube coated carbon fibers. *Composites Part A: Applied Science and Manufacturing*, 121, pp.149-156.

6. **Chao Hu**, Deepu Ashok, David Nisbet and Vini Gautam. 2019. Bioinspired surface modification of orthopedic implants for bone tissue engineering. *Biomaterials*, 219, 119366.

7. **Chao Hu**, Zeyu Sun, Yi Xiao and Qinghua Qin. 2019. Recent patents in additive manufacturing of continuous fiber reinforced composites. *Recent Patents on Mechanical Engineering*, 12(1), pp.25-36.

8. Peng Wu, **Chao Hu** and Qinghua Qin. 2018. Time-dependent behavior of layered magneto-electro-elastic cylindrical shell with viscoelastic interlayer. *Composite Structures*, 200, pp.874-885.

9. **Chao Hu**, Winson NG Joon Hau, Weiqi Chen and Qing-Hua Qin. The fabrication of long carbon fiber reinforced polylactic acid composites via fused deposition modelling: experimental analysis and machine learning (submitted to *Journal of Composite Materials* on 31 May 2020; manuscript ID is JCM-20-0690).

ABSTRACT

Hot melt extrusion (HME) is a well-established industrial manufacturing technology predominantly in polymer-related industries. The HME machine can not only independently fabricate continuous sheets, tubes, and 3D printing filaments, but produce plastic parts like toys, spools, bottles and packages in association with other techniques such as injection molding, thermoforming and blow molding. As an important upstream process, this thesis is mainly central in HME to study the fabrication of carbon fiber (CF) reinforced thermoplastic composites by coupling with injection molding and fused deposition molding (FDM) techniques.

In this thesis work, a simple and economical surface treatment method was developed for the first time to modify the surface roughness of CF by spray coating with carbon nanotubes (CNT). Then, The CNT-coated CF was compounded, extruded and injection molded with high density polyethylene (HDPE) for hierarchical CNT-CF/HDPE composite fabrication. To evaluate the influence of CF contents and CNT coatings on the mechanical, thermal and morphological properties of the hierarchical composites, the CF content relative to the composites varying from 0-25 wt.% and 1 wt.% CNT coatings relative to CF were investigated in the research. The results showed that with the increase of CF content, all the evaluated properties including the tensile properties, flexural properties and hardness of CF/HDPE composites were effectively enhanced. Meanwhile, compared to uncoated composites, the CNT-spray coated counterparts have higher overall mechanical performance. The differential scanning calorimetry data indicated that the crystallization temperature and the crystallinity of HDPE was affected by the introduction of CF and CNT while the melting temperatures did not have apparent changes. An analysis of mechanical results combined with the morphological observation via scanning electron microscopy indicated that the interfacial bonding between CF and HDPE was improved by the incorporation of CNT.

The FDM fabrication of CF/polylactic acid (PLA) composites was studied by employing the HME-made PLA composite filaments with chopped long CF reinforcement (~4.6 mm) as the feedstock. By varying the loading quantity, the effect of CF contents on the mechanical, thermal and morphological properties of these 3D printed composites was thoroughly investigated. The results showed that with the increase of CF contents, all assessed properties of CF/PLA composites including tensile properties, flexural properties, hardness and thermal conductivity were effectively improved compared to the neat PLA. Their performance exhibited the same upward-downward-upward trend with the addition of CF. It can be attributed to the mutual influence generated from inter-/intra filament porosities and the high stiffness of CF. Meanwhile, a machine learning technique, Gaussian Process modelling was also introduced for the property prediction of the composites. In comparison with the experimental analysis, the optimal CF content of 6.7 wt% with best overall performance was predicted using this model, which was very close to the best experimental results at 5 wt% CF.

Auextic materials have gained great research interest by virtue of its various exotic mechanical properties while most of these metamaterials rely on the hollow cellular configuration, largely undermining the overall mechanical performance. In order to solve this issue, we first designed a new class of chiral structures by integrating various polynomial curves. Based on the state-of-the-art 3D printing technique, these auxetic geometries were then fabricated into high-performance composites with chopped carbon fiber (CF) as the reinforcement. Guided by experimental characterization and finite element analysis, the influences of the polynomial orders (n) and the incorporation of CF on the mechanical properties were systematically studied. Results show that the auxetic behavior can be tailored by varying the n value inside the polynomial equation. Moreover, the tensile modulus, strength and energy absorption at break of printed chiral samples were all enhanced with the addition of CF, especially for the large improvement of modulus and absorbed energy by 2-fold.

CONTENTS

LIST OF FIGURES

LIST OF TABLES

ACRONYMS

ABS	Acrylonitrile Butadiene Styrene
AE	Acoustic Emission
AM	Additive Manufacturing
ASTM	Amercian Society for Testing Material
BCR	Braided Composite Rod
CAD	Computer-Aid Design
CCD	Charge Coupled Device
CF	Carbon Fiber
CNT	Carbon Nanotube
CM	Compression Molding
CVD	Chemical Vapor Deposition
DFM	Design for Manufacturing
DFA	Design for Assembly
DIC	Digital Image Correlation
DSC	Differential Scanning Calorimetry
EPD	Electrophoretic Deposition
FDM	Fused Deposition Modeling
FEA	Finite Element Analysis
FFF	Fused Filament Fabrication
FRPC	Friber Reinforced Polymer Composite
GF	Glass Fiber
HDPE	High Density Polyethylene
HIPS	High Impact Polystyrene
HME	Hot Melt Extrusion
IM	Injection Molding
ISO	International Standardization Organization
LOM	Laminated Object Manufacturing

ML	Machine Learning
MTL	Material Template Library
MWCNT	Multi-Walled Carbon Nanotube
NPR	Negative Possion's Ratio
PA	Polyamide/nylon
PC	Polycarbonate
PCL	Polycaprolactone
PE	Polyethylene
PEEK	Poly Ether Ether Ketone
PEI	Polyeherimide
PEKK	Poly Ether Ketone Ketone
PET	Polyethylene Terephthalate
PLA	Polylactic Acid
PP	Polypropylene
PPS	Polyphenylene Sulphide
PVA	Polyvinyl Alcohol
RBF	Radius Bias Function
SEM	Scanning Electron Microscopy
SLA	Stereolithography
SLS	Selective Laser Sintering
SM	Subtractive Manufacturing
SSE	Single-Screw Extruder
STL	Surface Tessellation Language
TLCP	Liquid Crystalline Polymer
TPU	Thermoplastic Polyurethane
TSE	Twin-Screw Extruder
T_c	Crystallization Temperature
T_g	Glass Transition Temperature
T_m	Melting Temperature
VOC	Volatile Organic Compounds

X_c	Degree of Crystallization
XPS	Extruded Polystyrene
ΔH_m	Melting Enthalpy

CHAPTER 1 INTRODUCTION

1.1 Background

As one of the basic engineering materials, composites are composed of two or more constituents with utterly distinctive physical, mechanical and chemical properties. By organically integrating their different characteristics, these materials exhibit superior overall performance relative to their individual components [1-5]. **Figure 1.1** shows the classification of composite materials based on their reinforcement forms and internal structures during their fabrication [6]. Of all composite materials, the fiber reinforced polymer composites (FRPC) receive extensive research and industrial applications due to their exceptional strength to weight ratios [7]. To date, numerous techniques have been utilized in the manufacturing of FRPC like injection molding, compression molding, hand layup, resin transfer molding, filament winding, pultrusion and automate fiber placement [8-12]. Nevertheless, these conventional manufacturing methods require expensive molds, dies or lithographic masks and have the limitation for special fiber alignment, leading to the bottlenecks for the industrial production of complex and customized constructions [13]. Therefore, it becomes extremely imperative to explore new manufacturing technology to bypass long and costly processing procedures with more flexibility in structural design.

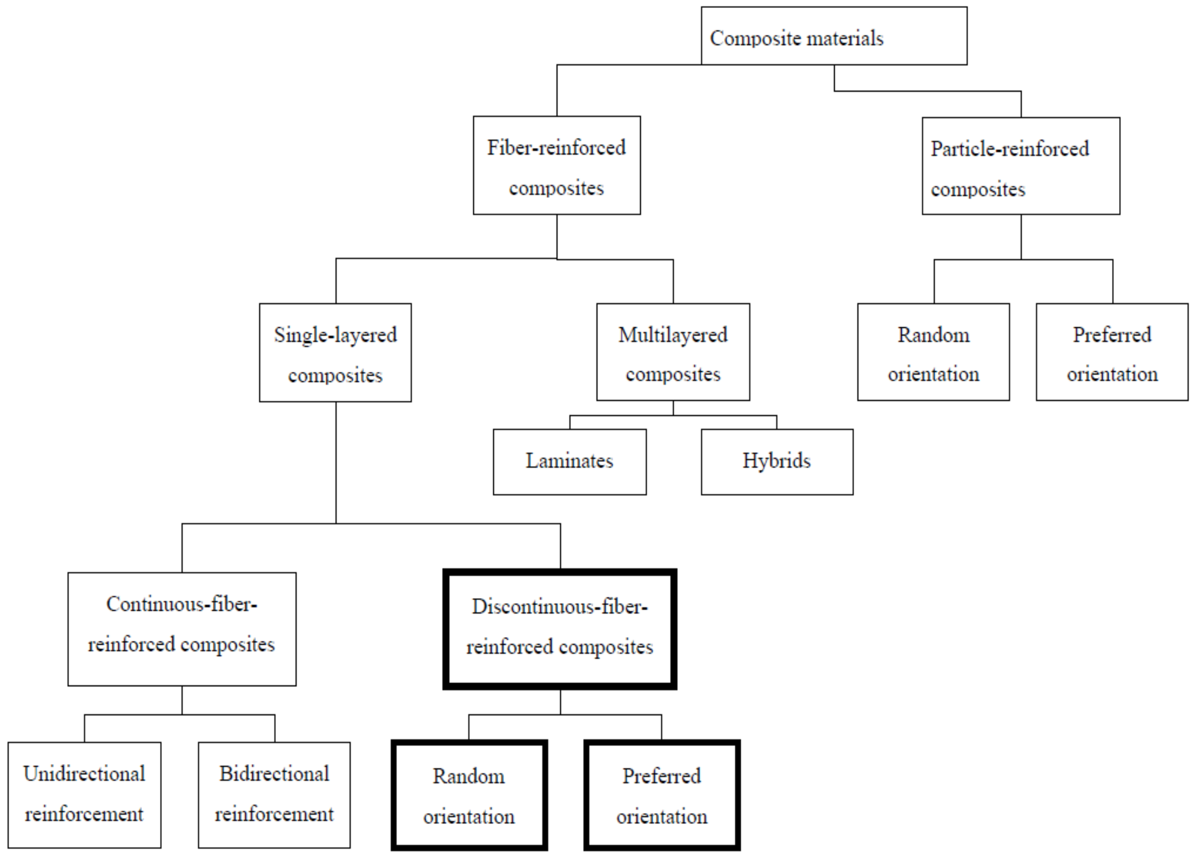

Figure 1.1 The classification of composite materials [6].

Additive manufacturing (AM), also known as 3D printing, rapid prototyping, or solid-freeform, is a disruptive technology that not only has a great potential to supplant many conventional manufacturing methods, but provide a new avenue for new products, new supply chains and new business services [14]. The fabrication process of a part through this technology is to add materials layer-by-layer directly from a 3D model, as opposite to subtractive methodologies. It starts with a meshed computer model that can be developed from the computer-aided design (CAD) software and converted into standard AM file formats that can be recognized by the corresponding 3D printers, such as surface tessellation language (STL) file or material template library (MTL) file. These files with sliced 2D layers can be further manipulated in terms of various machine-related processing parameters (e.g. infill density, infill pattern, layer height, wall thickness, etc.) to fulfil the part printing [15, 16]. As a promising technology, AM offers distinct advantages over the aforementioned manufacturing methodologies. Designs for printed parts can be easily created, modified and shared so that the manufacturing process can be simultaneously carried out at different locations according to the client requirement [17]. Compared to other subtractive manufacturing (SM) processes that need to remove materials from their original blocks, AM makes the most use of raw materials to fabricate the final part by simply adding materials with minimal waste [18]. The fully customized parts with intricate geometries (internal or external) can be created in an economic manner without the use of additional machining tools (e.g. jigs, fixtures, cutting units, etc.). Studies show that this cost-effective technology is highly competitive to make the small lot-size (even one piece), for instance, with polymer injection molding for the targeted yield below 1000 items [19]. It, to a certain extent, facilitates the product design innovation by avoiding extra consideration of manufacturing and assembly principle [20]. Moreover, the lean production of maximum material utilization rate, low energy expenditure and minimal waste with recyclable and reusable residues endow AM with the capacity of designing and manufacturing environment-friendly products [21]. By altering material composition and topological structure within a part during the processing stage, gradient and multi-functionalities can be imputed into the printed product with hierarchical and multi-material features [22].

Since the AM concept was proposed from a patent by Charles Hull in 1984, multifarious 3D printing methods have been invented by encompassing a wide range of technologies [23]. According to the ASTM international standard F2792, all these AM techniques can be defined into seven categories of manufacturing processes in terms of their respective characteristics and limitations, including material extrusion, material jetting, binder jetting, sheet lamination, vat photopolymerization, powder bed fusion and directed energy deposition [24]. By cause of the expired early patents regarding these AM methods and devices, a significant growth with annual average of around 30% is sustained after 2010 in global market sales (i.e. materials, products and services), mostly ascribing to the huge decrease for purchasing a commercial 3D printer with available price lower than $500 [25, 26]. Industry is giving enormous investments in AM systems by perceiving the manufacturing advantages of these technologies including design improvement, assembly reduction through part consolidation and simplified production supply chains through point-of-use fabrication [27]. They have been witnessed the wide application in numerous fields, such as automotive and aerospace industries for complex and lightweight structures with high load-bearing capacities, biomedical and orthopedic industries for bioactive tissues, organs and implants, architectural field for prototype designs and electronic industry for active components [28-31]. In order to produce more than 100,000 3D printed parts for jet engines by 2020, General Electric sets the corporation plan of $3.5 billion investment in additive manufacturing [32]. The report from McKinsey Global Institute also estimated that the global economic impact caused by AM in 2025 will be $200 bn-$600 bn per year with the entire manufacturing cost reduction of 35%-60% [33].

Built upon the rapid evolution of various AM techniques, they have been flourishing in composite industry with the ability to incorporate various fillers into plastic printing. The manufacturing of FRPC via AM technology currently can be accomplished by the following 4 approaches: fused deposition modelling (FDM), selective laser sintering (SLS), laminated object manufacturing (LOM) and stereolithography (SLA) [34]. Among all these techniques, FDM is the most widely used and proliferated 3D printing process for FRPC fabrication by virtue of its cheap setup cost, low energy input and material consumption, minimal waste emission and facile operation [35]. Although the advancement of FDM technique in the past five years enables the 3D printing of continuous FRPC with its higher mechanical performance, the necessity for the modification of common 3D printers with complex processing makes it at the infant stage [36-40]. As the only company (i.e. Markforged) in the world successfully commercializing the FDM printer for continuous FRPC fabrication, most of the published researches are central in the employment of this machine with its monopolistic raw material supply, deficient matrix option (only one plastic material called Onyx), finite design freedom and extravagant cost [41-43]. It leads to a lack of robust and standard paradigm for the AM of continuous fiber reinforced composites. The mainstream for the FDM production of composite parts with intense investigation is still based on the application of discontinuous fibers as a filler due to relatively low cost, moderately improved mechanical properties and no machine modification requirement.

Dated back to the early 1930s, hot melt extrusion (HME) has been a well-established industrial manufacturing technology predominantly in the plastic processing, but also in food and pharmaceutical fields. The majority of polymer products involve HME in their manufacturing steps and this stage with HME processing typically accounts for 50% of the total energy expenditure [44]. As an independent machine, the hot-melted extruder can fabricate continuous sheets, tubes, pipes and FDM filaments while plastic parts like toys, spools, bottles, packages can be produced in association with other manufacturing techniques including injection molding, thermoforming and blow molding [45, 46]. The basic principle of HME operation simply relies on the melting and cooling of thermoplastic polymers to form desired shapes, making it a green technology with solvent free trait [47]. Its unique blending geometry with highly customized screw configurations can promote high-shear localized mixing, contributing to the high-throughput manufacturing of composite materials with great phase uniformity [48]. The continuous operation with few processing requirements also endows this technique with higher scalability and time-/cost-efficiency [49].

1.2 Aims and objectives

The aim of this research project focuses on the fabrication of FRPC via HME+IM and HME+FDM systems, respectively. Although the manufacturing industry tends to move from the conventional methods to advanced AM strategies due to the above mentioned merits, the two systems studied here are both built upon the essential processing technique HME to provide the proper feedstock. The reinforcement chosen for the composite fabrication is carbon fiber (CF) for its superior mechanical properties. The thermoplastics used as matrices are two typical polymers for IM and FDM productions: HDPE and PLA. The main objectives of this thesis are listed as the following:

- To employ the simple and economical technique called spray coating to modify the surface properties of CF with the incorporation of carbon nanotube (CNT).
- To fabricate the hierarchical CNT-CF/HDPE composites via the coupling of twin-screw extrusion and IM techniques.
- To examine the mechanical (i.e. tensile, flexural and hardness), thermal (i.e. melting temperature, crystallization temperature and degree of crystallization) and morphological properties (i.e. fractural surfaces) of these hierarchical composites as a function of varying CF loadings and with/without CNT coatings.
- To apply long CF (~4.6 mm) into the 3D printing of PLA composites via the coupling of twin-screw extrusion and FDM techniques.
- To assess the mechanical (i.e. tensile, flexural and hardness), thermal (i.e. thermal conductivity) and morphological properties (i.e. fractural surfaces) of these 3D printed composites as a function of varying CF loadings.
- To introduce machine learning into the prediction of the optimal mechanical properties of 3D printed CF/PLA composites.

- To design new chiral structures by employing polynomial equation and realize the fabrication via FDM-based composite printing.
- To investigate the effects of these chiral structures and the CF addition on the deformation and mechanical properties via tensile experiment [50] and finite element analysis (FEA) [51-57].

1.3 Thesis structure

This PhD thesis is composed of seven chapters and organized as follows:

Chapter 1 briefly introduces the conventional manufacturing methods for various composite materials; the history, process and future expectation for the advanced AM technology; the FDM technique for discontinuous FRPC fabrication; and the basic feedstock production built upon HME. Besides, the aims and objectives are also given to highlight the novelty of this project.

Chapter 2 provides a detailed literature review on the HME manufacturing of discontinuous fiber reinforced composites. As it can be seen in **Figure 1.2**, the structure of this chapter includes three main sections: HME, FDM and discontinuous FDM feedstock for FDM. As the indispensible upstream operation, the mechanism and process of HME is first summarized combining with the most popular downstream IM technique. Then, the detailed FDM process is analyzed in terms of material feeding, melting, extrusion, deposition and solidifcation. The common composite feedstock involving various thermoplastic matrices, discontinuous fibers and support materials is also discussed.

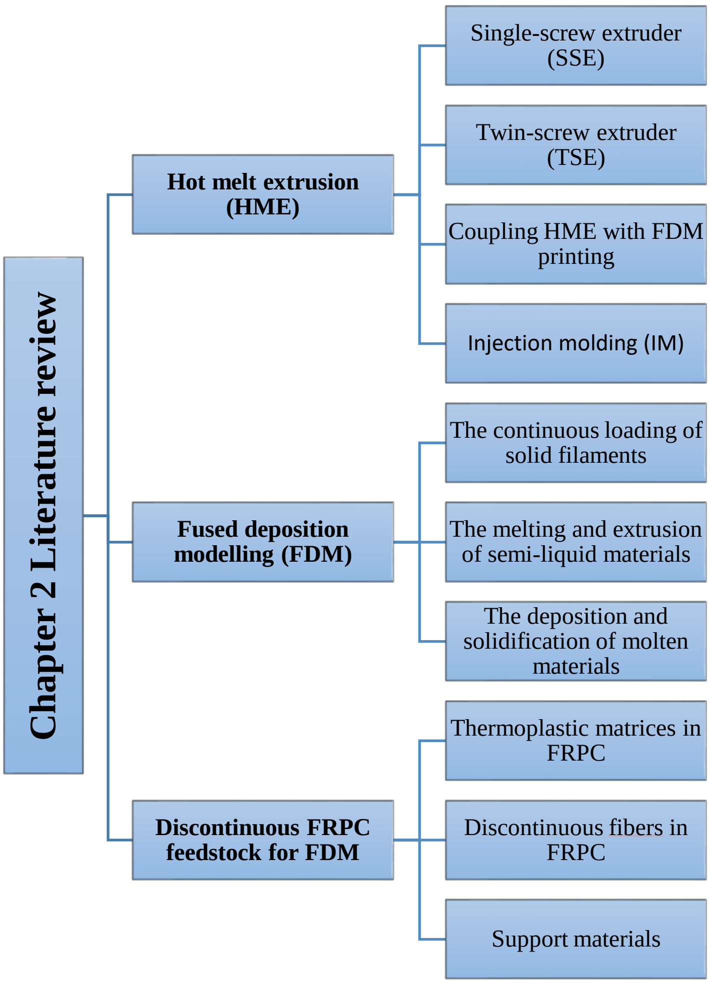

Figure 1.2 The structure of chapter 2 literature reiview

Chapter 3 describes all the materials and experiments employed in this research, including the fiber, nano-scale modifier and thermoplastic polymers as feedstock; a series of sample preparation methods based on HME, IM and FDM; and the mechanical, thermodynamic and morphological characterizations for the fabricated FRPC.

Chapter 4 investigates the fiber/polymer interfacial bonding properteis of chopped CF reinforced HDPE composites that are prepared via HME and IM approaches. Spray coating technique is utilized to modify CFs via the incorporation of CNTs so as to increase their surface roughness. The effects of varying CF contents and CNT coatings on the interfacial adhesion between CF and HDPE are studied for the first time.

Chapter 5 focuses on the fabrication of CF/PLA composites via HME and FDM approaches. The composite filament is large-scale manufactured by using an industrial twin-screw extruder with the addition of long CF (~4.6 mm). The effect of varying CF content on the tensile, flexural, hardness, thermal conductivity and fractural properties is studied. Furthermore, machine learning is for the first time introduced into the research of FDM-based composite to predict the optimal CF loading within a certain range.

Chapter 6 presents the research on the FDM printing of chiral CF/PLA composites with negative Poisson's ratio. At first, the novel chiral structure with varying Poisson's ratios is designed into four types by altering the polynomial orders. All these types are fabricated both by neat PLA and CF composites so as to investigate the impacts of geometric variations and CF loadings on tensile deformation and mechanical performance of these 3D printed chiral materials. FEA is also employed as a theoretical analysis tool to validate the experimental results

Chapter 7 summarizes the major conclusions in this thesis and identifies some personal perspectives on the furture work that can be conducted to solve the issues or undone aspects in this research project.

CHAPTER 2 LITERATURE REVIEW

2.1 Hot melt extrusion (HME)

2.1.1 Basic structure and process of HME

The HME system usually consists of an extruder, downstream processing equipment and other sensors to monitor and assess the product quality. The mixture of thermoplastic polymers and discontinuous fibers is added into the extruder through a feed hopper where the feed rate can be controlled by an electrically operated valve. The rotating screw located inside of the extruder barrel is driven by a motor so that the feedstock material can be conveyed at a predetermined speed. Concurrently, the polymer material is melted to mix with fibril fillers via multiple heaters in the barrel wall. Once the molten flow of material is pushed forward to the end of the barrel, a die is attached to assist the material extrusion into the desired shape. The basic structure of an extruder can be seen in **Figure 2.1** [45]. The extruded filament can be quickly cooled and solidified through a water tank, and then wrapped onto a spool via a collection unit. All these equipment and sensors are connected to a central control system in order to regulate the processing parameters such as barrel temperature, screw speed, feed rate, pressure, etc. More details regarding the operation and mechanisms of polymer based extrusion can be referred to related reviews [58, 59]. In recent years, HME has also be directly integrated with FDM into a single continuous process to achieve a more effective and efficient large-scale AM of FRPC [60-62]. Based on the material conveying mechanism, three types of HME can be defined: ram, single-screw and twin-screw extruders. Although the first type is easy by simply pushing the material with a piston, the discontinuous operation and inefficient heat transfer restrict its application [63]. Therefore, another two HME methods (i.e. single- and twin-screw extrusion) will be discussed in this section.

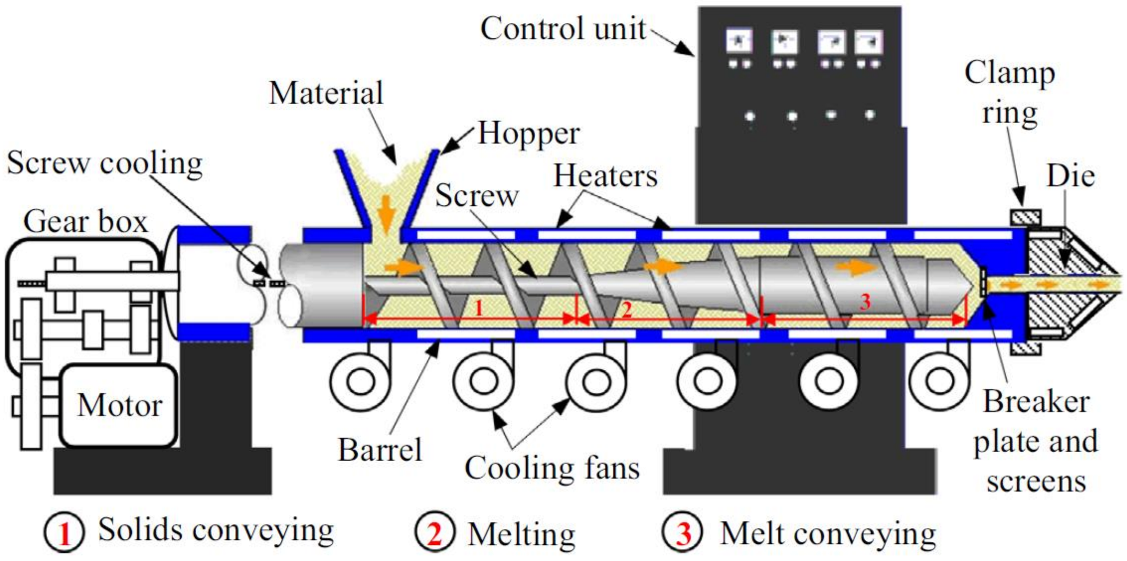

Figure 2.1 Basic components in a screw extruder [45].

2.1.2 Single-screw extruder (SSE)

Invented in the 1870s, SSE is the most widely used extruder by virtue of its simple operation in polymer and rubber processing [64]. The most fundamental configuration of SSE is the one rotating screw installed inside a stationary cylindrical barrel where three discrete zones can be distinctively subdivided: a feed zone, a compression zone and a metering zone [65]. Dissimilar pressures along the screw length can be generated based on the variation of the depth along with the pitch of screw flights within each zone. In order to consistently feed the materials from the hopper into the extruder barrel, the screw flight depth and pitch are normally designed at larger scales than those from other zones so that a very low pressure can be achieved at the feed zone. With the rotation-driven conveyance into the compression zone, the solid materials need to be melted and homogenized so that they can be converted into a suitable form to be delivered into the metering zone. Thus, a gradual increase of barrel pressure along the length of the compression zone is created by decreasing the screw pitch and/or flight depth [66].

Mixing, kneading and devolatilizing can also be accomplished in this processing zone for some less demanding applications [67, 68]. With the stabilization of the effervescent flow into a steady state in the last zone (i.e. metering zone), a uniform product with consistent shape can be ensured from the die extrusion. Since it can produce a very high pressure during the operation, the manufacturing of extrusion-based products via SSE is extremely suited for highly viscous polymers [69].

The feed system for most SSE is flood fed via the extruder hopper, where the material is added through the feed throat into the barrel by gravitational force and the output rate is determined by the rotation speed of the screw. The high pressure generated in conveying materials from this feed system tends to compact the plastic pellets or powders into the solid bed [59, 70]. Occasionally, the mass flow rate can be independent of the screw speed and regulated directly from the feed system based on the starve fed mechanism, leading to the output rate lower than the forwarding efficiency of the screw [71, 72]. The occurrence of agglomeration can be avoided with the improvement of mixing action since the pressure accumulated along the screw is less than that from the flood feeding. The formation of a loose solid bed due to the much less compaction also facilitates the melting action as those polymer particles sustain their individuality [73]. However, the reduced capacity of extrusion throughput and more complicated operation with the introduction of a controllable feed device, to a certain extent, restrict the application of this feed system in SSE [74]. With the rotation of the screw in the extruder barrel, heat energy can be created owing to the friction between the rotating screw and the inner surface barrel. Combined with the heat flux from temperature-controlled heaters, the particulate materials can be melted from the solid bed into a viscous liquid pool so that the melted extrudate can be extruded out from the die for the further downstream processing [75].

2.1.3 Twin-screw extruder (TSE)

The SSE process is simple and cost effective but does not possess a remarkable mixing capacity that is preferred for the manufacturing of polymer composites with multiple components compounded. Therefore, a modified extruder called TSE with two screws arranged side-by-side in the modular barrel was created in the late 1930s with the aim to form intimate mixtures of two or more materials [76]. In a typical TSE, the rotation of these two screws can be designed either in the same direction (co-rotating) or in the opposite direction (counter-rotating) (**Figure 2.2**). Based on the positive displacement pump from the co-rotating twin-screw design, a wide range of mixing actions and efficient heat transfer are obtained with a faster throughput independent from the screw speed [77]. In contrast, the counter-rotating arrangement can produce a very high extensional shear force between the gap of two screws, enabling high pressure generation, potential air entrap, and long retention time with low screw speed and output [78, 79]. Both of them can be further classified into fully intermeshing or non-intermeshing. As the most used type, the intermeshing TSE can not only reduce the non-motion during extrusion but avoid the localized overheat of raw materials due to its self-wiping feature. The rotation of both screws is able to remove residual materials from the screw roots and clean the whole inside barrel after the operation. Meanwhile, the product waste can also be minimized at the end of the production via this popular configuration [74]. For the non-intermeshing type, the mutually separate screws positioned in the extruder barrel result in a weak interaction and low torque generation, making it a better option in processing highly viscous materials and venting to remove internal volatile substances [80].

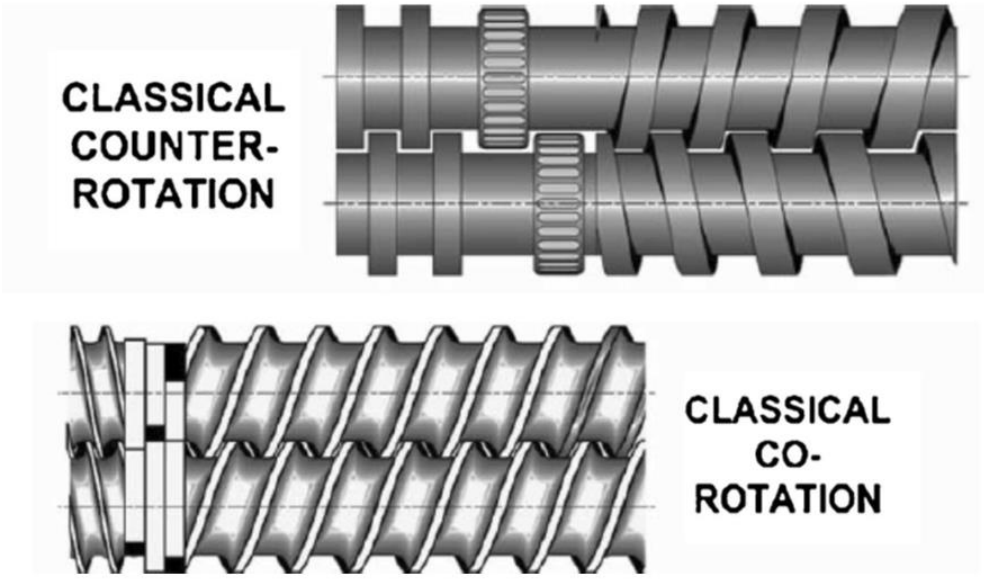

Figure 2.2 The two types of screw design for twin-screw extrusion including counter-rotation and co-rotation [81].

The diversity of screw designs also exhibits a wide variation of screw profiles in the same extruder with the intricate combination of two basic screw elements: conveying and kneading segments (**Figure 2.3**). Also known as flighted segments, the conveying segments with relatively large channel depth (i.e. 2-3 mm for lab-scale extruders and several centimeters for industrial counterparts) are normally employed for the delivery of raw materials along the length of the extruder barrel. By modifying the pitch length and the amount of flights, the conveying rate in the feed and compression sections can be adjusted [82]. According to the difference of rotation directions in this element, the right-handed pitch ensures the consistent conveying of materials with high pumping capacity while the left-handed pitch (i.e. reverse screw segments) can yield intense shearing through pushing the molten material along the direction opposite to its flow towards the extruder end. The combination of these forward and reverse screw segments has been proved as an effective avenue to compress materials due to its great pressure buildup [83]. On the other hand, the kneading segments play a crucial role in mixing the different materials in the barrel. The kneading capacity can be regulated by positioning each of these segments at varying angles (e.g. 30°, 60° and 90°), and the last angle has the best homogenizing effect with the stagnation of these materials [84]. Although the kneading segments can provide a sufficient mixing action, they may also impair the material properties due to the excessive grinding force, such as the added fiber length and matrix rheology for the composite extrusion [85]. The modification of screw profiles by coordinating the arrangement of these screw segments endows TSE with greater versatility to achieve desirable shear, mixing and conveying levels. Meanwhile, it also well explains the large overlap existing in the processing capabilities of co-rotating and counter-rotating screw modes by virtue of the diversified design of screw profiles [86].

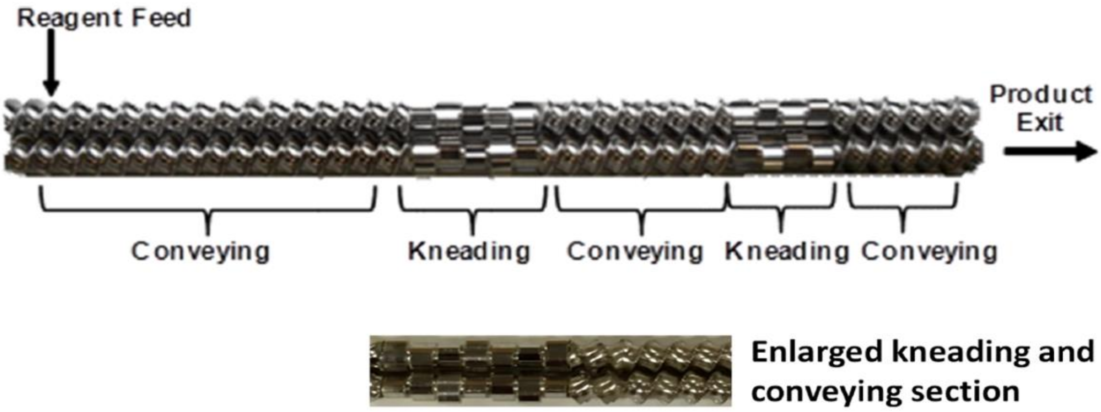

Figure 2.3 The two basic screw elements in intermeshing co-rotating screws [82].

2.1.4 Injection molding (IM)

IM is one of the most important polymer processing techniques to manufacture objects with varying sizes, shapes and may details. It involves in the injection of melted thermoplastics or mixed polymer-based composites into a mold under the condition of high temperature and presssue, the solidification of the part via cooling inside the mold and the ejection to be a finished product at the end of the manufacturing cycle [87]. The IM machine is mainly composed of two parts: the injection unit and the clamping unit (**Figure 2.4**) [88]. The first unit is actually a HME setup while the die at the tip of the extrusion barrel is replaced by a nozzle cap, before which a non-return valve is installed to prevent the backward flow of the melt during injection. As the terminal element, the mold of the clamping unit is the most typical feature in the IM machine. It has two halves that can be combined to create a cavity with designable 3D shape so that the molded object can form a specific outer surface. In order to improve the productivity, one mold can also possess several cavities to simultaneously fabricate more than one object in a production cycle. As shown in **Figure 2.4**, one half of the mold is fixed at a stationary platen and directly connected with the nozzle to facilitate the melt flow while the other half is mounted at a mobile platen that is driven by a motor. The clamping force should be larger than the injection pressure with the view of preventing the melt leaking due to the mold opening and keeping the cavity pressue [89].

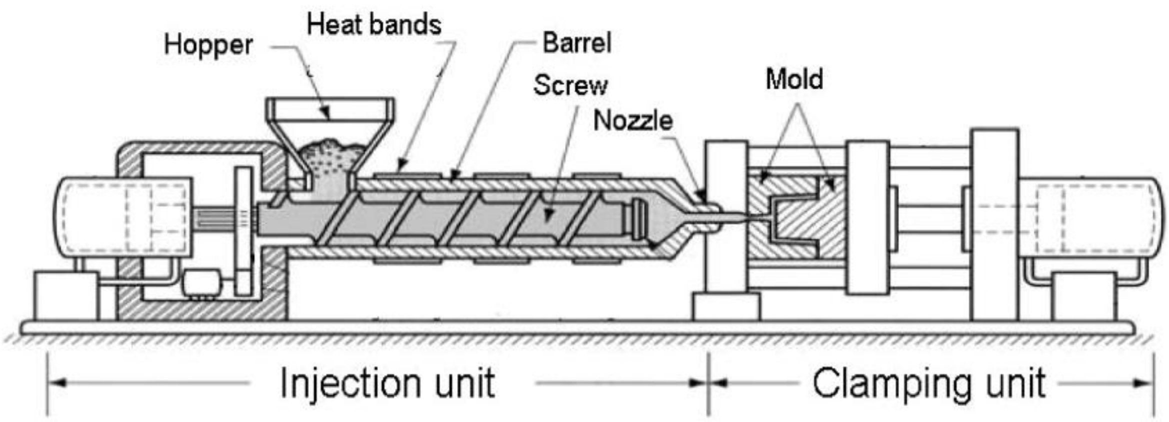

Figure 2.4 The basic structure of an injection molding machine [88].

The cyclic manufacturing proces of IM can be categorized into the following steps: (1) filling, involving the injection of the melt flow into a closed mold under certain pressure; (2) packaging, where the injected melt is squeezed under the high pressure to prevent its shinkage; (3) cooling, involving the solification of the melt flow at a relatively low temperature; and (4) ejection, where the shaped object is ejected by pins located at the mobile half of the mold for the next production cycle [90]. The overall manufacturing time is normally less than one minute [91]. Among all these steps, the cooling process is the most significant stage as it accounts for around 80% of the cycle time [92]. With the aid of a cooling system based on water circulation, the mold temperature can be regulated to optimize the hardening of the material so that the thermal stress is eliminated in order to maintain the structural stability. The IM process can be either single-stage with the operation of plastication and injection in the same barrel via rotational screws, or two-stage where the melt is conveyed to an accumulator chamber and then ram-injected into the mold cavity [93].

2.2 Coupling HME with FDM printing

Almost all thermoplastic-based materials used in the FDM process are prepared by HME in the form of continuous filaments. As an indispensable operation, how to manufacture good quality thermoplastic filaments from HME should be carefully concerned so that they can be successfully processed in FDM printing. The option of raw materials should be stiff yet flexible enough so that the produced filament from the extruder will not break during wrapping and unwrapping from a spool. To meet this requirement, a minimum strain at yield of around 5% has been recommended for its mechanical properties [94]. A sufficient strength and stiffness should be guaranteed so as to withstand the pushing and pinching force in the feeding mechanism of FDM. The constant delivery of a filament without buckling is essential to print a part with stable quality. Meanwhile, the filament fabricated from HME should have a proper viscosity to maintain the uniform deposition. A too low viscosity may lead to dripping while a too high viscosity could hamper the extrusion from the printing head, although higher nozzle temperature can be utilized to overcome this issue [95, 96]. In addition, with the increase of fiber loadings and lengths, the continuous feeding of discontinuous fiber/matrix pellet mixture into the hopper of HME system is a challenging issue since relatively long fibers with high contents will gather at the feed throat to form a net-like structure, restricting the continuous adding of this mixture into the barrel. In one of our recently accepted patents, we invented an automatic material push-feeding setup that can be freely installed onto the feed hopper of the extruder. By punching the material throughout the feeding channel with varying rates, we eliminated the blockage of material flow at the throat and facilitated the homogeneous feeding of long fiber/polymer pellet mixtures into the extruder barrel [97]. Furthermore, high percentages of fibers may also increase the brittleness and cause the sharkskin instability for the HME-made composite filament, impairing the processability both in filament production and FDM printing [98].

2.3 Fused deposition modelling (FDM)

Invented by Scott Crump in 1989, FDM is the first commercialized AM technique through the founding of his company Stratasys and now holds the largest market in polymer based 3D printing [99, 100]. Since FDM is trademarked by Stratasys at the beginning, this technique also has another equivalent term called “fused filament fabrication (FFF)”, vividly depicting the fundamental mechanism underlying the melting and deposition of feedstocks in the form of filaments to print designed parts [101]. The basic structure of a FDM printer can be seen in **Figure 2.5**. In general, the operation of a common FDM based system can be categorized into the following three steps: (1) the continuous loading of solid filaments via a feeding roller; (2) the melting and extrusion of semi-liquid materials through a nozzle; and (3) the deposition and solidification of molten materials onto a build plate.

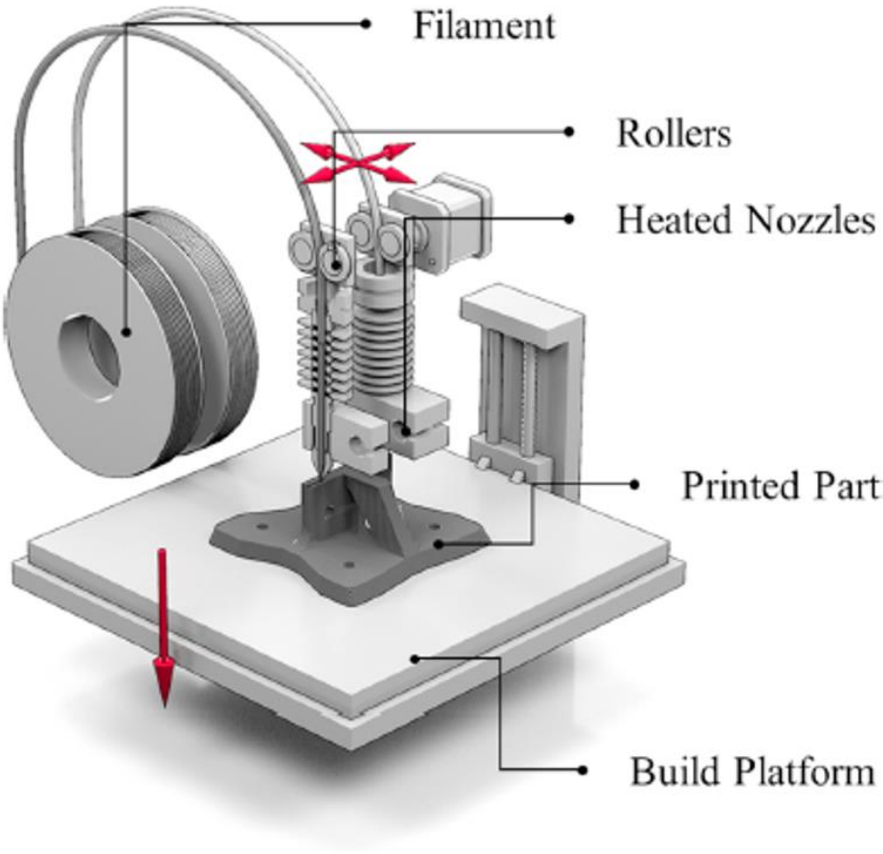

Figure 2.5 The schematic of the basic structure for a FDM printer with red arrows showing the relative mechanical motion of components [101].

2.3.1 The continuous loading of solid filaments

The FDM process begins with loading the coiled filament from a spool through the feed system to the heated nozzle. It consists of two pinch rollers and a stepper motor where the stepper motor pushes the solid filament forward with the aid of a radial force exerted by pinch rollers. The surfaces of one or both of rollers possess grooved or toothed textures so as to avoid the slippage of the moving filament with sufficient friction [102]. To ensure a continuous and stable loading movement, a uniform and feedable filament with suitable mechanical and melt flow properties is required so that the constant amount of materials can be extruded for higher quality printing. By adopting a custom-made texture analyzer to simulate the forces of pinch rollers on the filament and map out the flexibility profiles from the recorded force-distance curve, Nasereddin et al. developed a simple mechanical screening approach to predict the feedability of a filament from the comparison of its profile with those of commercial counterparts via correlation analysis (**Figure 2.6**) [103]. It is also crucial to minimize the deviation of the filament diameter since a big volume variation along the length causes errors in the printed shape. For instance, a thickness deviation of -0.25 mm in the filament may reduce the printed size by 11.29 mm^3 in a 10 mm material consumption, which corresponds to 15.98% of the nominal volume [104]. The HME manufactured thermoplastic based filaments for FDM normally have three thread diameters: 1.75 mm, 2.85 mm and 3 mm [105]. For the thicker filament, its high strength and stiffness promotes a smoother loading process with less likelihood of filament breakage from the large compression force of rollers while more pressure is needed to push the material into the nozzle. In contrast, the thinner filament can be fed easier and faster through the same nozzle size but its high flexibility may result in buckling and twisting through the curved guide tube during the material loading [106]. No matter which diameter is selected in FDM process, the printed parts can be maintained with similar qualities once the processing parameters are fine-tuned.

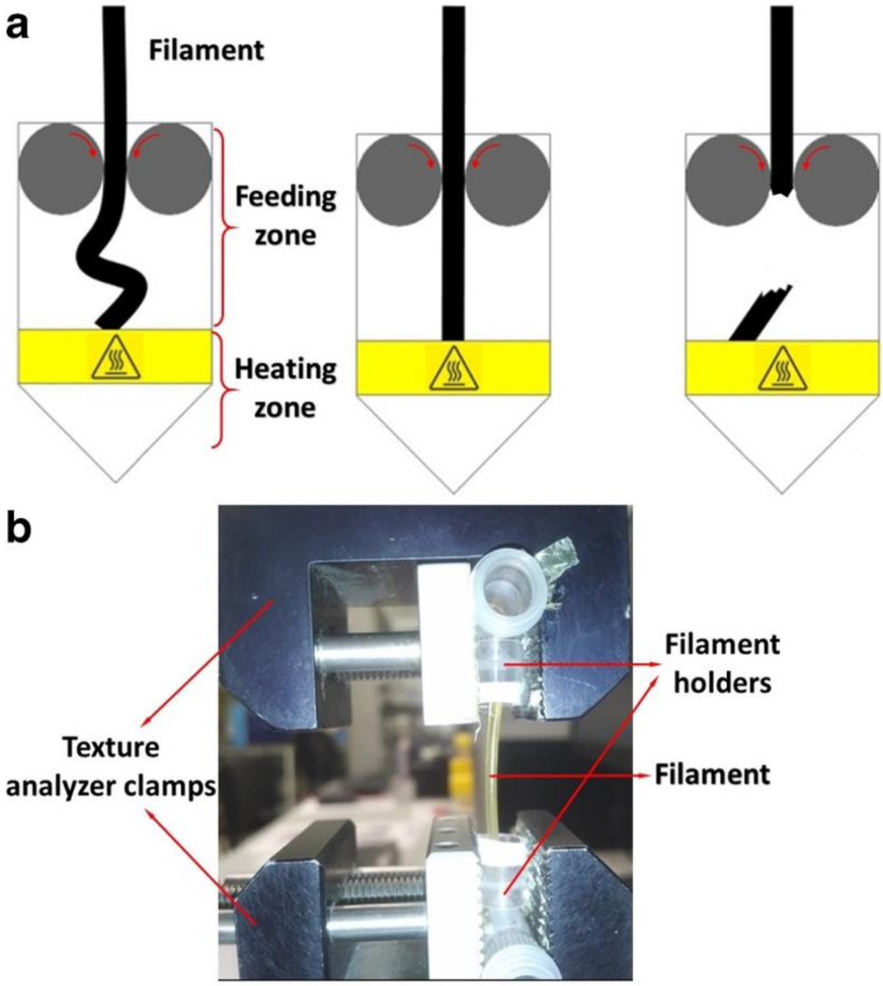

Figure 2.6 The filament loading via pinch rollers in the feed system: (a) different behaviors of loaded filaments including buckling, stable feeding and fracture; (b) the rest rig for the texture analysis of filament feedablility [103].

In situations where the filament is too brittle, humid or inhomogeneous (sustaining inconsistent pushing force), fracture may occur during the material feeding with the discontinuity for the forward thrust of the filament, causing the jam in the guide tube or clogging in the printing head. This severe issue can not only contaminate the printer with the material burning at the heated nozzle, but bring about the geometrical misalignments or failure of the printed part [107]. Since there is no solution currently able to deal with this problem automatically in FDM machines, operators need to visually identify it, manually terminate the printing, clean the feeding system by disassembling the entire printing head and restart the whole part from the scratch [108, 109]. Thus, the monitoring of filament breakage in the material loading plays an important role in guaranteeing the successful FDM operation. By introducing an acoustic emission (AE) sensor into the loading system, Wu et al. created a lightweight FDM machine condition monitoring tool to identify both normal and abnormal printing states. As AE hits, the original waveform signals were received and simplified via the combined application of principle component analysis and the hidden semi-Markov model so that common machine failures like the material run-out or filament breakage can be diagnosed in a real-time fashion [110]. Based on the same AE technique, Yang et al. deduced the different probability distributions of AE signals by employing two quantified indicators (i.e. instantaneous skewness and relative similarity) to accurately identify the filament breakage from the steady feeding state, offering a potential strategy for in situ loading detection of FDM process [111]. The optoelectronic contact switch or mechanical contact switch are also utilized in industry to monitor the breakage while these methods can only detect the existence of material in the channel. They are incapable of identifying the dynamic motion of the filament, restraining the effective diagnosis in material loadings.

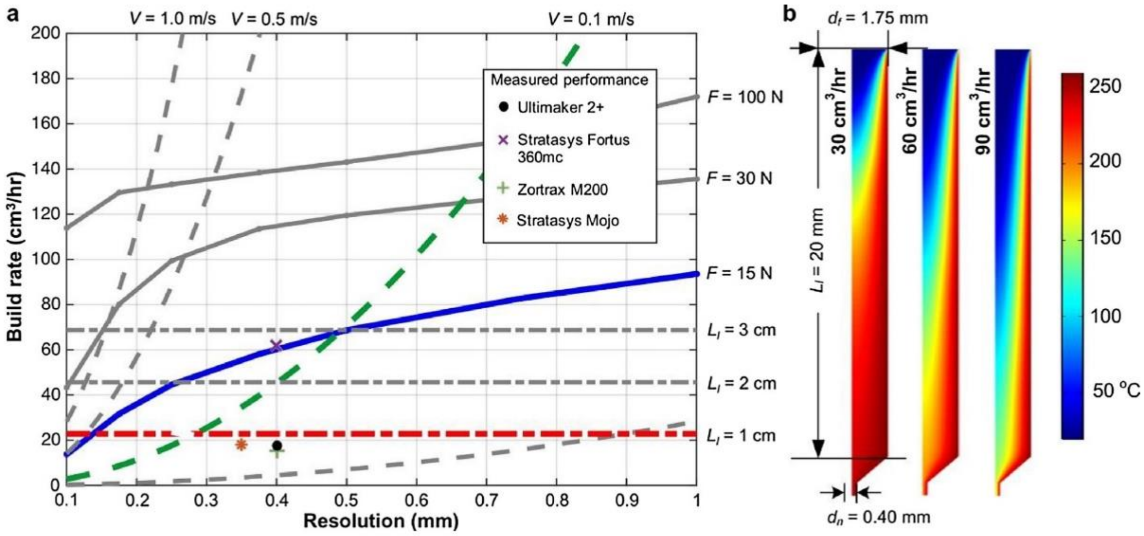

Figure 2.7 The performance summary of conventional FDM system: (a) the trade-space of volumetric build rate versus resolution in several desktop FDM printers that is constrained by maximum traction force of rollers, heat transfer rate in the liquefier and moving speed of the printing head. The common area under three curves is the accessible performance from these selected commercial FDM printers; (b) the temperature distribution in a liquefier at varying volumetric rates, indicating the limited heat penetration at higher feed rates [112].

Improvement in the throughput of FDM process is essential to fulfil the vision of maximizing the machine utilization and advancing the production efficiency with less lead time. One critical strategy is to increase the build rate via the printing head. Both of current desktop and professional FDM machines have the similar rate (~10-100 cm^3/h) in part printing, though the latter is more remarkable in maintaining dimensional accuracy and overall quality [112]. This relatively slow build rate can be attributed to the limitations of three key modules in a FDM system: the maximum traction force of rollers from the material feed mechanism, the heat transfer rate from the thermistor to the filament core in the liquefier, and the moving speed of the printing head positioned in the gantry. Of all, the complex regulation of the feed rate is not only restricted by the pressure drop in the liquefier, but affected via the trade-off between the maximum traction of feed rollers and filament facture [102]. Through the FEA simulation of technical parameters in the modules of several commercial printers, Go et al. analyzed the rate-limiting mechanism and mapped a unifying trade-space of volumetric build rate versus resolution as a function of extrusion force, liquefying temperature and gantry speed, predicting the big possibility in enhancement of FDM build rate via the optimization of these modules (**Figure 2.7**) [112]. In consequence, a "FastFFF" system was developed, in which a rotating nut was adopted in the feed device so that a faster feed rate can be achieved. Combined with a laser-heated liquefier and servo-driven parallel gantry, the maximum extrusion rate and volumetric build rate in this prototype system respectively reached at 282 cm^3/h and 127 cm^3/h, which are ~14-fold and ~7-fold greater than commercial FDM printers (**Figure 2.8**) [113]. This system as an example overcomes the module-level performance constraints and offers a promising potential to adapt into the high-speed printing of fiber-filled composites.

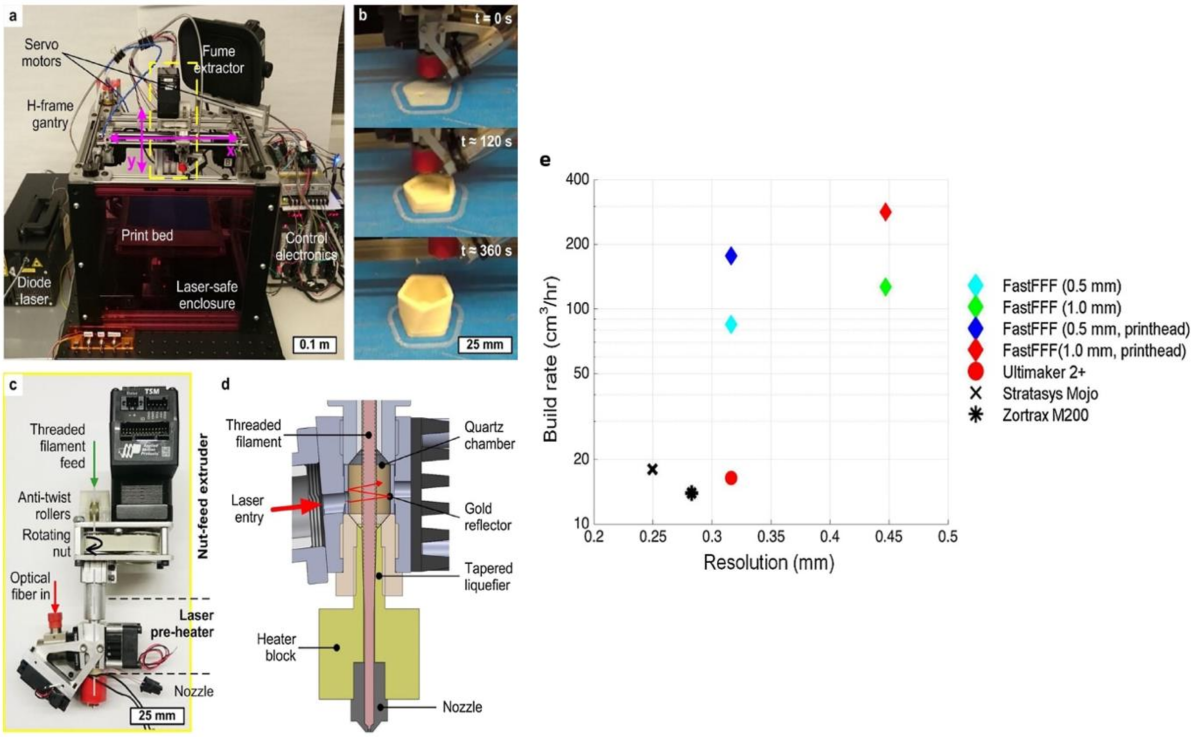

Figure 2.8 The FastFFF system with high-throughput printing head design: (a) the desktop FastFFF printer with H-frame gantry, diode laser with fiber coupling to printhead, and control electronics at a build volume of 185×125×200 mm; (b) photos for the printing of a spiral cup as a function of time; (c)

photos for the nut-feed drive unit and laster-assisted heater in the printing head; (d) cutaway solid model of the liquefier, showing how laser is coupled to filament as it travels through a quartz chamber surrounded by a reflective gold foil; (e) the comparison between FastFFF system and commercial destop FDM systems in terms of volumetric build rate versus resolution [113].

2.3.2 The melting and extrusion of semi-liquid materials

As the pivotal operation of a FDM system, the thermal process that takes place at the liquefier plays a vital role in regulating the melting and extrusion of semi-liquid thermoplastic-based materials. During this process, the input filament is loaded forward into the liquefier body where the solid material experiences a progressive heating up until its glass transition temperature (T_g) is surpassed [114]. The heat flux received by the filament converts the physical state into a thick semi-liquid material, allowing it to be extruded out from the print nozzle at the end of the liquefier. In order to ensure a continuous and stable material flow without blocking the tip of the nozzle, the temperature at the nozzle must be kept constant, which is achieved by the coiled resistance heater or cartridge heater inside a heat block. Besides the heating element, the heat block attached at the top of the nozzle also houses a thermistor (i.e. temperature sensor) to control and monitor the required temperature for the specific printed material [115]. Although the solid material inside the nozzle must be heated to an objective temperature for melting, the upper part of the filament should remain as cool as possible to avoid the possible jamming. Therefore, a heat barrier made of a low conductive stainless steel joins at the top of the heat block to reduce the upward heat conduction. In fact, minimizing the upward heat flow from the heat block can not only save more energy to maintain the desired temperature by preventing the heat lost and shortening the working time of resistance heater, but avert the discontinuous flow of the material due to the frequent fluctuation of temperature [116]. In order to further decrease the temperature close to the ambient environment, a heat sink composed of a finned case with an external cooling fan is connected with the heat barrier to dissipate heat via convection (**Figure 2.9**). This is necessary to protect the hardware durability since supporting elements that fix the heated liquefier body to the gantry are made from common plastics (with low weakening temperatures) and could be subjected to irreversible deformation or failure at the prolonged overtemperature, leading to the mechanical dysfunction of the printing machine [117].

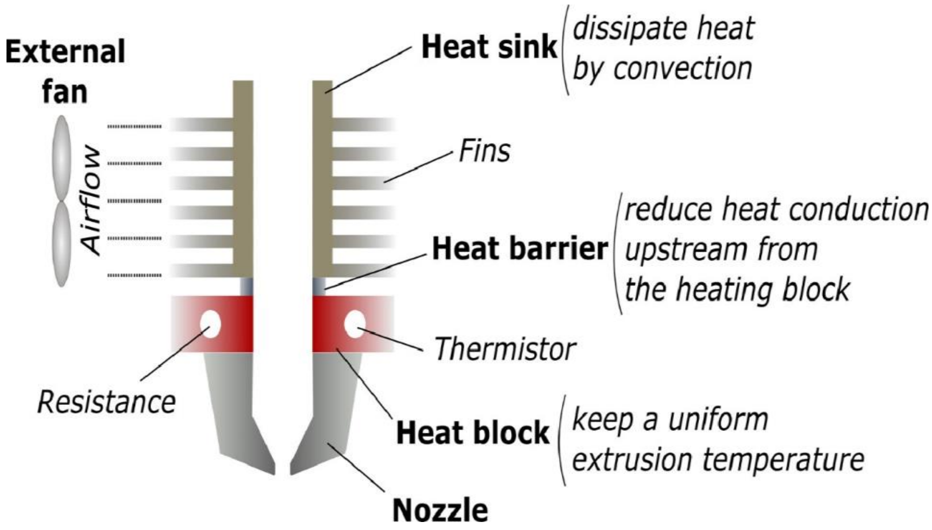

Figure 2.9 The general structure of a standard FDM liquefier with all functional parts [118].

The design and functionality of a nozzle in a standard FDM liquefier is extremely important to govern the accuracy, productivity and build quality of printed parts. One of the biggest determinants for the performance of the nozzle is the orifice size. Typically, the diameters of printing nozzles range from 0.1 to 1 mm so that the ratio of the maximum diameter contraction of the filament to its original thickness can ascend to 1:30 [119]. However, the most widely used nozzle size for a desktop FDM printer is 0.4 mm (e.g. Ultimaker 3 and Makerbot Replicator) since this size is small enough to achieve a refined surface quality of parts and maintain a reasonable build time [120]. It should be noted that the layer height should never be larger than the nozzle size because the bonding strength between neighbouring layers will be drastically decreased. This can be attributed to the reduction of contact area between the extruded layer and the previous deposited layer, thus leading to their insufficient mutual bonding. For the sake of increasing the deposition rate and build volume to meet the requirement of industrial manufacturing, the large-scale FDM system employs the nozzle with much large sizes while the print resolution and surface finish are usually compromised. Post-possessing methods like polishing and coating must be added to eliminate the rough surface of parts, which will be more time consuming and labor intensive than the initial printing. Recently, Chesser et al. created a novel nozzle-selectable system and integrated into the large-scale FDM liquefier, where the nozzle size can be altered mid-printing by utilizing a poppet nozzle selector (**Figure 2.10**). With this system, the interior of a part can be printed at a course resolution by using a large nozzle size while the surface can be fabricated at a fine resolution by shifting to a small nozzle diameter. The results from this work demonstrate that compared to the interior resolution of the composite part, a doubling of exterior resolution can be achieved without a significant increase of printing time [121]. As a new selective resolution printing technique, more work needs to be done to explore its industrialization potential, such as using finer nozzles for critical areas and developing relevant software algorithms for the intelligent selection of improved surfaces.

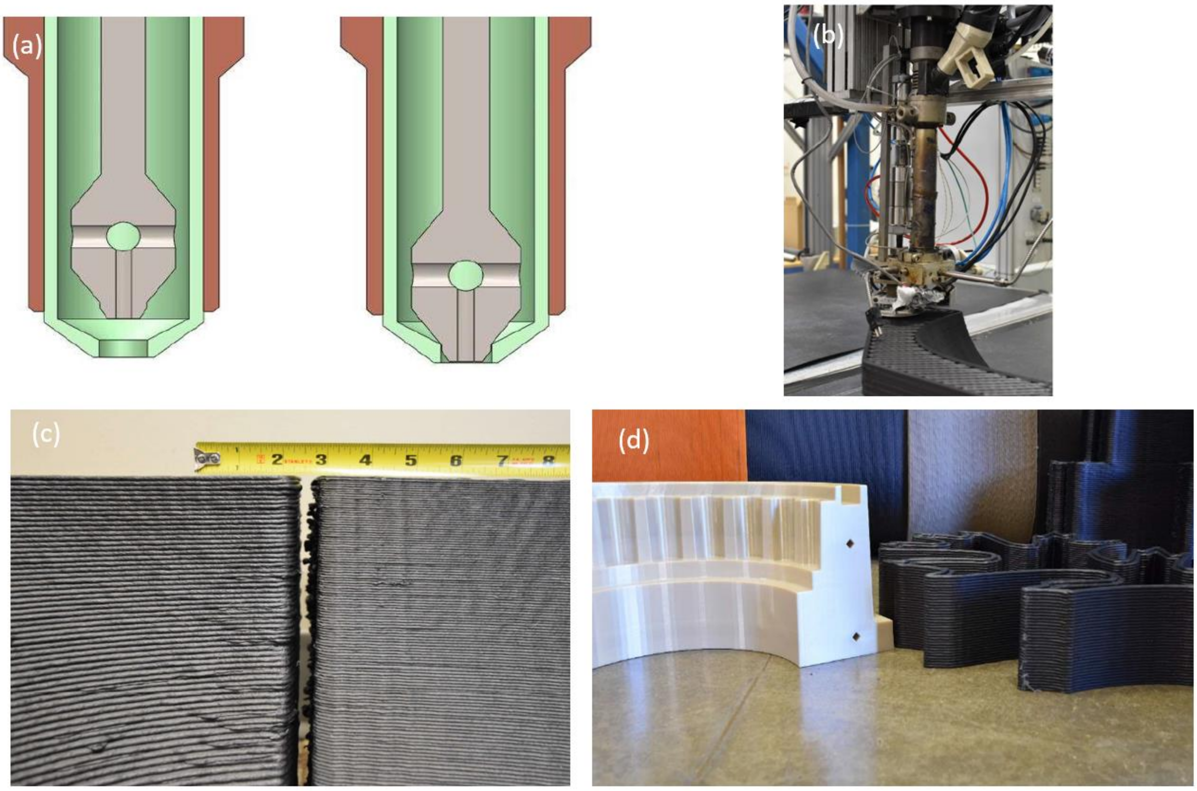

Figure 2.10 FDM printing of fiber composites with varying resolutions via selectable nozzles: (a) the poppet selector in nozzle to adjust size; (b) the fiber composite printing with multi-diameter nozzle; (c) close-up comparison of surface resolutions between normal nozzle and diameter-selectable nozzle in large-scale FDM system; (d) the printed part comparison between small-scale and large-scale FDM systems [121].

The thermal dynamics and pressure gradients in the FDM liquefier play a critical influence on the viscous flow of the material and the subsequent deposition onto the build plate. It has been demonstrated that a proper melt temperature can decrease the flow viscosity and facilitate the mutual bonding of extruded beads while a too high temperature may degrade the material by damaging inner polymer chains. If the temperature is too low, the insufficient melting of the solid material with low pressure drop could also give rise to filament buckling [122]. Many scholars conducted the theoretical research to understand the thermal history and behaviour of the material melting and extrusion in the liquefier [123-125]. For instance, Bellini et al.

investigated the transfer function of a liquefier through a mathematical model and found a strong dependency of the material viscosity on the nozzle heating [126]. As a significant factor affecting the bio-scaffold quality, Ramanath et al. studied the melt flow behaviour of poly-ε-caprolactone in a liquefier of a FDM printer via using two methods: mathematical modelling and finite element analysis (FEA) via Ansys®. The comparative results from these two modes revealed that the variation of nozzle diameters (0.25-0.4 mm) and angles (20-60°) has a direct impact on the pressure drop along the melt flow channel. The temperature gradient analysis shows the solid biopolymer was liquefied within 35% of the channel length [127]. Yardimci et al. presented a 2D deposition thermal model by utilizing corresponding analytical and computational thermal design tools to quantify the effect of nozzle design on the operational stability and temperature distribution near the vicinity of extrusion point [128]. Different from most studies focusing on the position of the melt front, Jerez-Mesa and his team designed a FEA model to tackle with the convective heat dissipation along the heat sink of a BCNozzle liquefier by the refrigerating fan. The predicted temperature profiles from the model with varying airflow velocities were validated with discrete temperature values measured via four thermocouples fixed on the liquefier body, confirming its adequacy to be applied for other working conditions [129]. Further exploration on the impact of overheat along the heat sink will also be useful to correlate the maximum acceptable temperature with the fan working regime for more energy saving. Considering the lack of related studies regarding the internal geometry of a liquefier on thermal behaviour of FDM system, the same group compared one commercial liquefier with two customized variations by adopting the same theoretical and experimental methodologies. Results show that the new design of a thick-fin heat sink with higher structural simplicity has the best performance of 3D printing under a fan velocity higher than 10% and a much lower manufacturing time than the commercial counterpart [118]. Without doubt, this work provides some insight into the heat transfer effectiveness of a certain liquefier and the optimization of this printer core component with more stable and precise temperature control.

With respect to the melting and extrusion of FRPC, the great importance of thermal dynamics in FDM liquefiers as a function of their structures and interaction between parts is also projected onto the fiber orientation in the melt flow. With the application of the Moldflow injection molding analysis package, Nixon et al. modeled the fiber orientation in the extruded beads from three different nozzle designs (i.e. convergent, divergent and straight geometries) in the FDM system. The largest overall fiber alignment was observed in the convergent nozzle while the divergent nozzle exhibited the least fiber alignment. However, before entering into the nozzles, fibers in the flow were oriented uniformly in all three liquefier channels [130]. Heller et al. presented a computational method to analyze the effects of nozzle geometry and extrudate swell on the fiber orientation in the polymer melt flow. The authors demonstrated a great fiber alignment along the flow axis within the convergent zone of the nozzle while a decreasing trend was observed in the extrudate swell, leading to a 19.9% reduction in the axial modulus of elasticity. By varying nozzle parameters, this study indicates the possibility of regulating the fiber orientation and mechanical properties of printed FRPC via the modification of FDM nozzle geometry [131]. Inspired by complex fiber arrangements in natural composites, Raney et al. developed a rotational 3D printing system with a controllably rotated deposition nozzle that enabled the spatially programmable orientation of short fibers in the polymer matrix (**Figure 2.11**). With the variation of rotation speeds, these researchers incorporated two fiber patterns (i.e. orthogonally and helically arranged fibers) into different sections of the printed composites, presenting high microstructural complexity and enhanced performance in strain, failure and damage tolerance [132]. In short, the specific design of a liquefier body has a crucial influence on the fiber orientation in the printed bead while the fiber orientation can also affect the flow field during extrusion. Due to the computational complexity for anisotropic flow, the currently limited researches simplify the modeling to consider fiber/polymer system as Newtonian isotropic fluids, which cannot accurately reflect the fiber orientation state [133]. Hence, more advanced simulation tools integrated with supercomputing are in demand for the precise prediction of the flow field and fiber orientation in the extrusion stage of fiber composites.

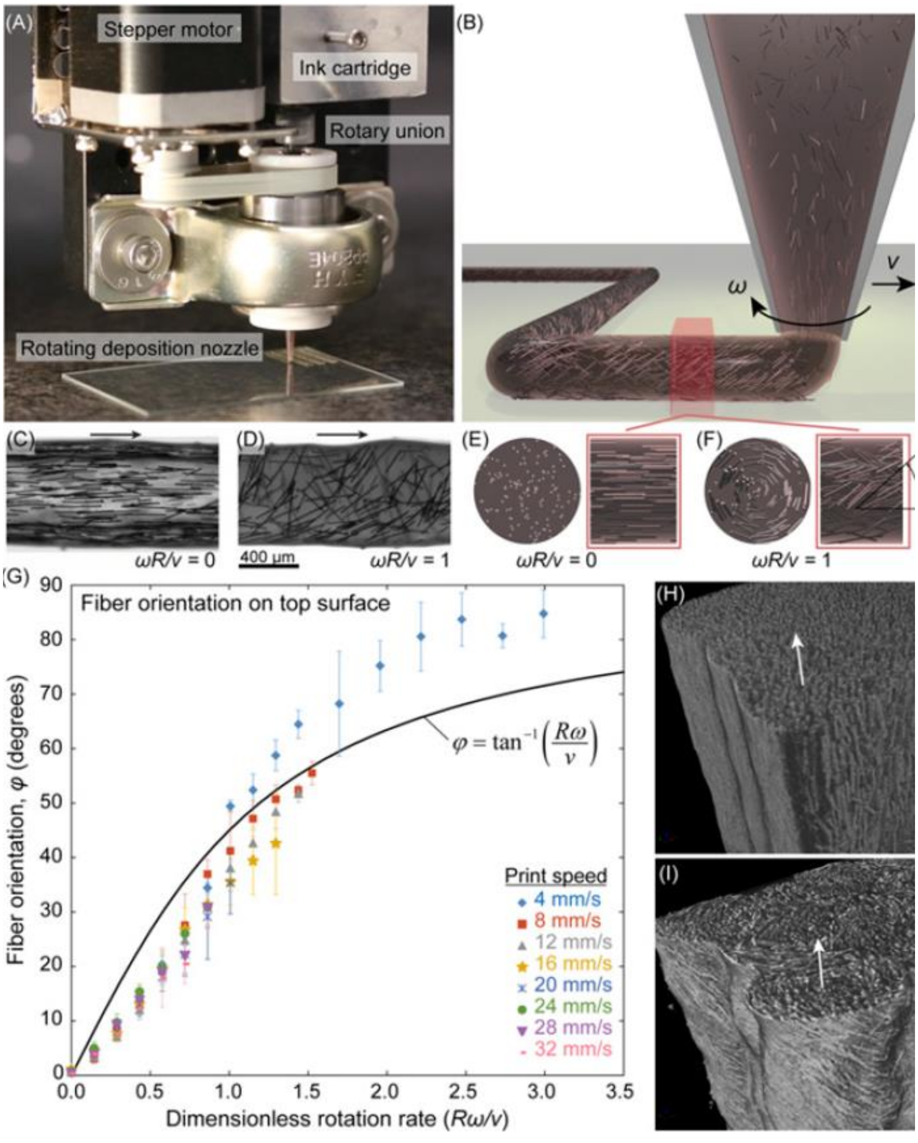

Figure 2.11 The rotational 3D printing system: (A) the controllable rotation of the nozzle during printing conducted by directly interfacing a stepper motor with a 3D motion-control system; (B) Schematic view of fiber orientations via the rotating nozzle to obtain a helical pattern, where the helical angle is adjustable by the rotational rate (ω) and translational velocity (v); (C and D) Optical micrographs of

fiber-filled composite filaments (1.3 vol % carbon fibers) printed without rotation and with a high rotation rate; (E and F) schematic views of idealized fiber arrangements for the same dimensionless rotation rates; (G) Surface fiber orientation (φ) plotted as a function of dimensionless rotation rate (Rω/v) over a wide range of rotational and translational rates,where the solid line denotes the kinematically ideal fiber orientation; (H and I) Cross-sectional views of the internal structure of composites printed without rotation and with a high rotation rate, observed by X-ray microtomography (print direction indicated by arrow) [132].

The measurement and monitoring for the temperature and pressure of the filament during the extrusion are vital to obtain a consistent part quality since any fluctuations in these conditions may produce significant impacts on the material flow, deposition rate and intra-/inter-layer bonding. As to the vast majority of FDM printers, the localized temperature is the only information that can be collected through a single thermistor located at one side of the heat block. To interpret its variation throughout this print head, the employment of multiple thermistors by some solvers can be an approach but higher probability of fluctuations is still a big issue [134]. Although infrared cameras can be integrated into the liquefier body to monitor the temperature, the observation from these devices is confined to the surface of the nozzle [135]. None of these measurements can determine the temperature variation inside the semi-liquid filament as the sensors are not in direct contact with the flow. In addition, almost all the pressure measurements inside the liquefier are inferred from mathematical modelling and FEA due to the big technical challenge in the small nozzle channel. Only one report currently enables the in-situ measurement for these two processing parameters in the melt. By creating a customized thermocouple insertion device coupled with a piezoresistive pressure transducer, Anderegg et al. successfully recorded the temperature and pressure distributions in the flow field during extrusion. Readings show the fluctuation of ± 2 ℃ and up to 11 ℃ decrease in filament temperatures respectively at idle and at high flow rate. There was also a significant fluctuation in pressure (140-6900 kPa) and the in-situ measurements were higher than theoretical predictions, indicating the limitation of computational modeling to completely capture the dynamics in the FDM liquefier [136]. Aside from the improvement of the internal process monitoring, this system also provides an empirical avenue to investigate the mutual relationship of various variables in FDM, including the flow rate, rheology, heat transfer, pressure drop, nozzle geometry and filler distribution.

2.3.3 The deposition and solidification of molten materials

In a typical FDM, the printing head installed onto a gantry is movable along X, Y and Z axes so that the deposition of material can be initiated from the nozzle by its horizontal translation at a constant height over the build plate. After the first layer, the succeeding layer is deposited via either the ascent of the printed head or the descent of the build plate, which is dependent of the individual printer [137]. This automatic process for each layer printing is repeated until the completion of the designed part. During this deposition and solidification process, the cross-bonding between beads is established by the inherent thermal energy of the extruded semi-liquid filament. A bridge between the adjacent beads called a neck is formed due to the sintering process driven by surface tension (**Figure 2.12**). Different with metal and ceramic sintering governed by volume, surface and grain boundary diffusion, the polymer sintering describes the coalescence process below the melting point based on the viscous flow mechanism [138, 139]. The mutual bonding of beads with neck growth within a layer can be termed as intralayer bonding. Meanwhile, as the bead from the next layer deposits over the previous layer, its high temperature also facilitates the formation of similar bonds between the beads of two successive layers, which can be termed as interlayer bonding [140]. Consequently, the printed objects by conventional FDM system are normally anisotropic whether in topological geometry or in physical properties.

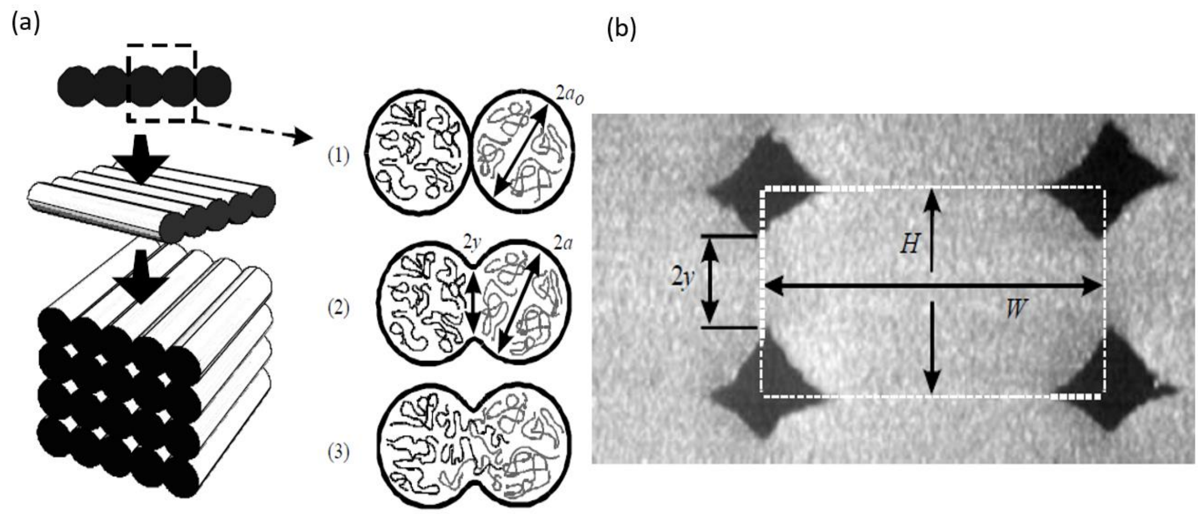

Figure 2.12 Bond formation between adjacent beads in FDM process: (a) the schematic of bond formation process involving (1) surface contacting, (2) neck growth and (3) molecular diffusion at interface and randomization; (b) the microphotograph of the cross-sectional area of a FDM part where W is the filament's width; H is the filament's height; 2y is the neck length between adjacent filaments [141].

The extent of bonding lies with the neck growth between the beads and the molecular diffusion and randomization of polymer chains at the interface. Combined with the isothermal sintering experiment, Bellehumeur et al. utilized the polymer sintering model to predict the degree of bonding during the deposition in FDM. Results show that the neck growth in the bonding zone was more affected by the extrusion temperature rather than the envelop temperature [142]. On the contrary, Sun et al. found that both the envelope temperature and variations of convective coefficients within the printer chamber have a significant impact on the mesostructured and mutual bonding of beads via the characterization of flexural properties. The sintering process also has a great repercussion on the bond formation while the critical temperature cannot be maintained too long above the glass transition owing to the fast cooling of the extruded filament [141]. Bhalodi and his team observed that the temperature at the neck between two neighbouring beads decreased exponentially with time through relating time and temperature in a mathematical model [143]. This short sintering process has been validated as the main reason for the imperfect bonding of partial coalescence, resulting in the generation of voids between each bead [144]. Numerous reports have concluded that the insufficient bond with voids acting as stress concentrators has a negative influence on the mechanical performance of the 3D printed parts, especially for the weak interlayer strength along the Z direction [145-148]. To address this issue, Ravi et al. integrated an in-process near-IR heating laser into the 3D printer to locally heat up the existing layer around the nozzle before the deposition of the extruded bead at this heated area (**Figure 2.13**). The increased interpenetrating diffusion from the raised interlayer temperature contributes to the 50% more interlayer bonding strength, 60% increase in bending strength, near 100% increase of elasticity and more than triple toughness of the FDM part compared to the counterpart without laser pre-deposition heating [149]. With the addition of 2 wt% thermally expandable microspheres in the polymer matrix, Wang et al. reported a material-based approach to improve the interlaminar bonding with reduced voids via heat treatment after FDM fabrication. Compared to untreated samples, the tensile and compressive strength was respectively increased by 25.4% and 42.2% after keeping them at 140 ℃ for 120s [150]. Besides the presence of voids, Rodriguez et al. discovered that the loss of molecular orientation after deposition is also an important factor in the decrease of overall mechanical properties in FDM parts [151].

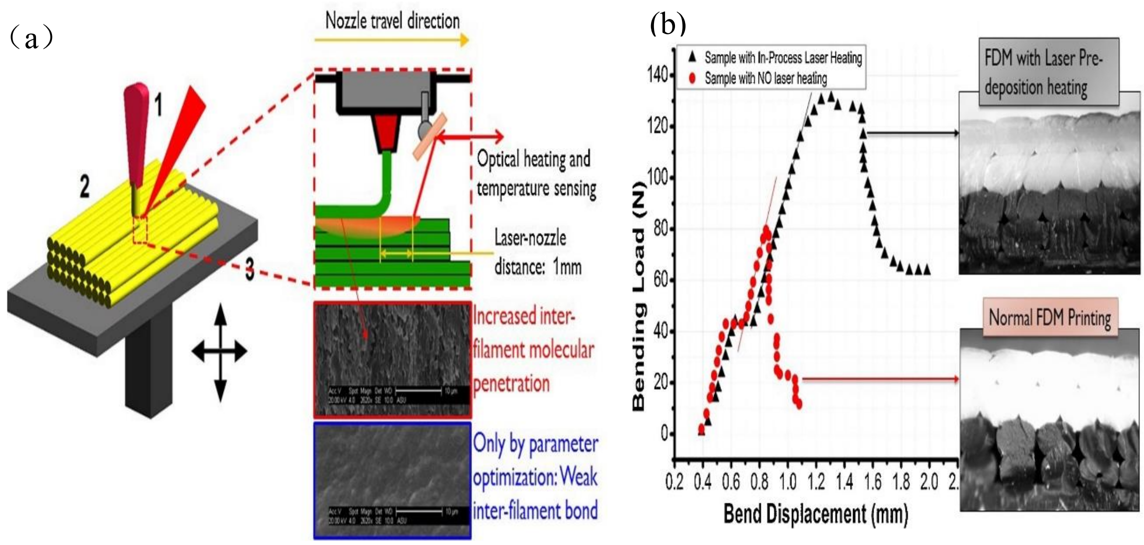

Figure 2.13 The integrated laser pre-heating system to enhance the inter-layer bonding in FDM: (a) the layer fixed ahead of the printing nozzle so that the previous deposited layer can be heat up with higher interface temperatures to allow more polymer inter-diffusion between neighbouring layers; (b) the flexural results show that the laser pre-heated samples had more than 60% increase of strength, around 100% increase of elasticity and more than 3-fold toughness compared to the FDM counterparts without laser treatment. Micrographs demonstrate enhanced filling, contributing to overall better mechanical performance in printed parts [149].

The sequential deposition of fused material layers involves the cooling by convection into surrounding air and the solidification onto the previous layer via heat conduction through the adjacent bead [152]. These rapid cooling cycles exacerbate the non-uniform thermal gradient with irregular heat distribution throughout the printed structure, resulting in the build-up of internal stresses within the deposited layers. A bunch of problems have been caused in the final part by the thermal-induced residual stresses and strains, including dimensional inaccuracy, shrinkage, warping, delamination and even printing failure [153, 154]. The typical warpage in the FDM process can be seen in **Figure 2.14** [155]. For instance, Wang et al constructed a mathematical model for the warp deformation, in which the T_g and linear shrinkage rate have been demonstrated as influencing factors for the appearance of intra-/inter-layer deformation, delamination and cracking [156]. Zhang and Chou developed a 3D model with the introduction of additive feature and stepwise thermomechanical manner to simulate stress distributions and part distortions as a function of several deposition parameters. Results showed that the residual stress was significantly affect by the scan speed followed by the layer thickness while the influence of the road width on the stress accumulation was only effective under the interaction with the layer thickness. The positive correlation between part distortions and these deposition factors derived from this model had a great consistence with the deflection experiment [157]. Assisted by the FEA analysis and element activations, they also found that the toolpath patterns played an important impact on both the magnitude and distribution of residual stresses, in which the primary direction of the designed toolpath guided the stress concentrations. From that simulation, higher residual stresses and larger distortions were observed in short-raster toolpath than those in long- and alternate-raster patterns [158]. Via embedding a fiber Bragg rating sensor into the midplane of FDM samples, Kantaros and Karalekas experimentally verified the sensitivity of residual strains to the deposition orientation in the in-situ solidification test, recording less strains for the beads aligned to the 0° direction than those in transverse and crisscross counterparts [159]. Armillotta et al. studied the influence of part geometries on warpage and found less distortion on very thin parts, which is contradictory to other literature suggesting that a lower z-direction dimension results in lower bending stiffness and thus large warpage. Based on a 1D analytic model, they proposed a different interpretation that a thinner part height can not only facilitate the shrinkage on multiple layers via thermal conduction and contribute to the reduction of internal stresses, but cause plastic deformation of the deposited layers to keep flat on the build plate under bending stresses, opposite to the occurrence of elastic deformation in thicker object that will be recovered as distortion [155].

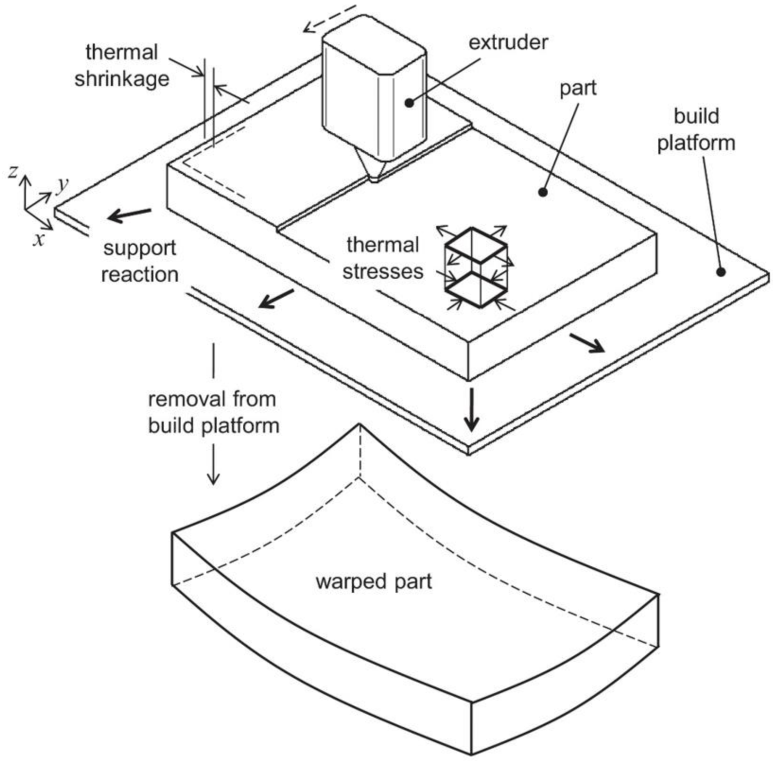

Figure 2.14 The typical warpage in the FDM process due to thermal stresses [155].

According to the above discussion, it is perceptible that considerable variables are involved into the fabrication process of this simple AM technology, including the part geometry (e.g. length, width, height, spatial structures, etc.), material properties (e.g. strength, modulus, Poisson's ratio, T_g, etc.) and processing parameters (e.g. layer thickness, deposition rate, nozzle temperature, chamber temperature, raster angle, bead orientation, number of contours, etc.) [160-162]. The analysis of all these interactive variables cannot be isolated, further increasing the complexity to assess the possible influence of individual factor on the FDM part quality. Last year, the material database 3D-printing grades from DSM was integrated into the FFF process simulation software Digimat, becoming the first commercial modelling tool for AM engineers to predict the behaviour and performance of printed parts so that the optimization of materials, printers and designed geometries can be realized [163]. However, the options in this database are till limited to some basic materials without a good cover for composites.

2.4 Discontinuous FRPC feedstock for FDM

2.4.1 Thermoplastic matrices in FRPC

As was mentioned above, both of HME and FDM processes are built upon the melting and cooling of materials to obtain the desired shape. In a sense, the extrusion-based FDM technology can be deemed as the automatic upgrade of the conventional HME method. Thus, the reversible liquid-solid state change of thermoplastics makes these polymers to be the eligible feedstock for these two manufacturing techniques. Compared to thermosetting resins, these heat-regulated polymers alone or as composite matrices have numerous unique merits, including high recyclability, less hazardous chemical compositions, no curing requirement and ease of mass production [164]. The common thermoplastic polymers that can be utilized as composite matrices for FDM process include acrylonitrile butadiene styrene (ABS), polylactic acid (PLA), high density polyethylene (HDPE), polypropylene (PP), polyamide/nylon (PA), polycarbonate (PC), thermoplastic polyurethane (TPU), polycaprolactone (PCL) and polyethylene terephthalate (PET) [165-168]. The commercially available polymer filaments in the FDM market can be seen in **Figure 2.15** [169]. Among them, ABS and PLA are the most extensively used 3D printing thermoplastic. The former is a tough terpolymer composed of a long polybutadiene chain criss-crossed by short chains of poly (styrene-co-acrylonitrile) and can be printed at high speed while it tends to warp and delaminate when printing large parts. The latter is a biodegradable and biocompatible aliphatic polyester derived from renewable resources (e.g. corn and sugarcane) and harder than PLA. Although it can strongly adhere to the build plate without the need of heating, this polymer is prone to jam in the liquefier owing to its high friction [170]. Other expensive engineering thermoplastics (e.g. poly ether ether ketone (PEEK), poly ether ketone ketone (PEKK), polyphenylene sulphide (PPS) and polyeherimide (PEI)) with higher thermal and mechanical performance can also be printed while specialized AM machines are required, further increasing the fabrication cost [171, 172]. Different with normal FDM printers that are operated at low temperature (≤ 280 ̊C), these specialized printers have better thermal management, higher heating capacity and stronger resistance to high temperature that these engineering thermoplastics need. Hence, FDM processing of these polymers aims to high value-added field like aerospace and biomechanical applications.

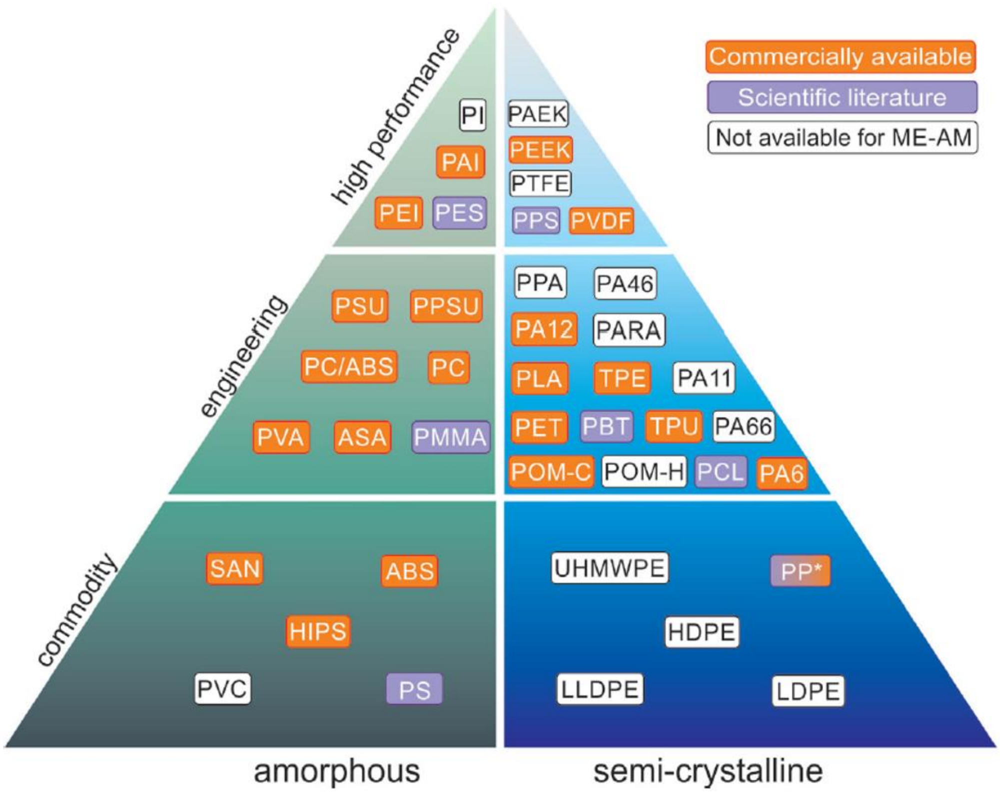

Figure 2.15 Pyramid of polymeric materials as a function of the material availability in FDM market [169].

Most of these thermoplastics are amorphous as their low T_g and large viscous softening range can facilitate the extrusion and deposition of plastic beads. However, amorphous polymers normally have weak chemical resistance and low mechanical performance (e.g. Young's modulus between 1.9 and 2.4 GPa, and elongation at break between 3 and 9%). In contrast, the limited amount of semicrystalline thermoplastics have a drastic change in viscosity due to a very small temperature range for softening. Despite their difficult in FDM processing, these polymers exhibit wider mechanical properties than amorphous counterparts (e.g. Young's modulus between 0.8 and 4 GPa, and elongation at break between 2.5 and 1600%) [169, 173]. In order to make full use of respective advantages from each material, two or more polymers can be blended during the HME of filament. One typical example is ULTEM® 9085 from Stratasys, a blend of PEI and PC. With the incorporation of PC, this commercial filament not only possesses lower Tg for easy extrusion, but presents better flowability, ductility, transparency, strength and stiffness [174]. Due to the high cost of Stratasys ULTEM® 9085 (~200 $/kg), Cicala et al. studied the fabrication of PC/PEI blends by varying the PC content and found that the standard PEI modified with 10 wt% PC outperformed ULTEM® 9085 in terms of thermal and tensile properties, which shows a great potential in the development of polymer blends for better performance [175].

2.4.2 Discontinuous fibers in FRPC

A wide variety of discontinuous fibers with varying sizes have been incorporated into the FDM fabrication of FRPC. According to their source, these fibril fillers can be classified into two categories: synthetic fibers and natural fibers. The former includes carbon fiber (CF), glass fiber (GF), Kevlar and liquid crystalline polymer (TLCP) and the latter has hemp, bamboo, flax, jute, harakeke and wood [176-179]. The synthetic fibers employed for FDM composites have numerous advantages such as lightweight, corrosion resistance, flame retardancy, chemical resistance and superior stiffness and strength while the natural fibers are normally biocompatible, biodegradable, renewable, recyclable and relatively cheap. Since the majority of natural fibers are unstable at temperature ≥200 ℃, polymer matrices that require high processing temperatures in HME and FDM will be not suitable for the manufacturing of AM composites [180]. The mechanical properties for FDM-fabricated discontinuous FRPC has been listed in **Table 2.1**.

As the primary filler, the fiber content plays a crucial role in the overall properties of printed composite parts. By compounding and extrusion of CF/PA mixture via TSE and SSE processes, Liao et al. fabricated the composite filaments with varying fiber contents (0, 2, 4, 6, 8 and10 wt%) and comprehensively characterized the material properties after FDM printing. The high stiffness of CF promoted an upward trend in tensile and flexural performance with the increase of fiber contents while the impact strength presented a sharp loss at low CF contents. This can be attributed to the generation of stress concentrations at fiber ends, initiating the crack propagation. With the increase of CF loading, the crystallization behaviour of PA composites didn't have a big change since the existence of CF acts as not only an inhibitor in the motion and arrangement of molecular chains, but a beneficial nucleating agent to facilitate polymer nucleation. Results also showed the increasing thermal conductivities at higher CF contents due to the establishment of this fiber-induced conductive network. The positive correlation between tensile properties and fiber contents was also observed in the 3D printing of natural fiber (hemp and harakeke) reinforced PP composites by Stoof and Pickering. Nevertheless, the FDM composites had lower strength and modulus than those of feedstock filaments. The lower pressure in FDM process incurred stress relaxation and formed more voids as stress concentrators. Natural fibers also proved to be a remarkable filler to maintain dimensional stability with much less shrinkage [181]. The discontinuous fiber loading in FDM is normally less than around 50% composites because higher contents may decrease the melt flowability and clog the nozzle [182]. In addition, some papers report worse mechanical performance at high fiber loadings owing to the increase of porosity, which indicates the importance to eliminate this defect so that the benefits of fiber incorporation can be maximized [183, 184].

Fiber length is an important factor in the limited improvement of strength for FDM-made discontinuous FRPC. Although initial lengths are long enough to promote the stress transfer from fiber to matrix, the discontinuous fibers are largely shortened by the high shear force in mixing and extrusion of rotating screws during the HME process, resulting in fiber lengths around one order of magnitude lower than the critical length [185]. Instead of fiber rupture under the external loading, these micro-scale fibers in composite filaments as FDM feedstock pull out of matrix without the effective transferring of the applied stress [186]. Moreover, shorter fibers can incur more stress concentrations with increasing fiber ends at the same fiber content [187]. Ning et al. printed ABS composites with the CF lengths of 150 μm and 100 μm and found that the longer fiber endowed the FDM composite with larger tensile strength and stiffness [184]. Tekinalp et al. analyzed fiber length distributions both in FDM- and compression molding (CM)-fabricated samples. Results show that compared to the initial length of 3.2 mm before the HME, the majority of fibers in FDM composites were broken down into the length of less than 0.4 mm. With the increase of CF content, fibers in FDM samples became shorter since more fibers were damaged due to the increasing interaction between these fillers. In contrast, composites made from CM had slightly longer fibers, crediting to the lower shear applied onto the material (**Figure 2.16**) [188]. Blok et al. also investigated the composite printing by respectively using short fiber (~100 μm) and continuous fiber feedstock. Although much higher mechanical performance was observed in continuous FRPC, design freedom was largely compromised with the incapability of free deposition through small steering radii and sharp angles. Filaments with short fibers exhibited better printability and higher degree of design freedom [189]. Undoubtedly, there is a great promise in the production of high performance complex FRPC if the printed fiber length can be increased in this HME+FDM system.

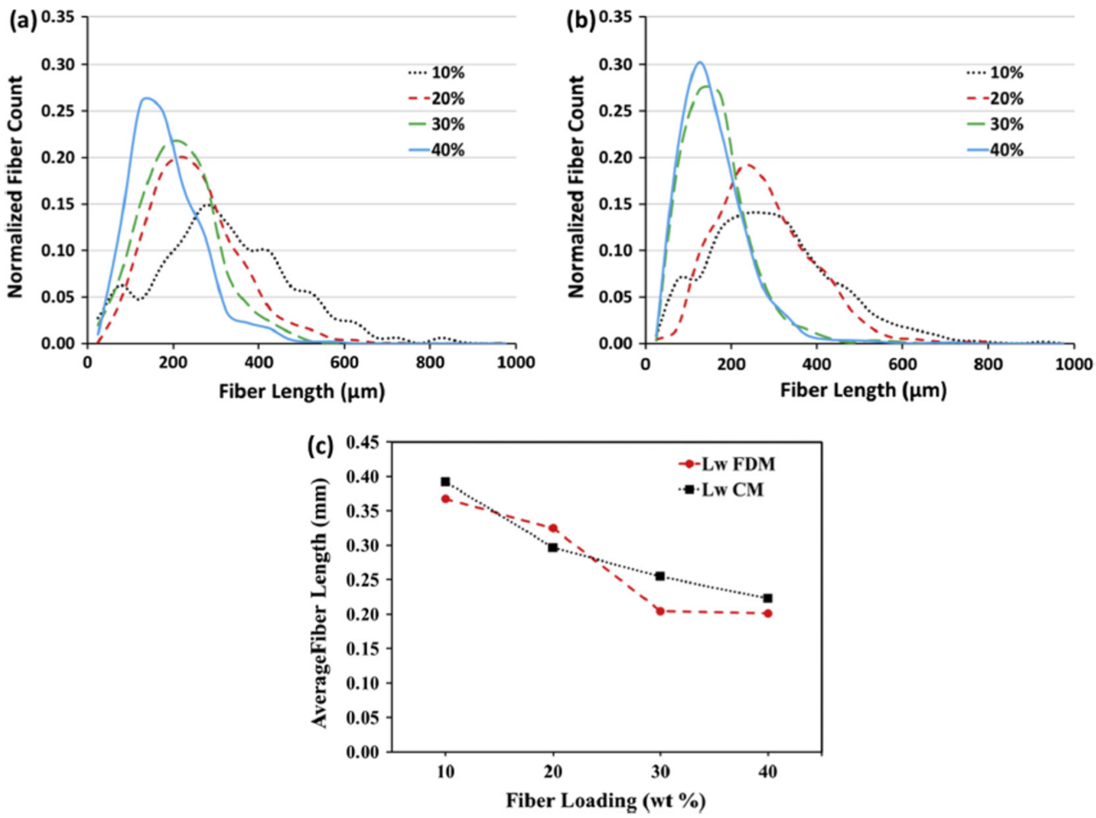

Figure 2.16 Fiber length distributions as a function of varying fiber contents: (a) compression-molded, (b) FDM-printed, and (c) weight average fiber lengths of dog-bone samples [188].

During the extrusion process, a high shear force is generated between the semi-liquid composite flow and the inner wall of nozzle, contributing to the fiber alignment along the printing direction. To be specific, the external force from the feed roller pushes the composite melt into the nozzle with a small diameter, leading to a high velocity gradient and thus great shear stress in the flow direction. Fibers are forced to be aligned along the axis of nozzle so as to reduce the flow resistance. These highly oriented fibers are preserved after depositing onto the build plate due to the fast cooling and solidification [190, 191]. Higher fiber loadings contribute to more uniform fiber alignment. As a result, the anisotropic feature in FDM-based parts is further aggravated with the incorporation of fibers, whether in structural distribution or in mechanical properties. The tensile strength in the build direction normally is only 50-75% of in-plane strength while the fibril fillers increase the anisotropy with the reduction of out-of-plane strength close to 90% [192]. Inspired by the traditional z-pinning concept to improve through-thickness performance and avoid delamination, Duty et al. introduced this scheme into the FDM process, where the part is conventionally printed with staggering seams designed to be z-axis aligned throughout the structure. This length and position of these seams can be controlled and filled by extruded pins prior to the deposition of subsequent layers (**Figure 2.17**). Results showed that the z-direction strength and toughness of printed CF/PLA composites can be enhanced by more than a factor of 3.5, and even higher than x-direction strength after normalizing these values. The printed part with the largest pin volume also demonstrated isotropic properties in mechanical characterization [192]. This strategy builds a new platform for AM designers to customize directional properties that are independent of print orientation.

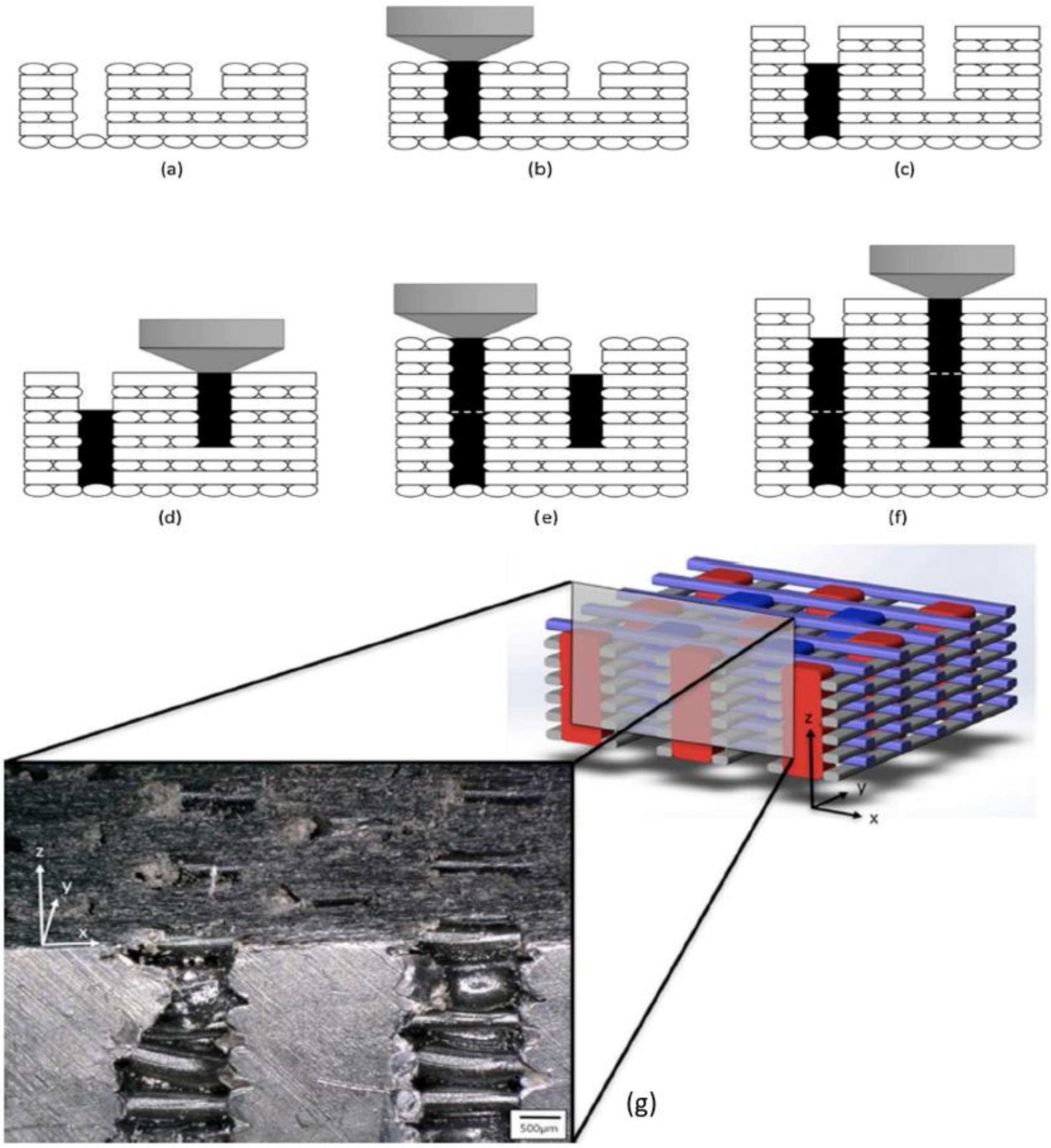

Figure 2.17 . Z-pinning approach for FDM printing mechanically isotropic materials: (a-f) process steps for 3D printing with z-pinning; (g) cross section of printed sample with 120 % pins [192].

The formation of voids has been discussed above as the consequence of insufficient bonding between adjacent beads in FDM process, yielding a detrimental impact on the mechanical properties and structural integrity for the printed parts. Thus, discerning the change of pores and voids after the introduction of discontinuous fibers is essential to ensure the printing quality of FRPC parts. Tekinalp et al. investigated the microstructure of FDM-based CF/ABS composites and found that in addition to the triangular voids on the bead surface, internal voids inside the extruded beads started to form in the printed composites. The size of those relatively large triangular voids became smaller with the addition of fibers, which can be ascribed to the high thermal conductivity of CFs and the decreased die swell at the nozzle, contributing to the improved packing after bead deposition (**Figure 2.18**). As a comparison, the authors also fabricated composite samples with the same feedstock materials via CM method and no visible porosity was observed due to its high pressure operational process [188]. Ning et al. illustrated the same void changes and varieties with the incorporation of CFs into the ABS matrix. Meanwhile, the porosities at different fiber contents were calculated, showing a V shape trend from 0 to 15 wt % CF contents with the lowest value at the 3 wt% fiber loading [184]. Due to the increased stress concentrations from these voids, it to a certain extent explained why a higher CF content didn't impart a better mechanical performance of FDM composites in this paper. The defect of inner-bead voids is mainly caused by the weak interfacial adhesion between fibers and polymer matrix. **Figure 2.19** depicts the inner-bead and inter-bead voids inside the FDM printed fiber reinforced composites. However, higher porosity can facilitate more swelling in printed biocomposites (e.g. wood fiber+PLA matrix), shifting this drawback into an advantage in designing programmable moisture-actuated hygromorph products [193]. Although various plasticizers and compatibilizers have been added to the FDM composite matrices with improved mechanical properties (e.g. flexibility and handleability), few is related to the surface modification of fibers for better interfacial bonding [194-196]. Since most of these fillers are synthetic fibers with no active groups and smooth surface, it's difficult to form a strong fiber-matrix adhesion by merely using the unmodified fibers as the reinforcement. Some reviews have focused on the enhancement of this interphase in conventionally manufactured composites via various surface treatment approaches (e.g. sizing, coating, grafting, etc.) [197-200]. This enlightening information may inspire material researchers, scholars and experts to develop AM-based FRPC with superior fiber-matrix interfacial properties so as to achieve better mechanical, thermal and electrical performance.

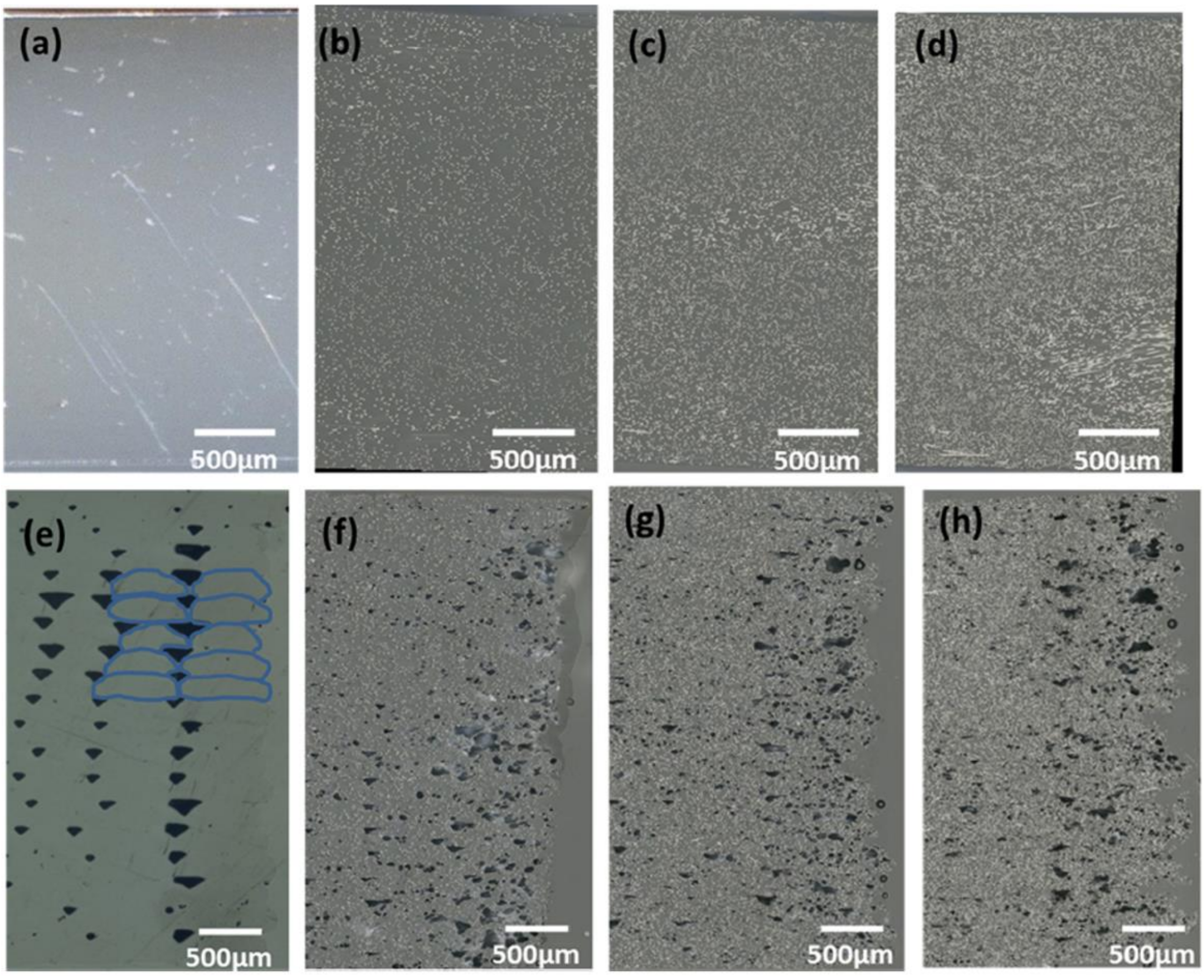

Figure 2.18 Micrographs of polished surfaces of CF/ABS samples fabricated by CM and FDM methods (a) CM neat-ABS, (b) CM10%CF, (c) CM20%CF, (d) CM30%CF, (e) FDM neat-ABS, (f) FDM10%CF, (g) FDM20%CF, and (h) FDM30%CF [188].

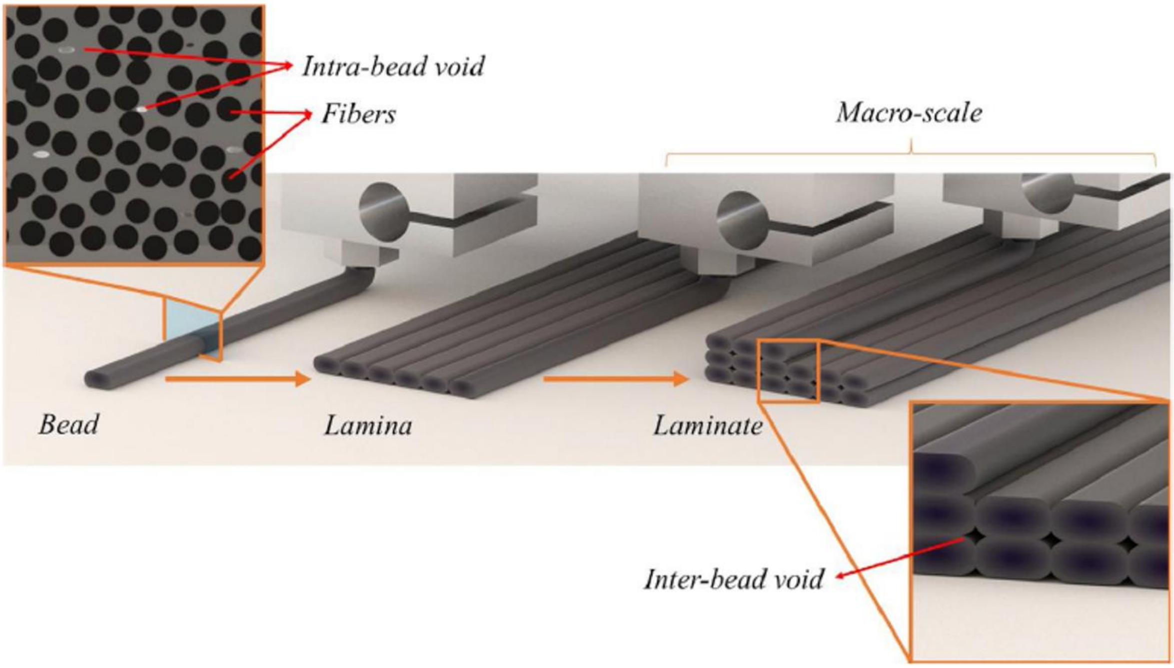

Figure 2.19 The schematic of the multiscale structure of FDM-fabricated fiber reinforced composite parts with inner-bead (intra-bead) and inter-bead voids inside [101].

Apart from the material properties, it is vital to understand the influence of various processing parameters in FDM on the morphology and overall performance of FRPC, including deposition parameters (e.g. infill pattern, infill density, layer thickness, bead width, build orientation, etc), operation parameters (e.g. nozzle temperature, nozzle size and shape, feed rate, print bed temperature, etc.) and ambient parameters (e.g. humidity, temperature, etc.). Based on the own-made 5 wt% CF/ABS composite filament, Ning et al. investigated the tensile properties as a function of raster angle, infill speed, nozzle temperature and layer thickness. Using X axis as the benchmark during printing, raster angle of [0, 90] presented much large tensile strength, yield strength and Young's modules than those from raster angle of [+45, -45], which can be attributed to effective load transfer from the matrix to reinforced CFs. This was also proved from the facture interface after tensile test that fibers were ruptured for [0, 90] samples rather than pulled out for [+45, -45] counterparts. The best infill speed was found at 25 mm/s since faster speeds cause less interaction and poorer intra-/inter-layer bonding between deposited beads. With the altering of nozzle temperature, a peak point for tensile performance appeared at 220 ℃ since beads cannot firmly bonded together at lower temperature while porosity in printed composites increased at higher temperature owing to the polymer degradation. Although 0.25 mm layer thickness contributed to the higher toughness and ductility, tensile strength and stiffness exhibited the best values at the layer thickness of 0.15 mm by virtue of the tighter coalescence between each layer [201]. Shifting bead layout orientations from 45 ° to 0 °, Anwer and Haguib reported higher mechanical performance for TPU composites with varying CF contents from 0 to 4 vol %, suggesting larger stiffness imparted by the fiber at the 0 ° print. To further elucidate the fiber orientation, they observed higher water contact angle from the 0 ° printed composite than that from the 45 ° bead orientation via hydrophobicity test, indicating greater entrapment from the higher fiber alignment at the smaller angle [202]. Jiang and Smith also studied the correlation between tensile properties and bead orientations at four angles (0 °, 45 °, ±45 °, 90 °) relative to the load direction. Compared to the pure polymers, results show that CF reinforced composites in general have higher tensile modulus at all print orientation while less improvement and even a decrease were observed for tensile strength except at the 0 ° print orientation [203]. This could be the low conformity of CFs to the previous layer, thus reducing the contact area for neighbouring layers during printing. This phenomenon has been reflected on the work from Love et al. that the out-of-plane tensile properties of the pure ABS was better than that of CF reinforced composites [204].

Table 2.1 List of mechanical properties for FDM-fabricated discontinuous FRPC.

Source	Polymer matrix	Fiber reinforcement	Fiber content (wt%/vol%)	Initial fiber length (mm)	HME	Tensile strength (Mpa)	Young’s modulus (GPa)

[205]	ABS	CF	5	0.1	SSE	26.5	1.3 (+44 %)
[206]	ABS	CF	10	0.1	SSE	37.4 (+32.6 %)	0.79 (+58.0 %)
[188]	ABS	CF	10, 20, 30, 40	3.2	Ram	~67.0	~14.5
[184]	ABS	CF	3, 5, 7.5, 10, 15	0.1, 0.15	/	42.0 (+23.5 %)	2.5 (+31.2 %)
[201]	ABS	CF	5	/	/	36.8	1.1
[207]	ABS	CF	15	/	/	39.05 (+41.0 %)	5.9 (+141.3 %)
[186]	PLA	CF	15	0.06	/	53.4 (~0 %)	7.5 (+123.4 %)
[192]	PLA	CF	15	/	/	38.2	/
[208]	PLA	CF	15	0.1	/	/	/
[183]	PLA	CF	3, 5, 7, 10	0.1	SSE	~55.0	/
[203]	PLA	CF	12.6	0.07	/	68.4 (+14.0 %)	9.28 (+162.9 %)
	ABS	CF	16.8	0.05		50.9 (+33.2 %)	7.15 (+212.2 %)
	PET	CF	17.7	0.07		68.3 (+48.2 %)	8.47 (+313.2 %)
	Amphora	CF	11	0.05		49.3 (+ 5.1%)	3.93 (+ 95.5 %)

[209]	PEKK	CF	30, 40	/	/	/	/
	PPS	CF	40, 50				
[210]	PA12	CF	2, 4, 6, 8, 10	15-20	TSE +SSE	93.8 (+102.2 %)	3.58 (+265.9 %)
[211]	PA6	CF	/	/	/	~21.0	1.29
[189]	PA	CF	15	0.1	/	83.8	4.6
[202]	TPU	CF	0, 1, 2, 4	/	/	~24.0	~0.64 (+34.07 %)
[195]	ABS	GF	15, 20, 25		TSE	58.6	/
[212]	PP	GF	30	/	/	~39.0	~1.4
[194]	PP	GF	30	/	/	~34.0	~0.4
[213]	PP	TLCP	20, 40	/	SSE	37.0	2.7
[181]	PP	Hemp fiber	10, 20, 30, 40, 50	≤ 8	TSE	22.45 (+31.9 %)	2.00 (+ 181.0 %)
		Harakeke fiber				23.55 (+38.4 %)	2.09 (+193.7 %)
[214]	ABS	Jute fiber	5	/	TSE	25.9	1.54

[193]	PLA+polyhydroxyalkanoate (PHA)	Wood fiber	15.2±0.9	/	/	46.0	3.29

2.4.3 Support materials

The incorporation of support into designed parts is necessary for the printing of complex geometries when overhangs and cavities are suspended in the midair. The increased fabrication freedom also enables designs with freely moving parts inside once the support is removed. Currently, there are three types of support materials employed in FDM: build materials, breakaway materials and soluble materials. The first type is mainly used for single-nozzle printers where the support materials are the same with the thermoplastic filament for the model building while a low-density format is usually chosen for the support so that it can be broken off after printing. Although material compatibility is not existed in this economic approach, more effort is required for support removal and yield poor surface quality, to a certain extent compromising the structural accuracy. The second type is like the first one while a separate polymer material is deposited with the build material. It’s quicker and easier to be peeled off and leave a clean surface without the need of post-processing. Nonetheless, the compatibility of breakaway materials due to their less adhesion is still a concern, especially for multi-material 3D printing [22]. Instead of requiring manual removal, the last type can be dissolved away in the proper solution. They allow for the fabrication of dense and intricate geometries where normal tools cannot reach into the support. Two soluble polymers are widely utilized in this type: polyvinyl alcohol (PVA) and high impact polystyrene (HIPS). The first one is a hygroscopic, biocompatible and flexible thermoplastic that can be directly dissolved into water while the second one has lightweight, rigid and impact resistant properties that needs to use proper chemical solvents like limonene [215, 216]. The main drawback for soluble materials as the support is the long dissolving time. To enhance their removal efficiency in printed parts, some processing strategies have been attempted to improve solvent dissolution, such as the increase of temperature, the application of agitation and/or the introduction of other solvents (e.g. hydrogen peroxide) [217-219]. Up to now, there is no relevant report on the effect of varying support materials on the interlayer bonding with FRPC-based build materials, which is imperative to fulfil the FDM printing of complex composite objects with precise designed dimensions.

CHAPTER 3 MATERIALS AND EXPERIMENTS

3.1 Materials

The materials used in this PhD project includes chopped carbon fiber, carbon nanotube, high density polyethylene and polylactic acid. The main specification for each material has been briefly summarized in **Table 3.1**.

Table 3.1 The brief specifications of experimental mateials

Materials	Propeties
Carbon fiber	Chopped form; ~4.6 mm length; ~7 nm filament diameter, smooth surface
Multi-walled carbon nanotube	Curvy structure; functionalized with hydroxyl group; 20 nm diamter
High density polyethylene	Pellet form; ~3 mm diameter; melt flow index: 0.3 g/10 min; mass density: 0.959 g/cm^3
Polylactic acid	Pellect form; ; ~3 mm diameter; T_g: 55-60 ̊C; T_m: 185-220 ̊C

3.1.1 Carbon fiber (CF)

CF also called as graphite fiber is a lightweight material with superior properties, including low density, low friction coefficient, high specific strengh, high stiffness, remarkable wear resistance and excellent thermal and electrical conductivity. In this research, Chopped long CF with the average length of 4.6 mm was used for a series of experiments, as shown in **Figure 3.1**. This fiber was manufactured from polyacrylonitrile by ACP Composites (Livermore, USA)

Figure 3.1 The chopped CF with the average length of 4.6mm.

3.1.2 Carbon nanotube (CNT)

CNT is the strongest and stiffest carbon material in the world with the maximum Young's modulus of around 1.2 TPa and tensile strengh ranging from 50 to 200 GPa and has already a wide application in practical engineering [220-224]. Although it has been employed in the composite fabriation as a filler, the improvement of mechanical performance is still limited due to the particale bundles and agglomeration. The inhomogeneous dispersion of individual CNT particles impairs the effective stress tranfer from this strong nanomaterial to the polymer matrix. The commercial CNT used here was manufactured via chemical vapor deposition (CVD) technique. It has multiple walls with average diameter of 20 nm and is functionalized with hydroxyle groups (**Figure 3.2**).

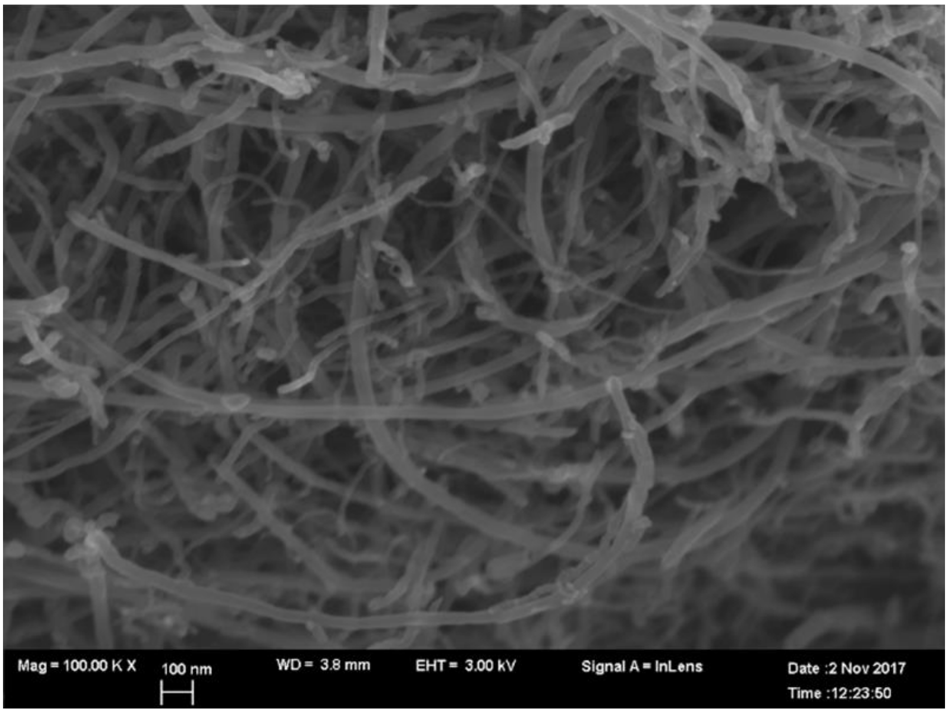

Figure 3.2 Micrograph of CNTs with curvy structures.

3.1.3 High density polyethylene (HDPE)

As a common thermoplastic, HDPE has a higher mass density (~0.941 g/m^3) than normal polyethylene, exhibiting high ductility, strong creep deformation, great impact strength, and excellent resistance in chemicals and corrosion [225]. However, The relatively low strengh and stiffness, to a certain extent restricts its application in some engineering or technical fields. In order to eliminate these drawbacks, various reinforcers have been incorporated into this polymer to increase its overall mechanical performance. The HDPE pellets were purchsed from Qenos (Melbourne, Australia) under the tradename of Alkatane GF7660 with the melt flow index of 0.3 g/10 min (**Figure 3.3**). The mass density and average pellet size were 0.959 g/cm^3 and 3 mm, respectively.

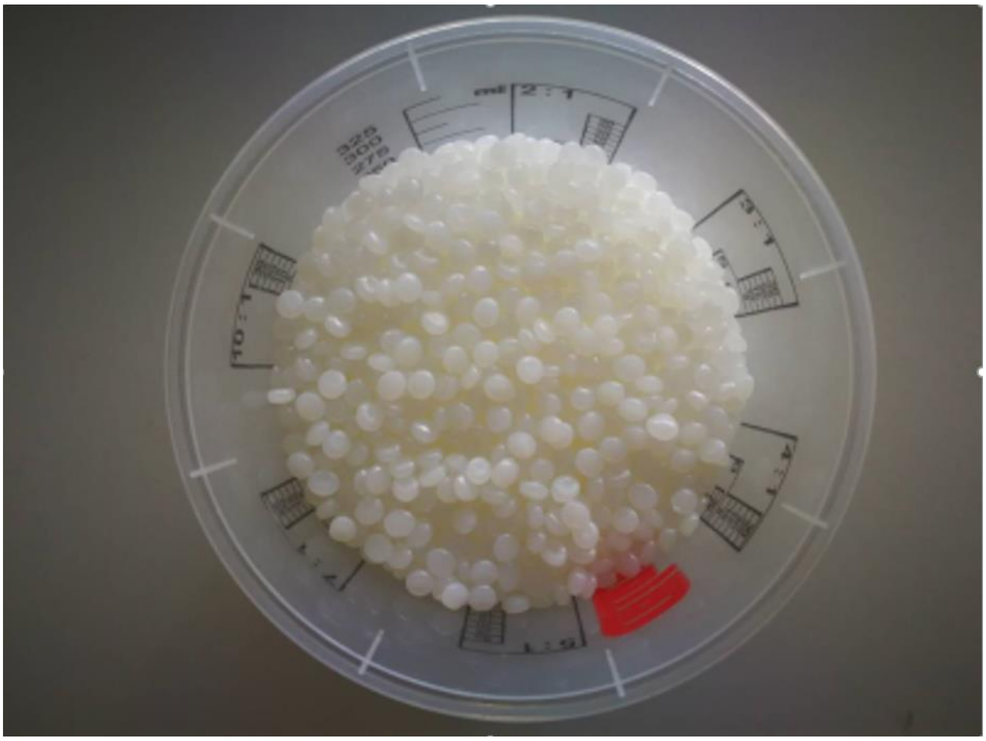

Figure 3.3 HDPE pellets purchased from Qenos with average size of 3 mm.

3.1.4 Polylactic acid (PLA)

As a biocompatible and biodegradable material, PLA is one of the most commonly used thermoplastic in FDM printing other than ABS. Economically produced from renewbale resources (e.g. corn, surgarcane and cassava), PLA emits much less volatile organic compounds (VOC) at the treatment of high temperatures than ABS. Compared to the poisonous substance (i.e. styrene) emitted from ABS, the lower level of main VOC (i.e. methyl methacrylate) from PLA is also much safer to human health, making it to be a green and environment-friendly option for 3D printing [170]. The natural PLA pellets purchased from Aurarum Pty Ltd (Keysborough, Australia) were used as the matrix for the HME fabrication of composite filaments and the following 3D printing. The avarage size for these polymer pellets was 3 mm (**Fig.3.4**).

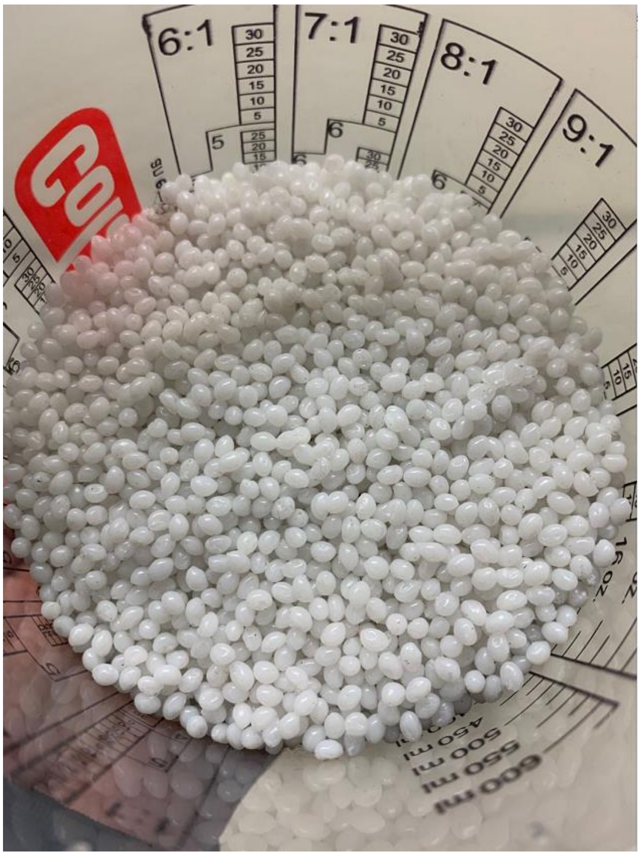

Figure 3.4 PLA pellets purchased from Aurarum with average size of 3 mm.

3.2 Sample preparation

3.2.1 Spray coating

A simple and economic method called spray coating was employed here to modify the surface properties of chopped CFs. Before coating, CNTs were used as the modifier to prepare a homogeneous solution. Since CNTs were inclined to agglomerate in the solution, they will not only impair the uniform spread surrounding the CFs, but block the nozzle of the spray gun during the coating operation (**Figure 3.5**). Thus, ultrasonication technique was used to faciliate the CNT dispersion to obtain a homogeneous suspension. The underlying mechanism of this technique is based on the generation of shock waves from the ultrasound that can separate individual nanoparticles from the accumulated bundles or agglomerates. Ethanol was chosen as the effective solution due to its relatively low viscosity and fast evaporation.

Figure 3.5 The agglomeration of CNTs.

As shown in **Figure 3.6**, the ultrasonic water bath was used for the ultrasonication. 1 mg/ml CNT/ethanol solution was prepared in a mall bottle and then place the bottle in the middle of the water bath for ultrasonication at the frequency of 35KHz for 10 min so that all the CNT agglomerates can be eliminated. The sonication treatment cannot be too long because it may damage the CNTs [220].

Figure 3.6 The homogeneous dispersion of CNTs in the ethanol solution via ultrasonication.

The spray coating system in this project is shown in **Figure 3.7a**, equipped with a air bruch spray gun of 0.2 mm nozzle diameter (**Figure 3.7b**) from Voilamart, Australia. Before coating, chopped CFs were evenly distributed on the plastic membrane and soaked with ethanol in advance to prevent them blowing during spray coating. After that, the ultrasonic treated CNT/ethanol suspension was loaded into the ink cup at the top of the spray gun and spray deposited onto the surface of CFs with the concentration of 1 wt%. The pressure was set at 20 psi with a flow rate of 0.2 ml/s from a 10 cm working distance. It should be noted that the spray coating direction must be perpendicular to the fiber plane. The CFs before and after CNT coatings can be seen in **Figure 3.7c** and **d**. The CNT-coated CFs were dried for 24h to sufficiently remove the ethanol solution before the commencement of hierarchical composite fabrication.

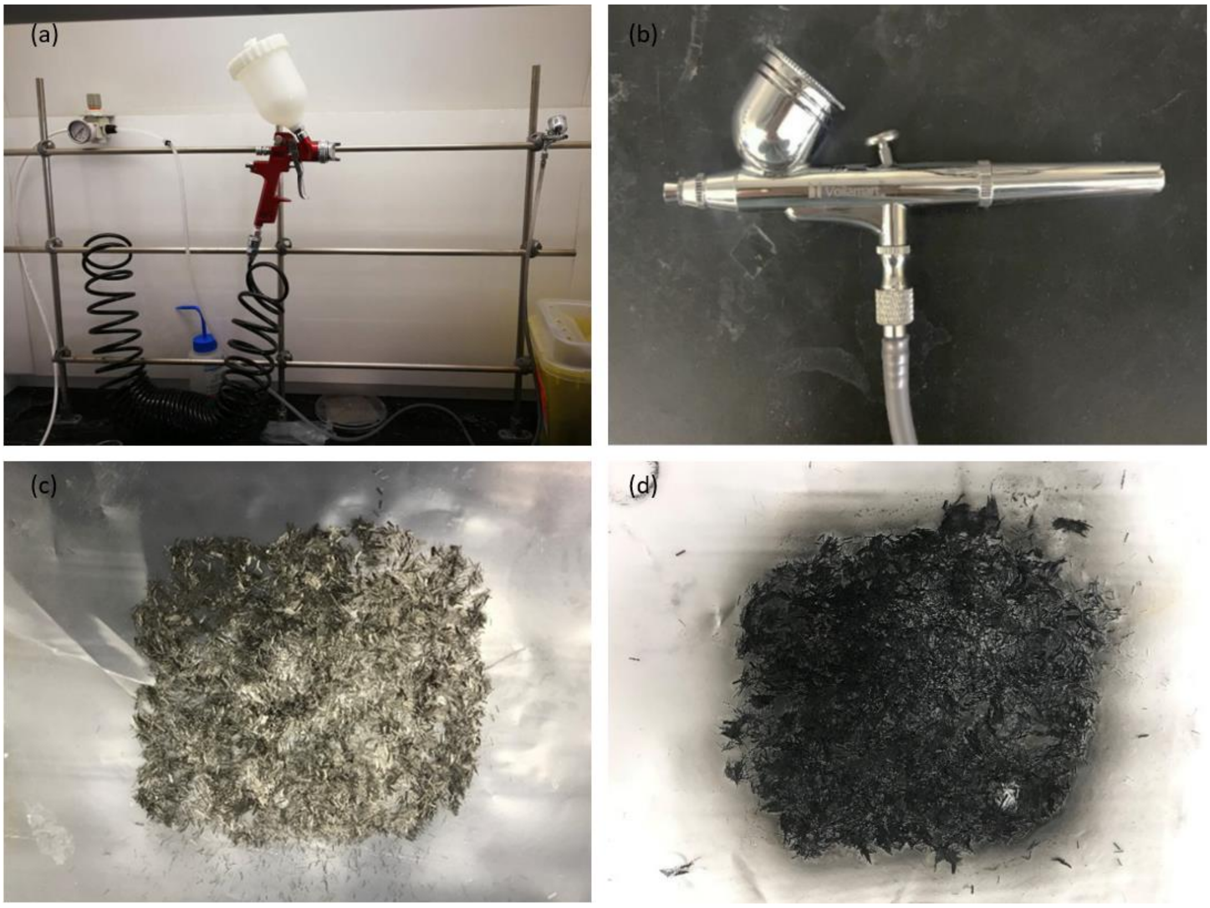

Figure 3.7 (a) The customized spray coating system; (b) the small air brush spray gun employed in this study with a nozzle diameter of 0.2 mm; (c) the evenly distributed CFs before CNT coatings; and (d) the evenly distributed CFs after CNT coatings.

3.2.2 Lab-scale extrusion

The HME machine used here is a lab-scale minature twin screw extruder (WLG10, Xinshuo Precision Machinery, China) composed of an upper cavity plate, a lower cavity plate, two concical co-rotating screws and a circular die (**Figure 3.8**). The maximum working temperature for this instrument is 280 ̊C. The CF filler (i.e. with or without CNT coatings) and HDPE matrix were mixed and fed into the hopper located at the top of the upper cavity plate. With the rotation of these twin screws (60 rpm) at the heated barrel with the setting temperature of 200 ̊C, the composite mixture was gradually melted, compounded and conveyed to the extrusion die, which can be directly connected to the injection molding machine. The mixtures were fully compounded in the extruder for 5 min.

Figure 3.8 The lab-scale miniature twin screw extruder WLG10.

3.2.3 Injection molding

Following the compounding extrusion, the melted material was tranferred to a lab-scale miniature injection molding machine (WZS10D, Xinshuo Precision Machinery, China) consisting of a plunger rod, a gauge plate, a mold core base, a storage vat and a safety testing unit (**Figure 3.9**). During the injection molding process, the melted mixtures were pushed into a mold with the pressure maintained at 980 bars for 10s. the cylinder temperature was set at 200 ℃ so that the material can be kept at melt state while the mold temperature was 60 ℃ to faciliate the solification after injection molding. Samples for tensile and flexural tests (**Figure 3.10**) were fabricated by employing corresponding molds, all these sample can be categorized into two groups:

1. Without CNT coatings: HDPE, 5% CF/HDPE, 10% CF/HDPE, 15% CF/HDPE, 20% CF/HDPE and 25% CF/HDPE

2. With CNT coatings: HDPE, 5% CNT-CF/HDPE, 10% CNT-CF/HDPE, 15% CNT-CF/HDPE, 20% CNT-CF/HDPE and 25% CNT-CF/HDPE

Figure 3.9 The lab-scale miniature injection molding machine WZS10D.

Figure 3.10 Injection molded samples for (a) tensile test and (b) flexural test.

3.2.4 Indutrial-scale extrusion

The large-scale fabrication of CF/PLA composite filaments for the following FDM printing was completed by using an industralized co-rotating twin-screw extrusion line (LTE16-44, Labtech Engineering, Thailand) that consists of a twin extruder for material compunding and extrusion, a water bath for cooling and solidification, a caterpillar haul-off unit for filament dragging and a wind-up unit for filament collection (**Figure 3.11**). Before the HME operation, PLA pellets and varying CF contents was mixed to prepare different feedstock (0, 2.5 wt%, 5 wt%, 7.5 wt%, 10 wt% and 15 wt%). All units in the extrusion line as well as the watch circulation system in the extruder barrel were switched on and the temperatures in the 11 temperature zones of the barrel were set in advance via the computer control center. Around 20 min is needed to fully heat up the extruder. After that, the CF/PLA mixtures were fed into the main hopper through the throat to the barrel, where two screws with the diameter of 16 mm and length/diameter ratio of 44 mm were located inside. The rotation speed for these two screws was set at 25 rpm. With the barrel heating and screw shearing, the melted composite flow was homogenized and conveyed forward to the end of the extruder barrel, where a die with 2.85 mm diameter was installed so that the extruded filament with the same diameter can be achieved for the 3D printing.

Figure 3.11 The industrial co-rotating twin-screw extrusion line LTE16-44.

The semi-liquild extrudate from the die was passed through a long water tank with constant temperature of 20 ̊C to assist the filament cooling and fast solidification. At the beginning, the solified filament was manually dragged to caterpillar unit and then pinched between a set of rollers with the rotation speed controlled at 3.2 m/min so that the continous filament can be transported at a constant rate. Consequently, the fabricated filament was wrapped onto a spool with the wind-up tension of 1Nm. **Figure 3.12** exhibited the neat PLA and composite filaments with varying CF contents. All optimized processing parameters involved into this industrial-scale extrusion have been presented in **Table 3.2**.

Figure 3.12 The neat PLA and PLA composite filaments with varying CF contents.

Table 3.2 Processing parameters involved in the operation of the industrialized twin-screw extrusion line.

Heating zones	Z1	Z2	Z3	Z4	Z5	Z6	Z7	Z8	Z9	Z10	Die
Temperature (ºC)	200	200	200	180	180	180	180	180	180	180	180
Screw speed (rpm)						25					

Water bath temperature (ºC)	20
Hall-off speed (m/min)	3.2
Wind-up tension (Nm)	1.0

3.2.5 3D printing

The FDM instrument used here was a high-end printer Ultimaker 3 (Ultimaker, Netherlands) that has a great printing quality, high flexibility for the regulation of processing paramters, and diverse utility in material options (**Figure 3.13**). Before printing, all samples were designed as STL files via Solidworks and then converted into G-code that can be recognized by the printer. Through using the Cura software, related processing paramters were also set as shown in **Table 3.3**.

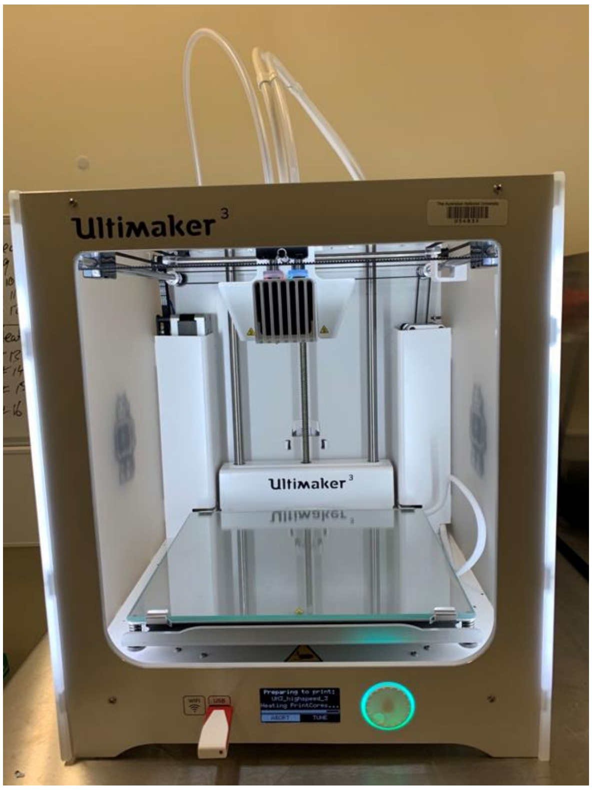

Figure 3.13 The commercial FDM printer Ultimaker 3.

Table 3.3 Processing parameters involved in the FDM printing.

Processing paramters	Values
Nozzle diameter (mm)	0.4
Nozzle temperature (̊C)	200
Build plate temperature (̊C)	60
Printing speed (mm/s)	70
Layer thickness (mm)	0.1
Raster angle (º)	+45/-45
Infill percentage (%)	100

When printing the CF reinforced composite filaments, nozzle could be clogged sometimes. In this circumstance, hot-/cold-pull methods were employed as an effective method to clean the blocked nozzle. Specifically, the nozzle is pre-heated to 200 ̊C and then the pure PLA filament is inserted into the nozzle. By stirring for a while, the PLA filament should be quickly pulled out so that the remaining CF/PLA composite residues can be taken out via the viscous force. If it cannot solve the nozzle clogging issue, cold-pull approach can be conduced in which once the PLA filament is inserted into the nozzle, firmly hold the filament and decrease the temperature to around 25 ̊C. Due to the material solidification at low temperature, the CF composite residues can be coalesced with the pure PLA filament and easily removed from the nozzle. Besides, in order to prevent warping and enhance bed adhesion of printed samples, the raft was added at the bottom of the structrue and can be easily peeled off after printing. The printed samples for chapter 5 can be seen in **Figure 3.14** which were based on the ASTM D638 and ASTM D790 while auxetic samples with various chiral structrues for chapter 6 can be viewed in **Figure 3.15**.

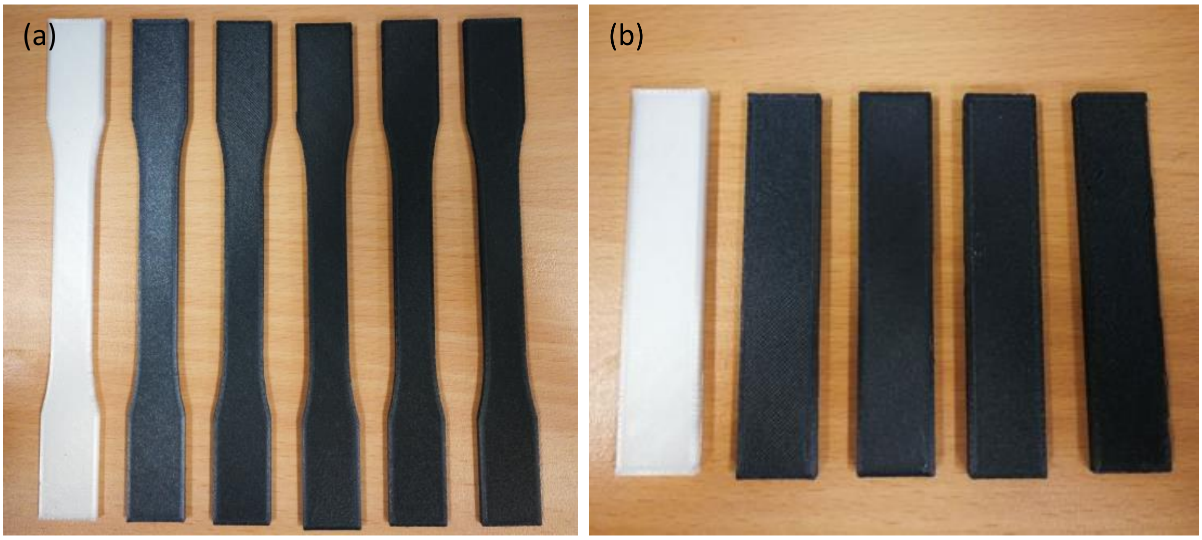

Figure 3.14 FDM printed samples for (a) tensile test and (b) flexural test.

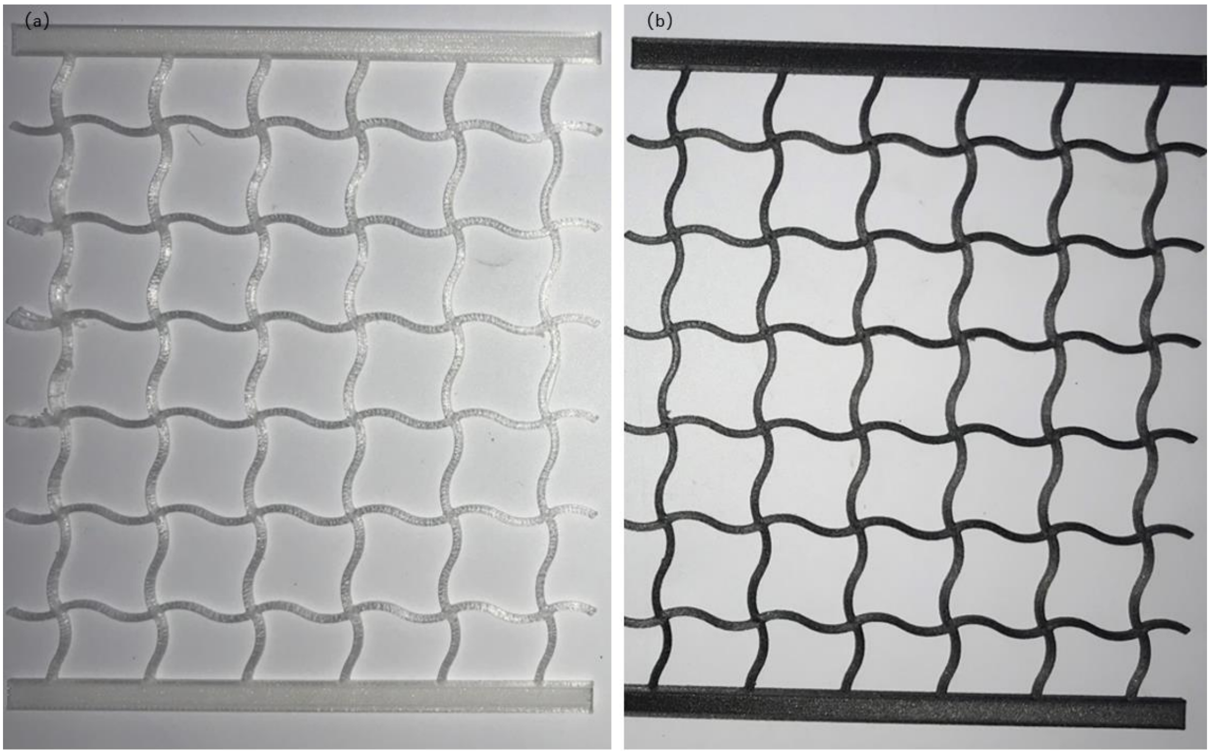

Figure 3.15 FDM printed (a) neat PLA and (b) CF/PLA composite with chiral structures.

3.3 Sample charaterization

3.3.1 Tensile test

The tensile tests in the chapter 4, 5 and 6 were respectively conducted in three universal testing systems: MTS CMT 5205 of SANS from China, model 4505 of Inston from United States and Zwick Z010 of Zwick GmbH from Germany. Although different testing machines were utilized, the basic principle for tensile test is the same. The sample was firmly mounted on the upper and lower clamps of the machine so that it didn’t slide during the test. The distance of these clamps was set at the right values according to each testing standard. The load cells and crosshead speeds used in each chapter can be refered to **Table 3.4**. The force-displacement data was recorded during the sample stretching until failure. The test of each specification was repeated for 5 times.

Table 3.4 The main processing parameters involved in three universal testing systems.

Universal testing system	Load cell (kN)	Crosshead speed (mm/min)
MTS CMT 5205	10	5
Inston 4505	5	5
Zwick Z010	10	5

3.3.2 Fexural test

Same universal testing systems and processing paramters were employed for flextural tests in Chapter 4 and 5. Before testing, the rectangular beam sample was mounted in a three-point bending test system, as shown in **Figure 3.16**. Upon securing the sample, the load was applied to push it upwards against the upper pin until the sample integrity started to fail with the occurrence of structural fracture. The force-displacement data was recorded during the test and 5 repeats for each specification were conducted.

Figure 3.16 The setup of three-point bending for the flexural test.

3.3.3 Hardness test

The principle of hardness test is built upon the measurement of an indent size on the surface of a tested sample under an indenter with a specific load, which reflects the resistance to shear and scratching. Two types of hardness tests were conducted for samples in chapter 4 and 5 by respectively using a micro-hardness Vickers tester (HVS-1000, Jiming, China) and a Rockwell hardness tester (model DXT, Matsuzawa, Japan), as shown in **Figure 3.17**. The main processing parameters involved in these two tests have been give in **Table 3.5**. During the test, the sample was placed onto the instrument table and moved closely to the tip of the indenter. Then, the load of the dentation and the loading time were set through a control panel so that the hardness of the sample can be measured at proper values, which can be directly recorded from the instrument. Data with ten replicates were measured and averaged for each sample.

Table 3.5 The processing parameters involved in the two hardness testers.

Hardness tester	Indenter shape	Load	Loading time (s)
Vickers	Pyramid	50gf	15
Rockwell	Ball	10Kg	10

Figure 3.17 Two types of hardness testers: (a) Vickers tester for chapter 4 and (b) Rockwell tester for chapter 5.

3.3.4 Full-field deformation test

In the tensile test reported in Chapter 6, the real time full-field deformation process of varying chiral structures was recorded via a 2D digital image correlation (DIC) system, which is composed of ARAMIS v6.3.1 (GOM mbH, Germany) and VIC-2D (CSI, USA) (**Figure 3.18**). Before loading the sample into the universal tester, 2 mm-thick aluminium sheets were used to clamp the top and bottom ends of the chiral structure. Special black and white paintings were also sprayed onto the polished front surface through an airbrush to create speckle patterns.

During the test, three images were taken every second via the camera to record the deformation evolution during the quai-static tensile test until the sample was fractured with the peak force decreased by 20%. The CCD camera for the image shooting was equipped with a lens of 50 mm focal length and possessed 2448 × 2050 pixels. The facet size and facet step were set to be 9 × 9 pixels and 5 × 5 pixels to ensure the accuracy in calculating the deformation of the front view for these chiral samples.

Figure 3.18 The full-field deformation test via a 2D DIC system during the tensile test.

3.3.5 Differential scanning calorimetry (DSC)

As the most popular thermal analysis technique, DSC can provide quantitative heat information by measuring the difference of heat flow rate for the target material under a controlled temperature program. It has been widely applied in the thermodynamic study of polymer-based materials by virtue of its capacity to assess the glass transition temperature, melting temperature, crystallization temperature, degree of crystallization and heat of fusion by merely requiring miligram quantities of samples [226]. The thermal behavior was measured in chapter 4 via a DSC instrument (DSC 204, NETZSCH, Germany), as shown in **Figure 3.19**. Around 10 mg of the granulated sample was extracted from the molded HDPE composite. The neat HDPE polymer was used as a control. The chamber was full of inert gas (i.e. nitrogen). Samples were first heated from 40 to 200 °C with 10 °C/min increments, and then maintained at this temperature for 5 min so as to eliminate the influence of heat history. During the cooling process, the same scanning rate was employed until the temperature decreased to 40 °C to assist the analysis of the crystal temperature and crystallinity. All these samples were scanned again from 40 to 200 °C with the same increments in order to investigate their melting conditions. According to the DSC results, crystallinity can be calculated by using the equation in section 4.2.4.

Figure 3.19 The DSC 204 instrument for thermal analysis.

3.3.6 Thermal conductivity

The thermal conductivity of neat PLA and CF/PLA composites fabricated by FDM in Chapter 5 was measure by using a customized setup which follows the ASTM E1225 and D5470 standards (**Figure 3.20**). In this setup, the body was mainly composed of two aluminium blocks and a top attached resistor so that heat can be generated by connecting to a power source and conducted from the top block through the firmly clamped sample in the middle to the bottom block. The temperature difference and heat flux between these two aluminium blocks can be measured via the corresponding thermocouples that were inserted into 1 mm holes of the blocks, as labelled in **Figure 3.20**. To minimize the heat loss during the test, four pieces of extruded polystyrene (XPS) foam boards were used to encompass the experimental setup, creating an insulated environment. The bottom black area was submerged into ice water during the test to quickly dissipate the heat received from the heat source. The measure values can be inputted into the equation in section 5.2.4 to calculate the thermal conductivity.

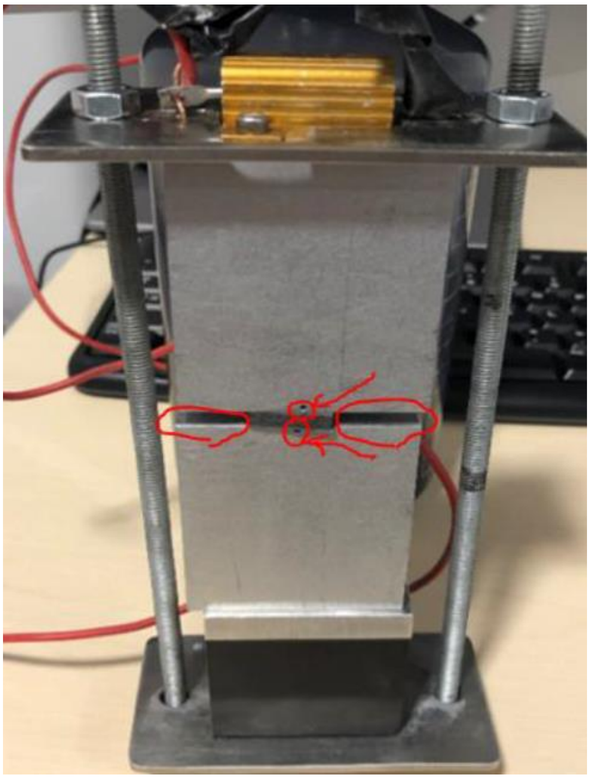

Figure 3.20 The customized setup for the measurement of thermal conductivity.

3.3.7 Scanning electron microscopy (SEM)

SEM ia a powerful and versatile tool to examine and analyze the microstructural features of a solid object. In this experiment, two SEM instruments were utilized for the observation of samples from Chapter 4 (SU-1510, HITACHI, Japan) and Chapter 5 (GeminiSEM 500, ZEISS, Germany). The more advanced GeminiSEM was shown in **Figure 3.21**. Before the morphological characterization, samples were secured to a small stub by using carbon tape and then sputter coated with a thin layer of gold so as to to prevent the charging effect on the surface with enhanced electric conductivity for SEM imaging (**Figure 3.22**). The electric voltage in both SEM instruments were set at 15 kV. Images with varying magnifications were taken for the fractural analysis thereinafter.

Figure 3.21 The SEM observation for fractural suface of sample via GeminiSEM 500.

Figure 3.22 The stub fixed samples with gold coating for the fractural observation.

CHAPTER 4 THE FABRICATION AND CHARACTERIZATION OF HIGH DENSITY POLYETHYLENE COMPOSITES REINFORCED BY CARBON NANOTUBE COATED CARBON FIBERS

4.1 Introduction

Carbon fiber (CF) reinforced polymer composites have been widely used in automotive, aerospace and construction industries by virtue of their ease of fabrication, low density, economy and remarkable mechanical performance [227]. This can be largely ascribed to the superior properties of the reinforcer CF, such as high modulus, high specific strength, and outstanding thermal and electrical conductivity [197, 228]. As is well known, apart from internal intrinsic characteristics of the reinforcement and the matrix, the resultant performance of the composites is also, to a large extent, modulated by the interfacial adhesion between these two phases. A strong interfacial bonding contributes to the efficient load transfer from the matrix to the fiber, which largely avoids the occurrence of stress concentrations and enhances the overall mechanical performance [229, 230]. Furthermore, the interfacial properties of the fiber-matrix entities play a crucial role in fracture toughness, compressive strength and strain to failure, fatigue resistance, impact strength and damage initiation threshold [231, 232]. However, due to the non-polar and chemically inert structure with highly crystallized graphitic basal planes, the CF normally has low surface energy and poor wettability, leading to the weak interaction with the majority of polymers [233, 234]. Various methods have been applied to improve the CF adhesion in the polymer matrix.

With respect to the in-plane properties of laminated composite materials, the fiber reinforcement can provide sufficient strength for many practical applications, while for the out-of-plane (i.e. through thickness) properties, the matrix usually becomes the main restraining factor for the holistic enhancement of fiber reinforced laminated composites [235, 236]. Existing techniques such as z-pinning, stitching and braiding have been applied for the interfacial improvement [237]. However, these methods not only increase the additional manufacturing complexity and cost, but simultaneously compromise the in-plane strength. Therefore, fiber or matrix modifications via the introduction of nanoscale additives open up a new avenue for the improvement of interfacial properties without increasing the overall volume of the composite. Numerous researches have been carried out in recent years in developing nano-engineered hierarchical composite materials where nanoscale additives (e.g. alumina, titania and silica) are finely integrated with fibers by employing ‘wet’, ‘dry’, ‘multi-scale’ or ‘multi-functional’ surface modification methods (**Figure 4.1**) [233, 238-240].

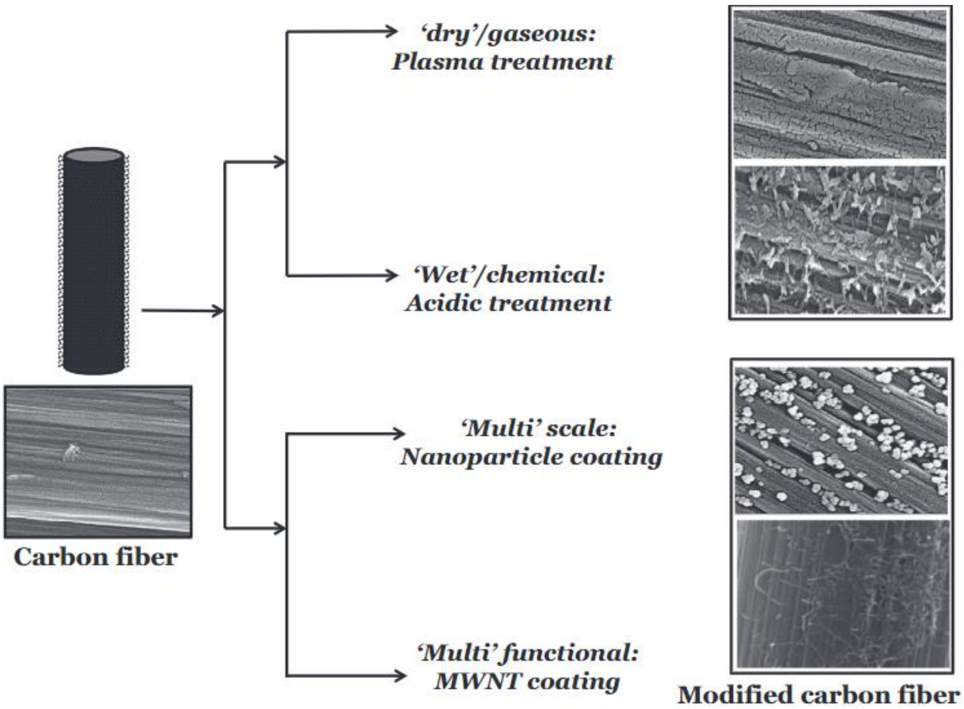

Figure 4.1 The Schematic for fiber surface modification methods (e.g. CF). SEM images showing the fiber surfaces after surface treatments [233].

Of all these nanofillers, the exploitation of carbon nanotube (CNT)—seamless cylinders of one or more layers of graphene with open or closed ends—is undoubtedly a big current interest in creating hierarchically reinforced composite structures [241, 242]. Based on their unique spatial structures and remarkable strength and modulus, substantial improvements for the fiber-matrix interfacial strength and matrix dominated through-thickness performance have been achieved in CF reinforced composites, such as impact strength, fracture toughness, interfacial shear strength and fatigue life [241, 243]. In general, CNT engineered hierarchical composites can be fabricated via two approaches: incorporation of CNT into the matrix or direct adherence of CNT onto the reinforcing fiber surface [244]. The first approach is normally limited to low concentrations of the nanofillers. With the loading increase of CNT, the matrix will become increasingly viscose, leading to the difficulty of efficient dispersion of CNT into the matrix and sufficient filtration of the matrix into fiber reinforcement [245]. Another drawback existing in the addition of CNT into the matrix is the limited capacity of interfacial adhesion between the fiber surface and the nanoscale reinforcement [246]. Besides, the curviness and agglomeration of CNT in the matrix may reduce the effective stiffness of the nano-reinforced composites [247]. Thus, more researchers have shifted the related study to directly incorporate CNTs into fibers or fabrics. Four different strategies can be identified for the direct integration with reinforcement phase: (1) epitaxial growth of CNT from the fiber surface via chemical vapor deposition (CVD); (2) electrophoretic deposition (EPD) of CNT on the fiber surface; (3) chemical bonding between group-modified CNT and fibers; (4) spray coating of fibers and fabrics by CNT contained suspensions [248-250]. As a result, Kepple et al. reported the enhancement of interlaminar fracture toughness by around 50% via in-situ growth of functionalized CNT onto CF fabrics [251]. Via EPD technique, Yao et al. deposited CNT onto the surface of CF, spurring a significant increase (58.6%) of fiber-epoxy interfacial adhesion [252]. Sui et al. also found that the hierarchical CNT/CF/epoxy composite fabricated by continuous electrophoretic deposition method brought 33%, 10.5%, 9.5% and 4.5% increases in interfacial shear strength, interlaminar shear strength, flexural strength and residual bending strength, respectively [253].

However, some of these techniques have internal disadvantages when depositing CNTs onto fibers and fabrics. Due to high processing temperature and reaction of catalyst with fiber surface in the CVD process, both the existing sizings around fibers during their manufacture and the tensile strength of the resultant composite are damaged, let alone the less flexibility in tuning the adhesion between CNT and fibers [254]. The operational principle underlying the EPD technique also necessitates the possession of electric conductivity for the substrates, which to a certain extent limits the application of this method [255]. Furthermore, the complicated steps and cost involved in some of these techniques largely decrease the productivity and their potential for scale-up. Compared to these methods, the CNTs deposition by coating approach shows a great promise because of its easy operation and no harm to fibers (even able to heal surface defects and improve tensile properties) [256-258]. It also does not need complex chemical modifications for pristine CNT during the coating process, which is usually the prerequisite for other deposition techniques. By the spray coating method, CNT can be localized onto damage prone areas rather than deposited throughout the entire composite structure, enabling the fabrication of nano-engineered hierarchical composite systems with tunable CNT distribution for improved material performance [259, 260]. Consequently, the spray coating technology for CNTs deposition onto fibrous reinforcement has the most feasibility for large-scale industrial production.

In this work, CNT with remarkable mechanical, electrical and thermal properties was employed to create a hierarchical CNT-based CF reinforced HDPE composites. As a thermoplastic polymer, HDPE has numerous merits, such as high impact strength, low friction coefficient, low density, excellent chemical resistance, and good fatigue resistance. Nevertheless, the strength and stiffness still need to be improved for the potential engineering applications. To the best of our knowledge, no related report has been published regarding the effects of CNT coating on the extrusion of CF reinforced thermoplastic composites. Via spray coating technique, CNT was deposited onto the surface of CF and then compounded into CNT/CF/HDPE composites by extrusion and injection molding (**Figure 4.2**). The interfacial properties of the hierarchical composites were compared to the counterparts without CNT coating. In addition, the resultant nano-engineered composites were investigated in terms of mechanical, thermal and morphological characterizations.

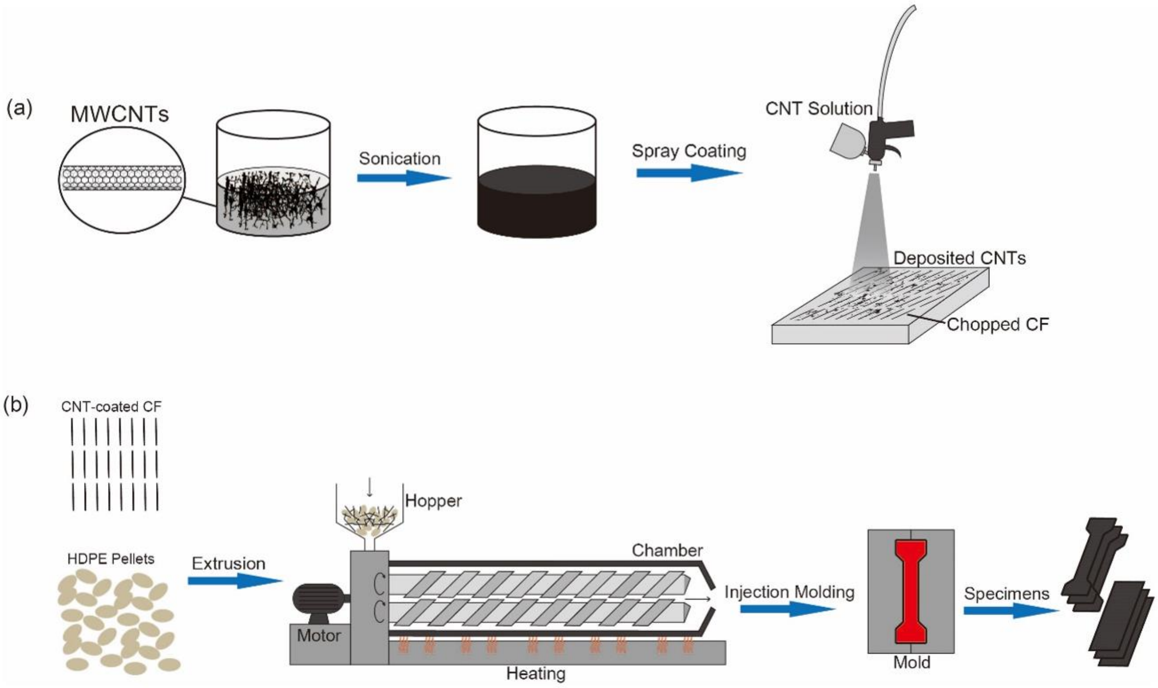

Figure 4.2 Schematic for the fabrication of hierarchical CNT-CF/HDPE composites: (a) spraying coating of CNT onto CF and (b) extrusion and injection molding of CNT-coated CF/HDPE composites.

4.2 Methodoloy

4.2.1 Materials

The HDPE pellets were purchased from Qenos (Melbourne, Australia) under the tradename of Alkatane GF7660. The melt flow index (190 ℃， 2.16 Kg) was 0.3 g/10 min according to ASTM D1238. The mass density and average pellet size were 0.959 g/cm^3 and 3 mm, respectively. The polyacrylonitrile-derived CF in chopped form was purchased from ACP Composites (Livermore, USA) as the reinforcer. Its average length was 4.6 mm. The commercial functionalized MWCNTs with hydroxyl groups were manufactured by CVD technique and their average diameter was 20 nm.

4.2.2 Spray coating

Prior to spray coating, 1mg/ml CNT/ethanol suspension was prepared by using an ultrasonic water bath (WUA-A09H, Thermoline Scientific, Austalia) to eliminate the agglomeration of CNTs. The ultrasonication was lasted for 10 min at the frequency of 35 KHz. Due to the light weight of chopped CFs, ethanol soaking was applied to them in advance to prevent the CFs blowing during the spray coating process. Then, the ultrasonic treated CNT/ethanol suspension was loaded and spray deposited onto the surface of CFs with 1 wt.% concentration by utilizing an air spray gun (Voilamart, Australia). The pressure was set at 20 psi with a flow rate of 0.2 ml/s from a 10 cm working distance. The CNT-coated CFs were dried for 24 h before the commencement of hierarchical composite fabrication.

4.2.3 Extrusion and injection molding

The fillers (i.e. uncoated CFs or CNT-coated CFs) and matrix (i.e. HDPE) with different ratios were fed into a laboratory scale miniature twin-screw extruder (WLG10, Xinshuo Precision Machinery, China), where the screw speed and barrel temperature were set at 60 rpm and 200 ºC, respectively. The mixtures were compounded in the extruder for 5 min and then transferred to the injection molding machine (WZS10D, Xinshuo Precision Machinery, China). During the injection molding process, the pressure was maintained at 980 bars for 10 s. The cylinder temperature was set at 200 ºC and the mold temperature was 60 ºC. Samples for the following tensile and flexural tests were fabricated by employing corresponding molds. All these samples can be categorized into two groups:

1. Without CNT coatings: HDPE, 5% CF/HDPE, 10% CF/HDPE, 15% CF/HDPE, 20% CF/HDPE and 25% CF/HDPE

2. With CNT coatings: HDPE, 5% CNT-CF/HDPE, 10% CNT-CF/HDPE, 15% CNT-CF/HDPE, 20% CNT-CF/HDPE and 25% CNT-CF/HDPE

4.2.4 Characterization

Both tensile test and flexural test for PE and composites were performed at a crosshead speed of 5 mm/min by using a universal testing machine (MTS CMT 5205, SANS, China). The tensile strength, modulus and elongation at breakage were measured in accordance with GB/T 1040 (sample size: 75 mm×10 mm×2 mm) while the flexural strength and modulus were measured in accordance with GB/T 9341 (sample size: 80 mm×10 mm×4 mm). Five parallel samples for each composition were employed in the tests above. The Vickers hardness was determined under the ambient conditions by utilising a micro-hardness tester (HVS-1000, Jiming, China). The load of 50 gf was applied for 10 s. Data with ten replicates were measured and averaged for each sample.

The crystallization behaviors were examined by using a differential scanning calorimeter (DSC 204, NETZSCH, Germany). The granulated samples were extracted from the cross-section of extruded plates with the averaged weight of 10 mg. They were first heated from 40 to 200 °C with 10 °C/min increments, and then maintained at this temperature for 5 min so as to eliminate the influence of heat history. With the same scanning rate, these granulated samples were then cooled down to 40 °C so as to analyze the crystal temperature and crystallinity. All these samples were scanned again from 40 to 200 °C with the same increments in order to investigate their melting conditions. Nitrogen was applied as the chamber gas. According to DSC results, the crystallinities X_c of PE, CF/HDPE and CNT-CF/HDPE composites were calculated via the following equation:

$$X_c = \frac{\Delta H_m}{(1-w)\times\Delta H_m^0} \times 100\% \qquad (1)$$

where ΔH_m is the melting enthalpy after thermal history, ΔH^o_m is the enthalpy of 100% crystallization of HDPE, which is 293.6 J/g, and w is the filler ratio of composites.

The surface morphology of CF and the fracture morphology of CF/HDPE composites were observed by employing a scanning electron microscope (SEM; SU-1510, HITACHI, Japan) with the acceleration voltage of 15 kV. All samples were sputter-coated with gold before analysis so as to increase the electric conductivity and SEM resolution.

4.3 Results and discussion

4.3.1 Mechanical properties

The results of tensile tests for pure HDPE, CF/HDPE composites and hierarchical CNT-CF/HDPE composites with varying CF contents were listed in **Figure 4.3**. Compared to the pure HDPE polymer, the tensile strength of CF/HDPE composites exhibited an obvious upward trend, increasing from 29.82 MPa to 50.88 MPa by 70.62% (**Figure 4.3a**). This result can credit to the high strength and modulus of CF as the filler having higher stiffness than the matrix normally can enhance the mechanical properties of composites [261]. Same increasing trend was also clearly observed for the variation of tensile modulus of CF/HDPE composites relative to the pure HDPE (**Figure 4.3b**). Another important reason for this phenomenon was the usage of long reinforced fiber in the composite fabrication. In general, the fiber with a critical length is required so as to facilitate the stress transfer from the matrix to the fiber via shear transfer mechanism [262]. Short fibers not only have much lower efficiency to transfer the stress, but yield more stress concentrations with increasing fiber ends at the same fiber content [187]. Both of these are detrimental to the ultimate mechanical performance. Consequently, the chopped CF utilized in this research was long chopped CF with the average length of 4.6 mm, which exceeded the normal length of reinforced fibers incorporated into the thermoplastic composite fabrication.

In addition, the tensile strength and modulus also gradually increased for CNT-CF/HDPE composites with the rise of CF contents (**Figure 4.3a** and **b**). Although the two tensile indicators increased for these two groups of composites, the values observed for CF/HDPE composites with CNT coatings were higher than those from uncoated counterparts. The introduction of CNT produced positive effect on the tensile properties by virtue of its improvement in the interfacial bonding between CF and HDPE. With the good adhesion between reinforcement and matrix, the stress transfer capacity of the composite was improved in terms of the reduction of mutual debonding. Compared to the pure HDPE, the elongation at break corresponding to the maximum displacement decreased with the increase of CF contents. It might be explained that the ductility of HDPE matrix was offset by the high stiffness of CF. Meanwhile, after the CNT modification, the stronger adhesion at the interphase of CF and matrix further decreased this value at the same fiber content.

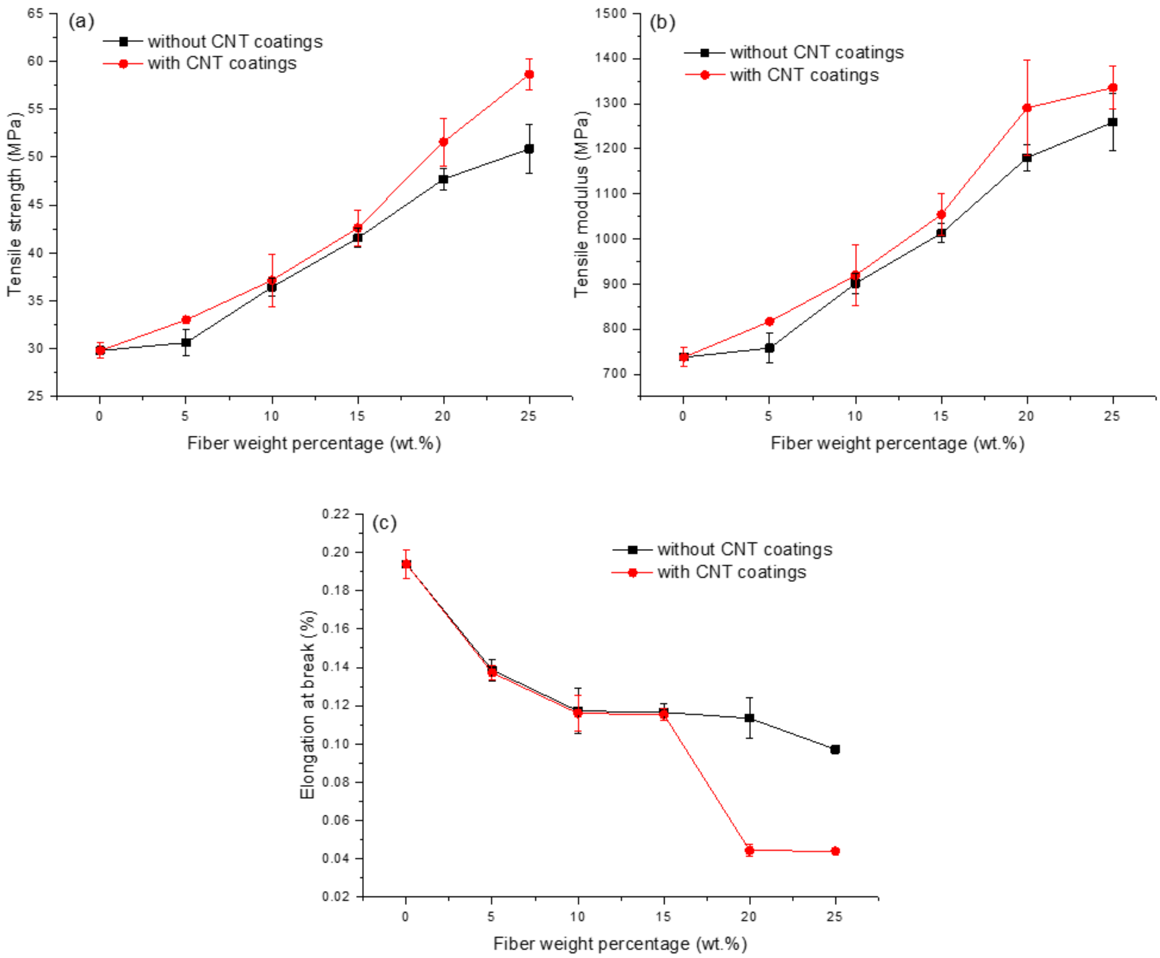

Figure 4.3 Tensile properties of CF/HDPE composites without and with CNT coatings: (a) tensile strength, (b) tensile modulus and (c) elongation at break.

The flexural stiffness and strength are extremely important for composites to prevent the potential deformation and bending failure while subjecting to high load and sliding velocity. Based on this consideration, the flexural properties of pristine HDPE and CF/HDPE composites with and without CNT coatings were also explored by three-point flexural test. As can be seen from **Figure 4.4**, the flexural strength and modulus showed the same tendency with the tensile strength and modulus, while the tensile strength was comparatively higher than the flexural strength. With the increase of CF content, the flexural strength and modulus from both untreated and CNT-coated CF/HDPE composites increased apparently compared to the pure polymer while the hierarchical CNT-CF/HDPE composites possessed higher values than uncoated composites. When CF content reached 25 wt.%, the flexural strength and modulus of CNT-coated composites climbed to 392.76 MPa and 1309.19 MPa, which are 25.89% and 19.79% higher than those from untreated counterparts. Likewise, all enhancements in flexural performance can be attributed to the high stiffness of CF and improved interfacial bonding between the reinforced fibers and the matrix.

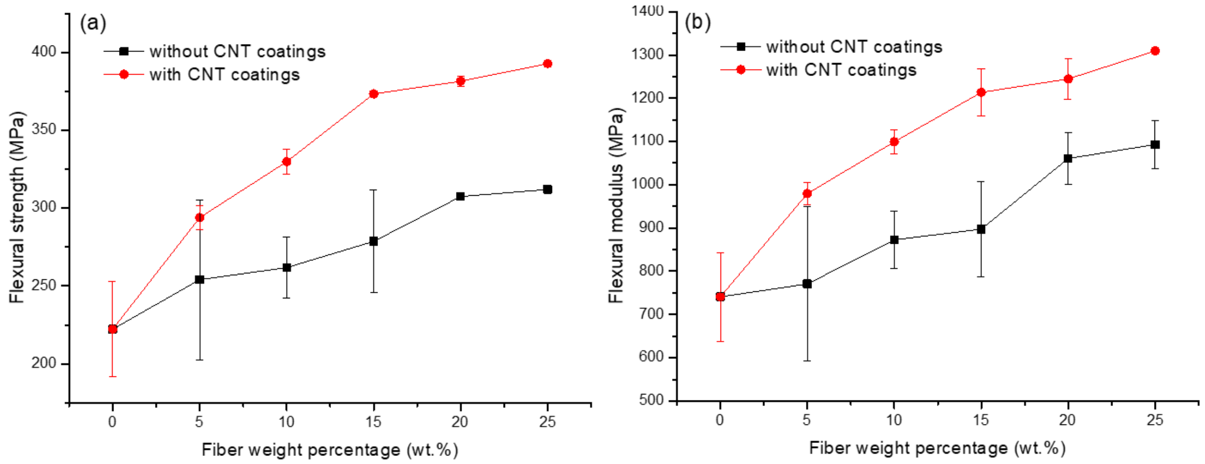

Figure 4.4 Flexural properties of CF/HDPE composites without and with CNT coatings: (a) flexural strength and (b) flexural modulus.

The Vickers hardness of hierarchical CF/HDPE composites with CNT spray coatings was compared with those without coatings as a function of varying fiber contents. Higher hardness is favourable in engineering application for its stronger resistance to penetration, wear, cutting and scratching[263]. As shown in **Figure 4.5**, with the increase of CF contents, the hardness of CF/HDPE composites exhibited an upward tendency. This can be ascribed to the increased number of linkage points with higher fiber content in the skeletal composite structure, which plays a crucial role in the improved resistance to external pressure by hindering the movement of matrix polymer chain [264]. Meanwhile, for the same content of CFs, PE reinforced by CNT-coated CFs had higher hardness values than the counterparts without CNT coatings. Compared to the composites without CNT coatings, the hardness of hierarchical CNT-CF/HDPE composites was increased by 22.67% when the CF content was 25%, which indicates that the interfacial bonding between fiber and matrix was largely enhanced. In generally, the synergistic mechanism originated from higher CF content and stronger interfacial adhesion modified by CNT coatings endowed the hierarchical composites with superior hardness.

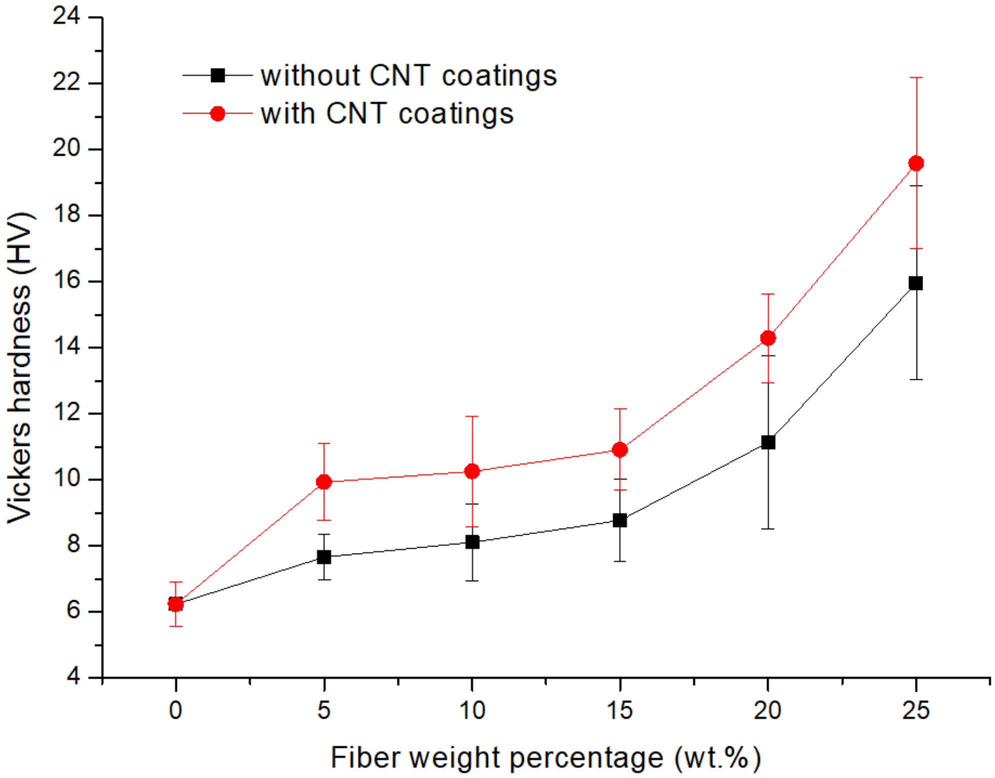

Figure 4.5 Hardness of CF/HDPE composites with and without CNT coatings.

4.3.2 Thermal properties

The crystallization and melting patterns of pristine HDPE, CF/HDPE composites and CNT-coated CF-HDPE composites obtained from DSC measurements were studied since fillers in a crystalline polymer matrix generally have the potential to alter thermal behaviors of the matrix. Based on DSC thermograms of the melting and cooling processes from different specimens (**Figure 4.6**), their melting temperature (T_m), cold crystallization temperature (T_c), melting enthalpy (ΔH_m) and degree of crystallization (X_c) were measured and listed in **Table 4.1**. It can be clearly viewed that T_m did not change significantly after the addition of CF, whether it was for CNT-coated or not. However, T_c in most cases for CF reinforced composites was lower than for pristine HDPE (112.21°C), except those composites with high CF content, such as T_c

for 25% CF/HDPE composite (112.58°C) and T_c for 20% CNT-CF/HDPE composite (113.10°C) and 25% CNT-CF/HDPE (112.89°C) composite. This can be elaborated by the interaction mechanism existing among CNT, CF and HDPE matrix.

Table 4.1 DSC data of the pristine HDPE, CF/HDPE composites and CNT-CF/HDPE composites.

Samples	**T_m (°C)**	**T_c (°C)**	**ΔH_m (J/g)**	**X_c**
HDPE	140.55	112.21	207.97	70.83%
5% CF/HDPE	139.98	109.31	196.24	70.35%
10% CF/HDPE	140.67	110.35	186.69	70.27%
15% CF/HDPE	140.62	110.17	172.55	69.14%
20% CF/HDPE	141.57	109.49	159.18	67.77%
25% CF/HDPE	139.55	112.58	145.91	66.26%
5% CNT-CF/HDPE	139.09	110.30	185.07	66.35%
10% CNT-CF/HDPE	140.18	110.58	179.32	67.86%
15% CNT-CF/HDPE	140.62	110.74	170.75	68.42%
20% CNT-CF/HDPE	140.78	113.10	164.65	70.10%
25% CNT-CF/HDPE	139.93	112.89	148.49	67.43%

With the introduction of long chopped CF, the friction between fibers and polymer chains can obstruct the mobility of the macromolecular chain and thus hinder the formation of highly ordered alignment of the crystal lattice [265]. It has been reflected by the decrease of T_c and X_c for both uncoated and CNT-coated CF/HDPE composites compared to that for the pure

HDPE. Simultaneously, for the CNT-coated hierarchical composites, the CNTs were mainly coated on the surface of CF and rarely dispersed in the matrix by the shear force of extrusion, which acted as the effective heterogeneous nuclei, to a certain extent, facilitating the crystal growth during the crystallization process [266]. It is well explained why X_c increased to the highest value of 70.10% for the 20% CNT-CF/HDPE composite, although a slight decrease was seen for the 25% counterparts due to the inhibiting effect from CF. It should be noted, however, that the existence of CNT acted not only as heterogeneous nuclei to promote the crystal growth, but also as restriction sites to hinder the regular arrangement of polymer chains [267]. In short, the intricate mutual interplay existing in CNT, CF and HDPE contributes to the complicated thermal hehaviors for the hierarchical CNT-CF/HDPE composites.

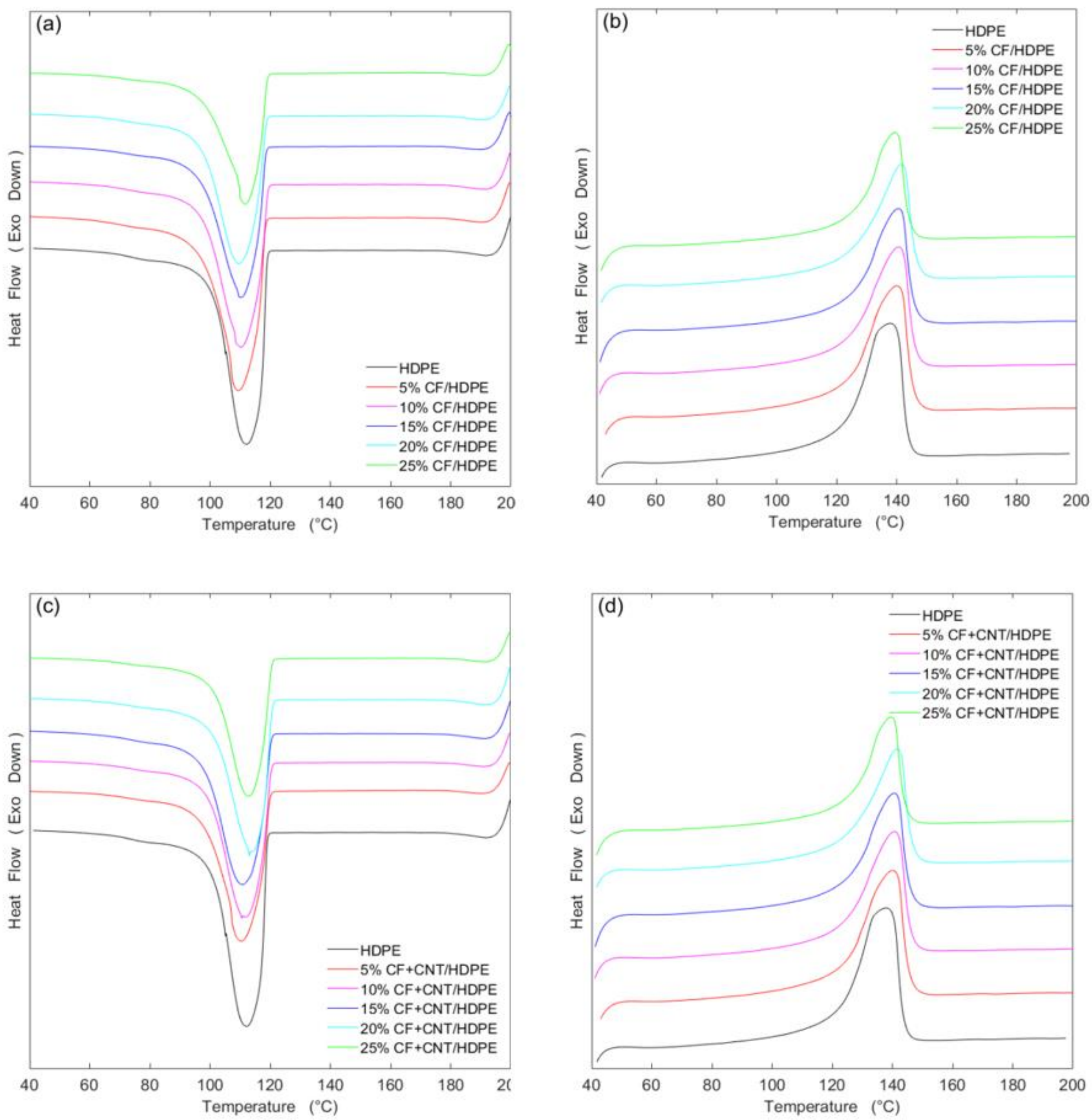

Figure 4.6 DSC curves of (a) cooling process of CF/HDPE composites, (b) melting process of CF/HDPE composites, (c) cooling process of CNT-CF/HDPE composites and (d) melting process of CNT-CF/HDPE composites.

4.3.3 Morphological properties

The surface morphology of CF after the spray coating of CNTs was first investigated via SEM analysis. As seen in **Figure 4.7a** and **b**, the surface morphologies of raw CFs were extremely smooth while the CNTs exhibited long and curvy structure with fiber-like shape. After the deposition of CNTs on the fiber surface by spray coating, the morphology of CFs with surface modification had been remarkably altered, which was shown in **Figure 4.7c** and **d** with different magnifications. The initial clean and smooth surface of CFs was wrapped by randomly oriented CNTs, resulting in a much rougher structure with many protrusions. Li et al. found similar results in the surface modification of CFs, where the commercially carbonxylic- and hydroxyl-functionalized CNTs were selected to coat the sized CFs by employing an aqueous suspension deposition method [243].

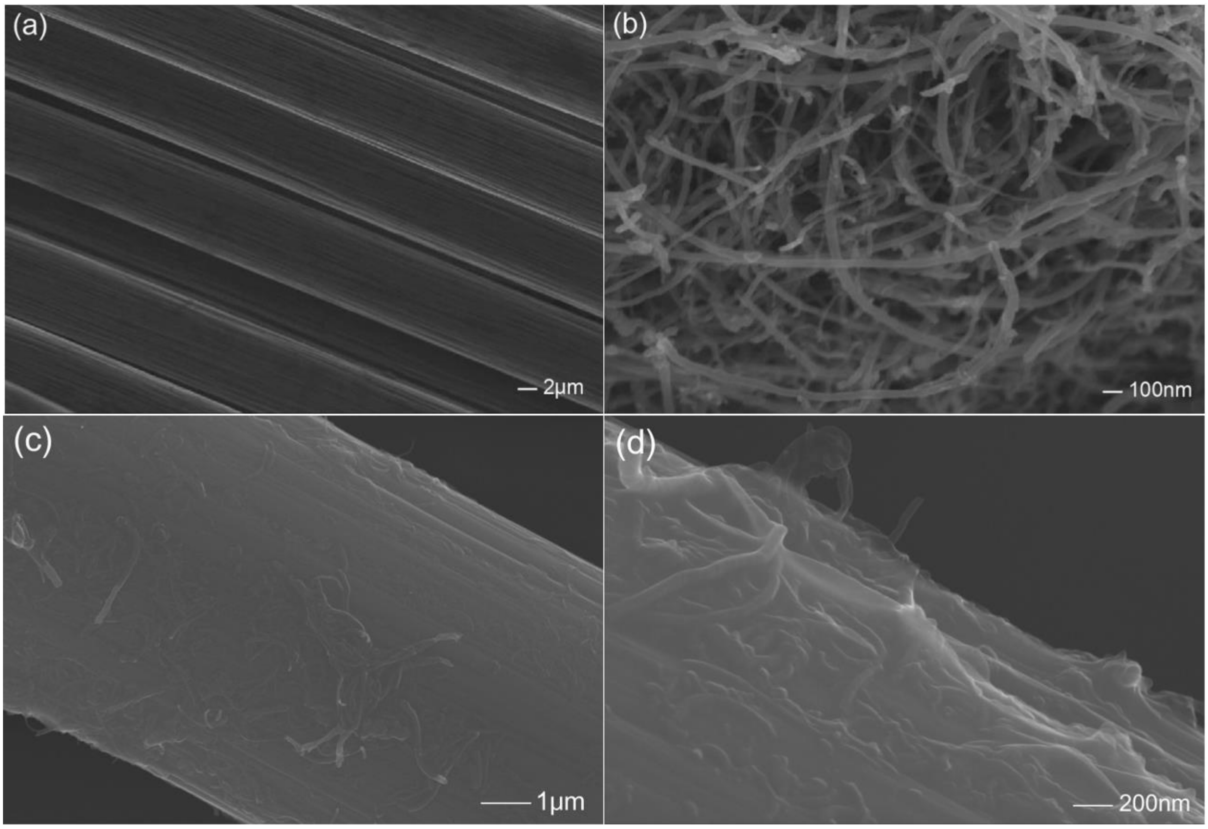

Figure 4.7 SEM images of (a) raw CFs, (b) CNTs, (c) and (d) CFs with CNT spray coatings.

The fractural morphologies of CF/HDPE composites with and without CNT coatings were next examined to qualitatively analyze the interfacial bonding between fibers and matrix. The pull-out CFs from the fractural surface of fiber reinforced composites can be clearly seen from all SEM images in **Figure 4.8**. According to **Figure 4.8a** and **b**, the morphological surfaces of CFs were very clean and smooth, which not only led to the big gaps between fibers and matrix, but formed numerous deep cavities from the direct pull-out of CFs. It obviously indicated the poor interfacial adhesion existing in the uncoated CF/HDPE composites. On the contrary, the gaps between CFs and HDPE matrix became much smaller for the CNT-coated CF/HDPE composites than those of the uncoated counterparts, as were shown in **Figure 4.8c** and **d**. From the SEM image in **Figure 4.8d**, it can also be seen that the HDPE matrix was attached onto the surface of CFs. These can be attributed to the improved interfacial bonding between fiber and matrix compared to the untreated composites. By virtue of the CNT spray coating onto CFs, the increased roughness on fiber surface facilitated the local interlocking between CFs and HDPE matrix, strengthening their mutual adhesion. The enhanced frictional force at the interphase based on the increased roughness also benefited the stress transfer from the matrix to high mechanically performed fibers, which improved the entire strength of CF/HDPE composites.

In addition, it is worth noting from **Figure 4.8** that with the introduction of CNTs into CF/HDPE composites, the fractural morphology at the matrix has been changed, from the relatively smooth surfaces converting to highly rough structures, which indicated the toughening effect of the matrix given by CNTs. The obvious increase of toughness in the HDPE matrix can be realized with very low content of the introduced CNTs. During the twin-screw extrusion of hierarchical CNT-CF/HDPE composites, some CNTs were peeled off from the fiber surface and dispersed into the matrix, so that the toughening of polymer matrix was generated [268]. This result further promoted the release of stress concentrations and hampered the crack propagation, which was beneficial to form a stronger interphase. All of these SEM observations in the fractural morphologies of composites well corresponded to the result from the mechanical test mentioned in section 4.3.1.

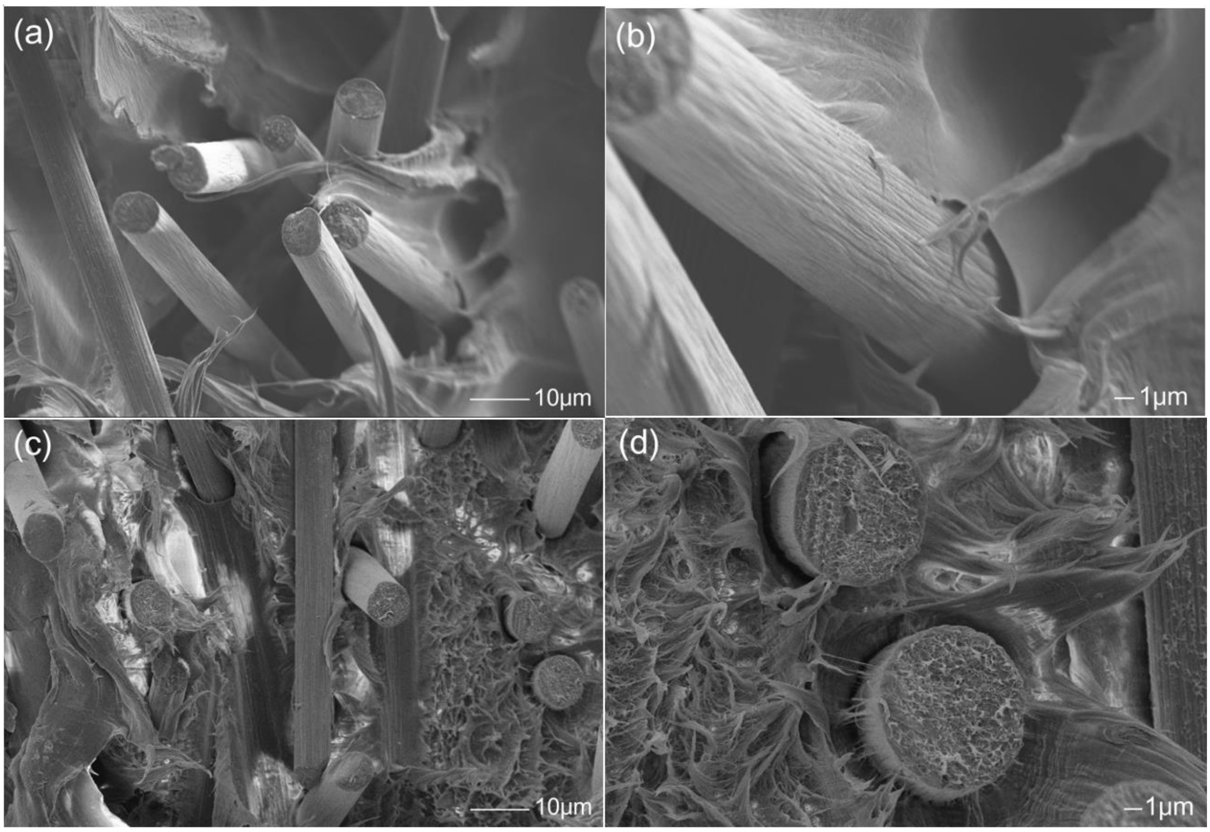

Figure 4.8 Fractural morphologies of (a) and (b) CF/HDPE composites without CNT coatings, (c) and (d) CF/HDPE composites with CNT coatings.

4.4 Conclusions

As a simple and economical coating method, spray coating of CNTs onto the surface of chopped CF was first reported for modifying the morphological properties of CFs. Then, the hierarchical CNT-coated CF reinforced composites were fabricated by employing the extrusion compounding and injection molding techniques. In order to study the mechanical properties of CF/HDPE composites after CNT coatings, tensile, flexural and hardness tests were conducted. The results showed that when the CF content reached 25%, the tensile strength and flexural strength of CF/HDPE were improved by 70.62% and 40.38% compared to the pure HDPE. After the spray coating of CNTs, the tensile strength and flexural strength were further enhanced, as well as the modulus values. Besides, the Vickers hardness of both uncoated and CNT coated composites showed an increasing trend relative to the HDPE matrix, while the coated composites have higher values than uncoated counterparts. With the CF content rose up to 25%, the hardness of the CNT-CF/HDPE composite was increased by 22.67% compared to the uncoated composite. It can be attributed to the high stiffness and strength of CF and the improved interfacial bonding between CF and the matrix after CNT coating, which was clearly observed from SEM images. The DSC analysis also illustrated the effect of CF and CNT on the crystallization of the HDPE matrix, both of which acted as heterogeneous nuclei and restriction sites to regulate the crystal growth of matrix in the fabricated composites. In conclusion, the spray coating of CNTs onto CF was demonstrated to be a promising surface modification method to fabricate the CNT-CF/HDPE composites with the improved interfacial properties to enhance the mechanical performance of the hierarchical composites.

CHAPTER 5 THE FABRICATION OF LONG CARBON FIBER REINFORCED POLYLACTIC ACID COMPOSITES VIA FUSED DEPOSITION MODELLING: EXPERIMENTAL ANALYSIS AND MACHINE LEARNING

5.1 Introduction

Additive manufacturing (AM), also known as 3D printing or rapid prototyping enables and facilitates the fabrication of complex objects by adding materials layer-by-layer from a computer-aided design file [182]. First introduced by Charles Hull, this technique has attracted significant research which results in the establishment of ISO/ASTM standards for various AM processes: binder jetting, material jetting, material extrusion, directed energy deposition, sheet lamination, powder bed fusion and vat photopolymerization [42]. This can be attributed to its numerous technical merits. Compared to conventional subtractive manufacturing methods, AM can take full advantage of raw materials to create the final parts with minimum waste after manufacturing [35]. The designed products with complicated internal geometry can also be fabricated directly from 3D models without the need of other tools (e.g. jigs and fixtures). As to the product design innovation, AM to a certain extent avoids the additional consideration of manufacturing and assembly (DFM/DFA) principles [269]. Furthermore, the consumption of natural resources and energy is minimalized in the AM operation by virtue of its lean production with less waste and post treatments, contributing to the automated manufacturing of environmental friendly products [270].

Currently, raw materials adopted in the AM industry are primarily polymers in two types owing to their ease of processing and availability: thermosetting polymers (e.g. expoy) and thermoplastics (e.g. acrylonitrile butadiene styrene (ABS), polyethylene (PE) and polylactic acid (PLA)) [10, 22, 271]. The former can be cured into solid parts from a liquid state with low viscosity via UV-assisted polymerization process while the later mainly involves in the repeated heating and cooling of solid polymers so that desirable geometries can be achieved during 3D printing [272]. Based on the specific selection of these polymeric materials, AM technique has been widely employed in various industries, such as automotive field for light weight structures, construction field for high load-bearing supports, education field for prototype demonstration and biomedical field for tissue and organ replacement [273-275]. Nevertheless, the inherent drawback of low strength and stiffness existing in polymers leads to the poor mechanical properties of products fabricated by AM, even though a series of processing parameters (e.g. layer thickness, build orientation, feed rate and etc.) have been studied with the result of limited improvements [276]. It largely restricts the 3D printing of polymers in high performance engineering applications. Therefore, the organic integration of composite materials with AM technique via introducing various reinforcers for better mechanical properties has spurred great interests in recent years [177, 277].

As man-made materials, composites are normally composed of two or more constituents with distinctive mechanical, physical or chemical properties [232, 278-280]. By orchestrating each constituent, composite materials can be endowed with superior performance with respect to the individual components [281, 282]. Up to now, numerous additives (e.g. carbon nanotubes, carbon black, metallic powders and short/long fibers) have been incorporated into the conventional AM of polymers so as to achieve the 3D printed composites with desirable features [283-285]. The most common additives are high-performance fibrous reinforcers due to their higher strength and stiffness in fiber form than in bulk form [286]. Among all of AM technologies, fused deposition modelling (FDM) is the most widely applied technique to fabricate fiber reinforced polymer composites. Its easy operation, low energy input and cheap manufacturing cost can credit to its relatively simple mechanical principles [287, 288]. In FDM, the thermoplastic-based filament is pushed forward into a heated nozzle via a pinch roller and melted into a semi-liquid state above the glass transition temperature. Through the action of three-dimensional movable nozzle, the molten filament is then deposited onto the printing bed and fused together into the designed part [133].

Although researches in the past five years enabled the fabrication of continuous fiber reinforced composites via AM technique, the necessity for the modification of common 3D printers with complex processing makes it currently at the infant stage [36, 211, 289]. The application of discontinuous fibers is still the mainstream for the FDM fabrication of fiber reinforced composites. For instance, by incorporating short carbon fiber (CF) with varying weight percentage into the ABS matrix, Ning et al. found that the tensile and flexural properties of these CF reinforced composites were better than the pure plastic counterpart with the best result performed at 5 wt% CF addition. Meanwhile, the 3D printed ABS composites with longer CF (150 μm) had higher tensile strength and Young's modulus than that with 100 μm CF [184]. Blok et al. conducted the related experiments to compare the short CF (~0.1 mm) reinforced Nylon composites with the continuous fiber printed parts. Although continuous CF/Nylon composites exhibited better tensile strength and stiffness than short fiber reinforced parts, the continuous CF has its placement difficulty while being deposited at sharp angles and through small steering radii [189]. Papon and Haque investigated the fracture properties of FDM-based PLA composites with milled CF (100 μm) as the reinforcement. The results showed that compared to neat PLA, a significant enhancement in fracture toughness and facture energy was achieved for either $0^{\circ}/90^{\circ}$ or $45^{\circ}/-45^{\circ}$ bead-oriented composites [183]. Ferreira et al. also observed enhanced tensile modulus and shear modulus of the neat PLA polymer with 15 wt% CF content both in the printing and transverse direction while the short length of CF (60 μm) was deemed to constrain the further mechanical improvement of composites[186].

In general, the fiber with a critical length is preferred so that the applied stress can be effectively transferred from the matrix to the reinforced fiber based on the shear transfer mechanism [9]. Short fibers not only hamper the stress transferring, but incur more stress concentrations with increasing fiber ends at the same fiber content [187]. To the best of our knowledge, no related paper has been published regarding the introduction of chopped long CF (~4.6 mm) as the reinforcement into the fabrication of 3D printed PLA composites. By varying the addition of these long CF, the CF/PLA composites were prepared via FDM method and the effect of CF contents on mechanical, thermal and morphological properties of these composites were comprehensively assessed (**Figure 5.1**). Furthermore, machine learning with Gaussian Process modelling was also first introduced into the research of 3D printed composite materials to compare with our experimental analysis and make useful predictions for the corresponding mechanical properties.

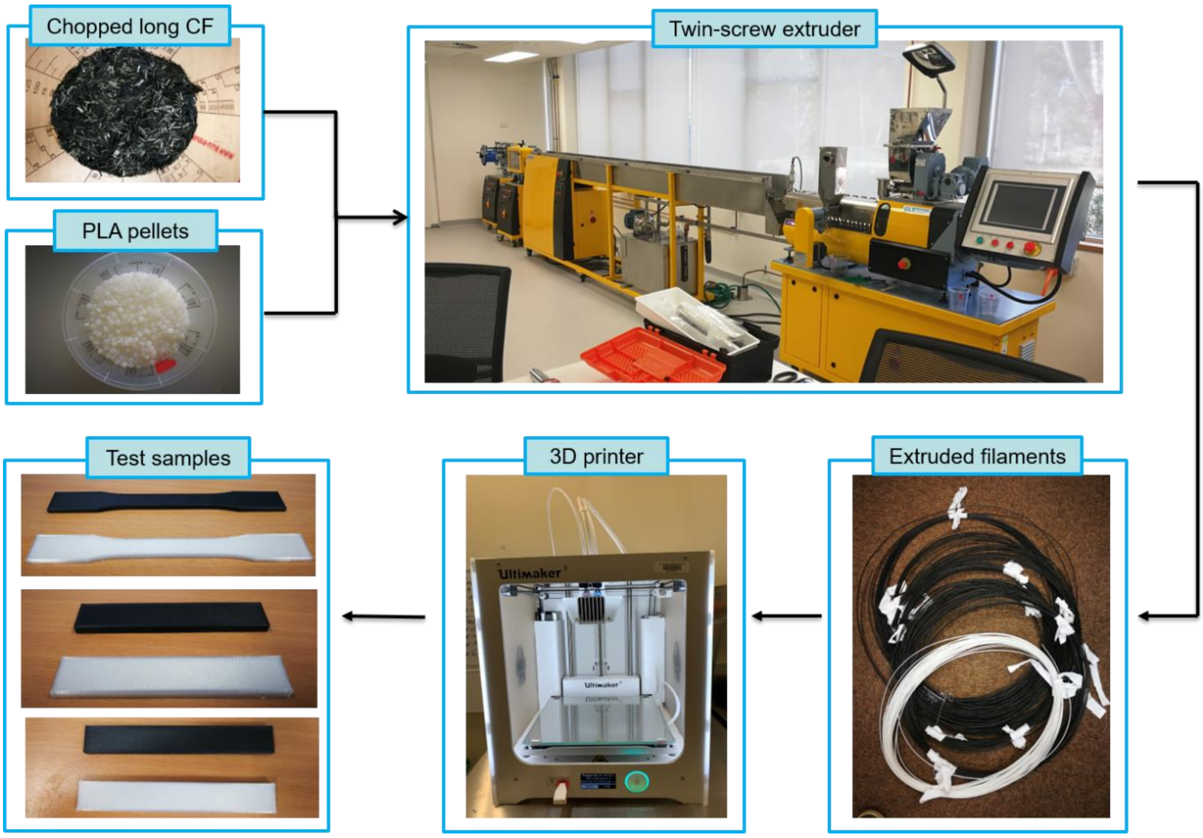

Figure 5.1 Schematic for the fabrication of 3D printed CF/PLA composites with varying CF contents.

5.2 Methodology

5.2.1 Materials

The natural PLA pellets were purchased from Aurarum Pty Ltd (Keysborough, Australia) with the melting temperature ranging from 185 ºC to 220 ºC. The polyacrylonitrile-derived CF in chopped form was supplied by ACP Composites (Livermore, USA) as the reinforcement for 3D printed composites. According to the product specification from our supplier, the average length of the chopped CF is 4.6 mm and its common diameter is 7 µm.

5.2.2 Twin-screw extrusion

The CF/PLA composite filaments with varying CF contents (i.e. 2.5 wt%, 5 wt%, 7.5 wt%, 10 wt% and 15 wt%) were prepared by employing an industrialized co-rotating twin-screw extrusion system (LTE16-44, Labtech Engineering, Thailand). The fabrication of these filaments at higher CF contents (>15 wt%) was difficult due to the failure of uniform extrusion. It consists of four units for the manufacturing of 3D printing filaments: the twin-screw extruder unit to melt, mix and extrude the continuous filament; the water bath unit to cool down and solidify the extrudate; the caterpillar hall-off unit to convey the extruded filament; and the wind-up unit to collect the filament onto a spool. Equipped with 11 temperature-control zones, the extruder has two screws with the diameter of 16 mm and length/diameter ratio of 44 mm. As is shown in **Table 5.1**, all processing parameters involved in the fabrication of CF/PLA composite filaments were optimized so as to achieve the uniform circular shape with the average diameter of 2.85 mm for 3D printing. The neat PLA filament was also prepared under the same conditions as the control.

Table 5.1 Processing parameters employed in the fabrication of 3D printing filaments via the industrialized twin-screw extrusion system.

Heating zones	Z1	Z2	Z3	Z4	Z5	Z6	Z7	Z8	Z9	Z10	Die
Temperature (ºC)	200	200	200	180	180	180	180	180	180	180	180
Screw speed (rpm)						25					
Water bath temperature (ºC)						20					
Hall-off speed (m/min)						3.2					
Wind-up tension (Nm)						1.0					

Since the chopped CF used here had relatively long lengh (~4.6 mm), the mixture of fibers and PLA pellets were easy to block the barrel throat during the addition of materials into the feed hopper. These light and long CFs could accumulate together and form a net-like structrure above the rotating screws, preventing the continuous feed flow of this fiber/pellet mixture. In order to solve this issue, the constant mixing and pushing strategy via a pushing rod was employed so as to avoid the forming of this net-like structure and ensure the stable feeding of this blended feedstock. Consequently, homogeneous CF/PLA composite filaments can be produced for the following 3D printing process.

5.2.3 3D printing

All neat PLA and CF/PLA composite samples for the following characterizations were printed by feeding extruded filaments into a commercial FDM printer (Ultimaker 3, Ultimaker, Netherlands) with the nozzle diameter of 0.4 mm. These samples were designed as STL files via SolidWorks and converted into G-code files which can be recognized by the printer. It should be mentioned that nozzle size, speed and temperature can affect the heat input, fusion, porosity formation and fiber alignment, consequently leading to the variation of microstructure and mechanical properties of printed specimen. All the processing parameters were regulated by using the Cura software. During printing, the nozzle temperature was set at 200 ºC while the build plate temperature was 60 ºC. The printing speed was controlled at 70 mm/s with the thickness of each layer maintained at 0.1 mm. The raster angle for deposition directions of different layers were +45º and -45º. The infill percentage was set at 100 %. In order to prevent warping and enhance bed adhesion during printing, the raft that can be easily peeled off was introduced at the bottom of printed samples.

5.2.4 Sample characterization

The tensile test and flexural test for PLA and CF/PLA composites were conducted by employing a universal testing machine (model 4505, Inston, United States) with the load cell capacity of 5 kN. Type-1 dog bone geometry in ASTM D638 was used for the FDM fabricated samples so as to measure the tensile strength, modulus and elongation at break for the tensile test while rectangular geometry with proper dimensions in accordance with ASTM D790 was selected for the measurement of flexural strength and modulus in three-point bending test (**Figure 5.2**). Five parallel samples for each composition were tested at a displacement rate of

5 mm/min. The hardness test was performed under ambient conditions by using a Rockwell hardness tester machine (model DXT, Matsuzawa, Japan) with the load of 10 kg applied for 15 s. Data was collected and averaged from the measurement of ten replicates for each sample.

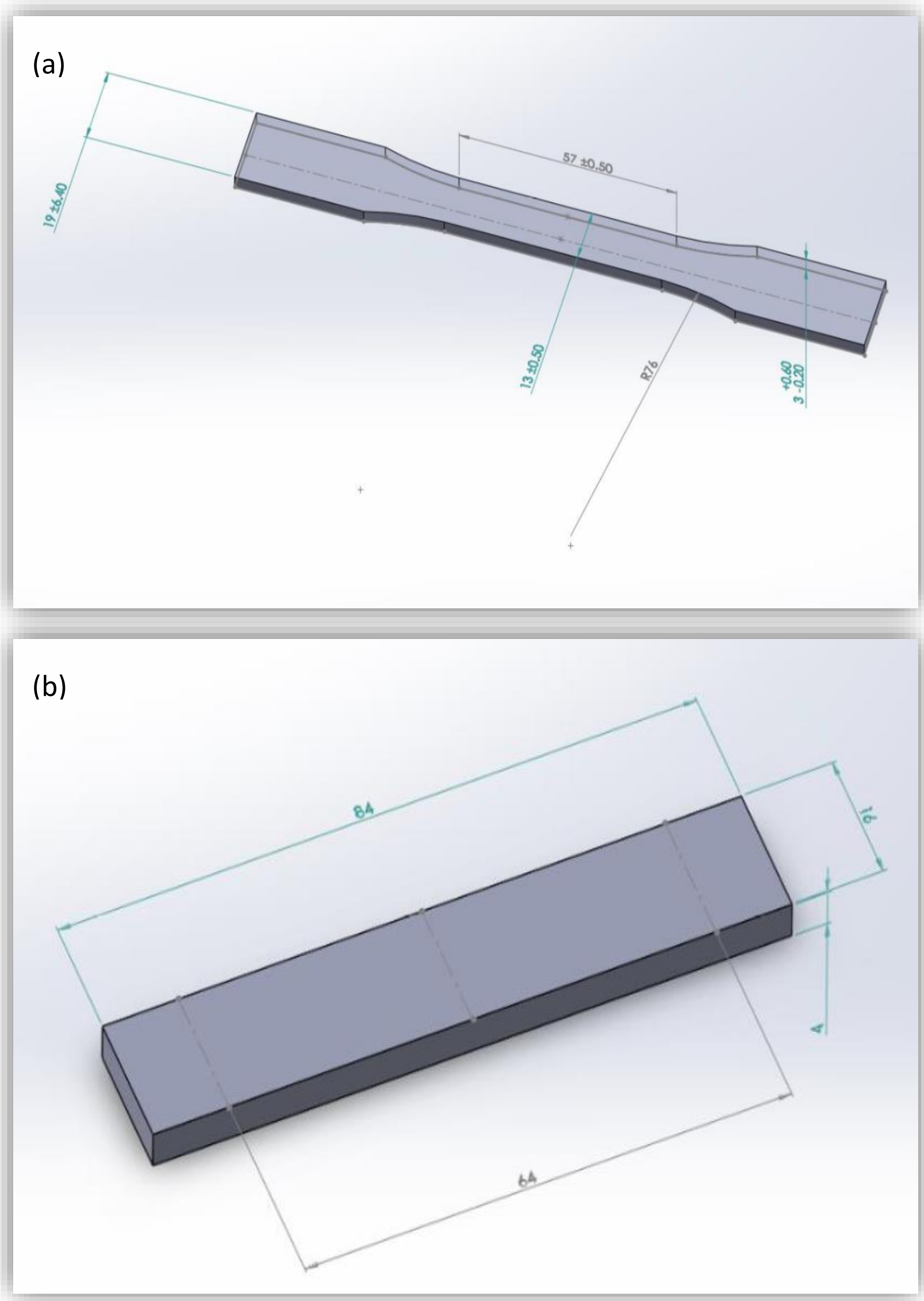

Figure 5.2 Sample dimensions for mechanical characterization: (a) ASTM D638 type 1 sample dimension for tensile test and (b) ASTM D790 sample dimension for flexural test.

The thermal conductivities of PLA and CF/PLA composites were measured in accordance with ASTM E1225 and ASTM D5470. Via connecting the resistor (WH50, TT Electronics, United Kindom) assembled on this apparatus to a power source with 100W power input, heat was created and delivered from the top aluminium block to the bottom aluminium block through the sample which was clamped between these two blocks. The temperature difference was then recorded with thermocouples attached to each side of the aluminium block. The schematic of the experimental setup was shown in **Figure 5.3**. To minimize the effect of heat loss, styrofoam boards were employed to house the experimental apparatus so that an insulated environment was achieved. The sample size was 48 mm × 33 mm × 4 mm in rectangular shape. The thermal conductivity k of a target sample was calculated via the following equation (1) from one-dimensional model of Fourier's law:

$$Q = kA\frac{\Delta T}{t} \tag{1}$$

Where Q is the unidirectional heat flow, k is the thermal conductivity, A is the area of the sample, ΔT is the difference in temperature and t is the thickness of the target sample.

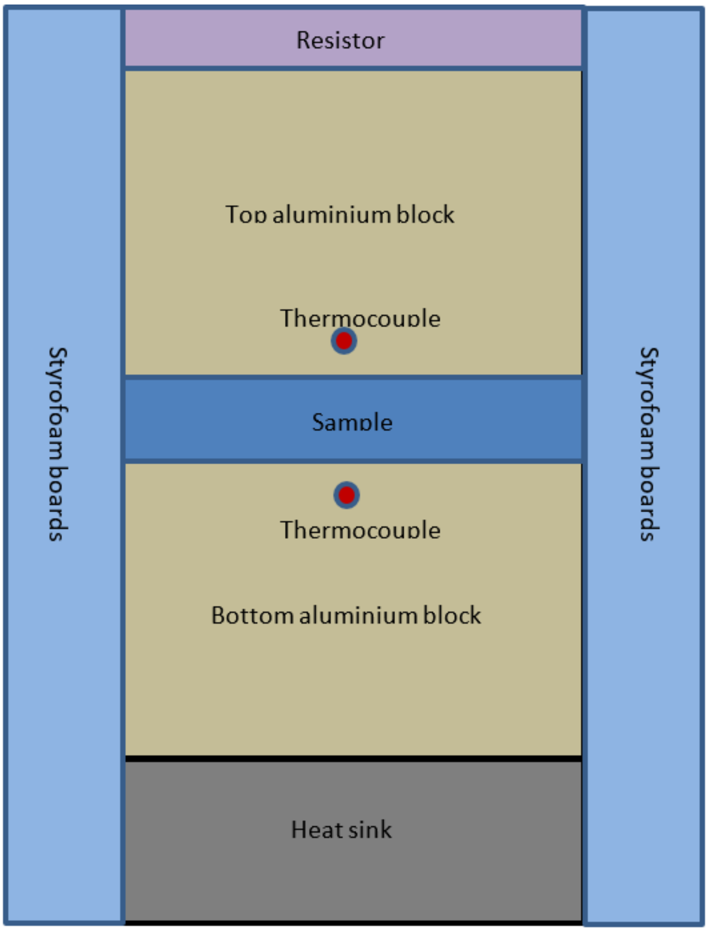

Figure 5.3 The schematic of the experimental setup for thermal conductivity test.

The fracture surfaces of neat PLA and CF/PLA composites after tensile test were observed by employing a scanning electron microscope (GeminiSEM 500, ZEISS, Germany) with the acceleration voltage of 15 kV. In order to prevent the charging effect on the surface, all samples were sputter coated with a thin layer of gold before imaging to enhance the electric conductivity and SEM resolution.

5.2.5 Machine learning

As one of machine learning (ML) techniques, the Gaussian Process was employed for the prediction regarding the mechanical properties of CF/PLA composites with respect to CF contents. It is a stochastic method that the finite number of random variables derived from this process follow a joint Gaussian distribution. Meanwhile, Gaussian Process Regression is based on Bayles's Rule given:

$$posterior = \frac{Likelihood \times prior}{Normalisation} \tag{2}$$

where likelihood and prior function are both assumed to be Gaussian distributed.

In terms of 3D printed CF/PLA composites, input X could be referred as CF contents whereas output Y could be defined as their corresponding physical properties, where $x_i \in R$ and $y_i \in R^6$. Thus, the experimental data could be paired as $\boldsymbol{S}_d = (\boldsymbol{X}_d, \boldsymbol{Y}_d) = (x_{d,1}, y_{d,1}) \ldots (x_{d,N_d}, y_{d,N_d})$ for each component $\boldsymbol{f}_d$ with d, n = 1, ….D, where D and N are both equal to 6 in this case. Therefore, Gaussian prior function could be written as:

$$\boldsymbol{f}(\boldsymbol{X}) \sim \boldsymbol{N}(\boldsymbol{m}(\boldsymbol{X}), \boldsymbol{K}(\boldsymbol{X}, \boldsymbol{X})) \tag{3}$$

where $\boldsymbol{m}(\boldsymbol{X}) \in R^D$ is mean vector of each output which assumed to be zero vector. While, **K (X, X)** is a covariance matrix which is defined to be positive-semi definite matrix. The kernel function is defined as the following format:

$$\mathbf{K}\,(\mathbf{X},\mathbf{X}) = \begin{bmatrix} (\mathbf{K}(\mathbf{X_1},\mathbf{X_1}))_{\mathbf{1,1}} & \cdots & (\mathbf{K}(\mathbf{X_1},\mathbf{X_1}))_{\mathbf{1},\boldsymbol{D}} \\ (\mathbf{K}(\mathbf{X_2},\mathbf{X_1}))_{\mathbf{2,1}} & \cdots & (\mathbf{K}(\mathbf{X_2},\mathbf{X}_{\boldsymbol{D}}))_{\mathbf{2},\boldsymbol{D}} \\ \vdots & \cdots & \vdots \\ (\mathbf{K}(\mathbf{X}_{\boldsymbol{D}},\mathbf{X_1}))_{\boldsymbol{D},\mathbf{1}} & \cdots & (\mathbf{K}(\mathbf{X}_{\boldsymbol{D}},\mathbf{X}_{\boldsymbol{D}}))_{\boldsymbol{D},\boldsymbol{D}} \end{bmatrix} \tag{4}$$

where Xi represents the inputs corresponding to the i-th output.

Three kernel functions including radius bias and Mater32 are chosen to construct the covariance matrix as

$$\mathbf{K} = B \otimes (\mathbf{K}_1 + \mathbf{K}_2) \tag{5}$$

where B is regarded as the coregionalization matrix.

The likelihood function for the output is defined as:

$$p(\boldsymbol{y}|\boldsymbol{f}, x, \Sigma) = N(\boldsymbol{f}(\mathbf{x}), \Sigma). \tag{6}$$

The predictive distribution for a new CF content therefore could be derived as:

$$p(\boldsymbol{f}(\boldsymbol{x}_*)|, \boldsymbol{S}, \boldsymbol{f}, \boldsymbol{x}_*, \varphi) = N(\boldsymbol{f}_*(\boldsymbol{x}_*), \mathbf{K}_*(\boldsymbol{x}_*, \boldsymbol{x}_*)) \tag{7}$$

with

$$\boldsymbol{f}_*(\boldsymbol{x}_*) = \mathbf{K}_{\boldsymbol{x}*}^{\boldsymbol{T}}(\mathbf{K}(\mathbf{X}, \mathbf{X}) + \boldsymbol{\Sigma})^{-\mathbf{1}}\bar{y}, \tag{8}$$

$$\mathbf{K}_*(\mathbf{x}_*, \mathbf{x}_*) = \mathbf{K}(\mathbf{x}_*, \mathbf{x}_*) - \mathbf{K}(\mathbf{K}(\mathbf{x}, \mathbf{x}) + \boldsymbol{\Sigma})^{-\mathbf{1}}\mathbf{K}_{\boldsymbol{x}*}^{\boldsymbol{T}} \tag{9}$$

where $\boldsymbol{\Sigma} = \Sigma \otimes I_N$**,** and φ denotes a possible set of hyperparameters of the covariance function $\mathbf{K}(\mathbf{x}, \mathbf{x}')$ used to compute $\mathbf{K}(\mathbf{X}, \mathbf{X})$ and variances of noise.

The detailed programming code involved in the ML process can be found in the Appendix of this thesis.

5.3 Results and discussion

5.3.1 Mechanical properties

The results of all mechanical properties including tensile, flexural and hardness tests for neat PLA and PLA composites with varying CF contents have been summarized in **Table 5.2**.

Table 5.2 Mechanical properties of neat PLA and PLA composites with varying CF contents

Samples	Tensile strength (MPa)	Tensile modulus (GPa)	Elongation at break (mm)	Flexural strength (Mpa)	Flexural modulus (Gpa)	Hardness (HRR)
Neat PLA	23.66±1.11	1.40±0.04	2.82±0.22	40.28±2.75	1.02±0.22	35.37±2.13
2.5 wt% CF/PLA	31.66±2.67	1.67±0.09	3.16±0.23	51.09±5.41	1.75±0.40	49.93±4.55
5 wt% CF/PLA	44.75±2.40	2.31±0.16	3.23±0.29	56.19±4.93	1.81±0.23	82.03±6.31
7.5 wt% CF/PLA	39.86±2.01	2.39±0.12	2.77±0.15	43.39±3.02	1.99±0.25	79.33±8.34
10 wt% CF/PLA	24.65±2.68	2.06±0.18	1.96±0.06	32.18±4.48	1.19±0.17	74.44±9.52
15 wt% CF/PLA	26.88±1.39	2.12±0.07	1.68±0.05	57.60±3.81	2.91±0.26	77.78±10.11

5.3.1.1 Tensile properties

The results of tensile tests for 3D printed neat PLA and CF/PLA composites with varying CF contents were given in **Figure 5.4**. Compared to the pure PLA polymer, the tensile strength greatly increased by 89.14% from 22.66 MPa to 44.75 MPa with the CF contents rising from 0 wt% to 5 wt% (**Figure 5.4a**). The result can credit to the remarkable strength and modulus of CF as the mechanical performance of composites normally can be enhanced via the incorporation of superior reinforcement with higher stiffness than the matrix [261]. Another important reason underlying this phenomenon might be the application of long reinforced CF (~4.6 mm) in the fabrication of 3D printed composites, exceeding the normal length of reinforced fibers introduced into thermoplastic composites. Nevertheless, a downward tendency of tensile strength to 24.65 MPa was observed with the increase of CF contents from 5 wt% to 10 wt%, especially the occurrence of a plunge for tensile strength between 7.5 wt% and 10 wt% CF/PLA composites. This may be ascribed to the more porosity caused by the increased voids around the poor fibers-matrix interface with higher fiber contents, impairing the mechanical performance for the printed composites. After that, the 15 wt% CF/PLA composite exhibited a larger tensile strength than that from the 10 wt% counterpart due to the mechanical improvement from higher CF content.

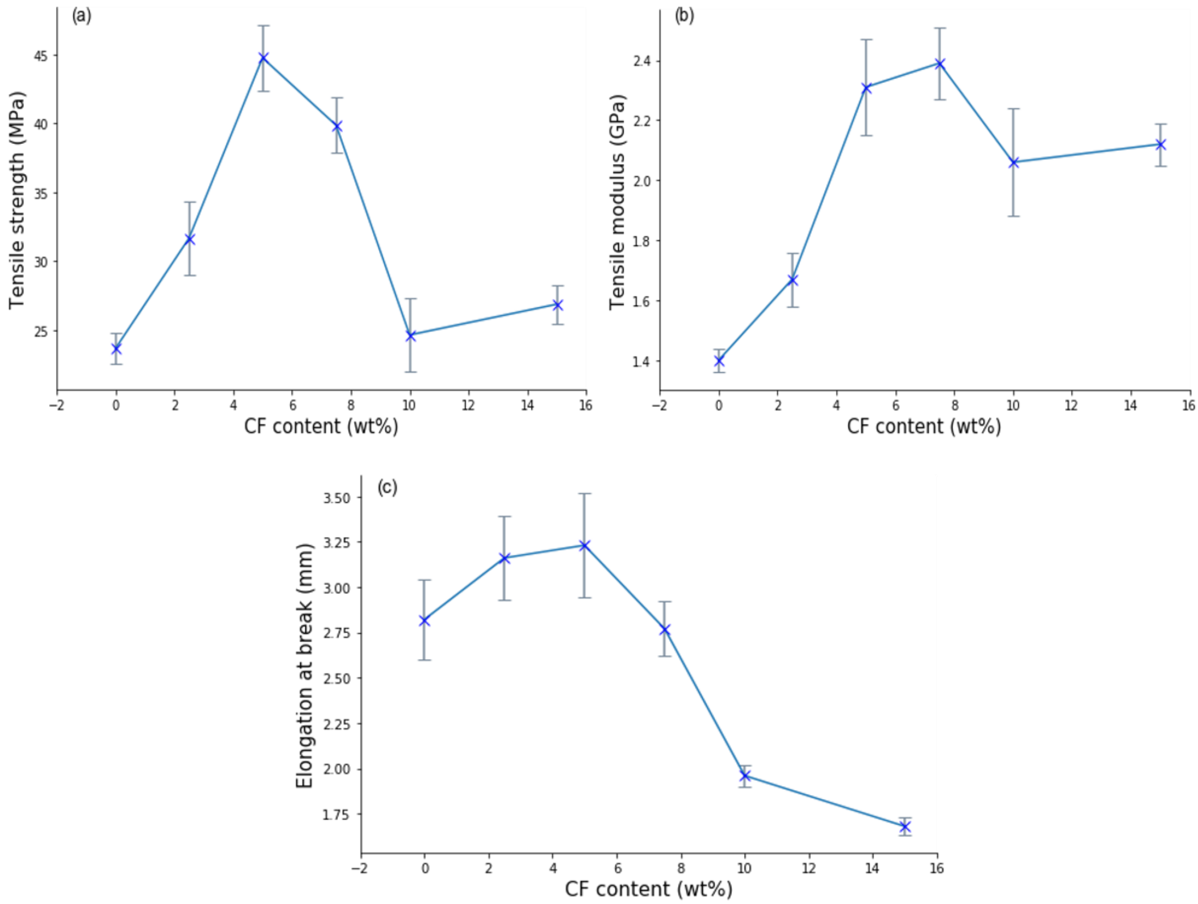

Figure 5.4 Tensile properties of 3D printed CF/PLA composites with varying CF contents: (a) tensile strength, (b) tensile modulus and (c) elongation at break.

Similar to the influence of CF contents on strength results, the tensile modulus of 3D printed composites showed an upward trend with the increase of CF contents from 0 wt% to 7.5 wt% and then decreased when the level of chopped fibers reached at 10 wt% (**Figure 5.4b**). Continuing the addition of CF contents from 10 wt % to 15 wt% contributed to the increase of tensile modulus again. The largest tensile modulus possessed by 7.5 wt% CF/PLA composite was 2.39 GPa while the lowest was 1.40 GPa at the neat PLA sample, demonstrating a 70.71% enhancement in modulus. With the incorporation of CF contents, the elongation at break representing the maximum displacement gradually increased to the largest at 5 wt% CF/PLA composite and then decreased to the lowest at the most CF content (15 wt%), as shown in **Figure 5.4c**. It might be explained by that the large voids existing between extruded filaments of the printed sample became smaller due to the better packing from the increased thermal conductivity imparted by reinforced fibers [188]. This leads to the initial increase of the elongation at break. However, another type of smaller-sized voids around the interface between the matrix and fibers became dominant with the increase of fiber contents. Combined with the high stiffness of CF with respect to the ductile PLA matrix, the elongation at break was largely decreased at higher CF contents. Therefore, the lower strain of 7.5 wt% CF/PLA composite justified its higher modulus than that of 5 wt% counterpart, although the latter has the highest tensile strength.

5.3.1.2 Flexural properties

The assessment of flexural properties (i.e. stiffness and strength) for composites is crucial to avoid the potential deflection and bending fracture when subjecting to high load and sliding velocity during some engineering applications. In view of this consideration, flexural tests were conducted to compare the 3D printed neat PLA samples with CF reinforced PLA counterparts via three-point bending method. As shown in **Figure 5.5**, both of flexural strength and modulus for neat PLA and CF/PLA composites exhibited the same trend with those from tensile characterization. In contrast to the PLA samples, the largest flexural strength and modulus were climbed to 57.60 MPa and 2.91 Gpa at 15 wt% CF/PLA composites, which were respectively increased by 43.00% and 185.29%. Likewise, the big improvement of flexural performance (especially for the modulus) at the fiber content of 15 wt% can be attributed to the incorporation of CF with high stiffness. However, due to the poor interfacial adhesion between CFs and the PLA matrix, more void defects caused by fibers might be formed with the increase of CF contents. The high porosity coupled with numerous stress concentration areas to a certain extent accelerated the bending failure of CF reinforced composites. It well explained the relatively low flexural strength and modulus for 10 wt% CF/PLA composite. Thus, a trade-off between CF content and porosity plays a vital role in determining the final flexural properties.

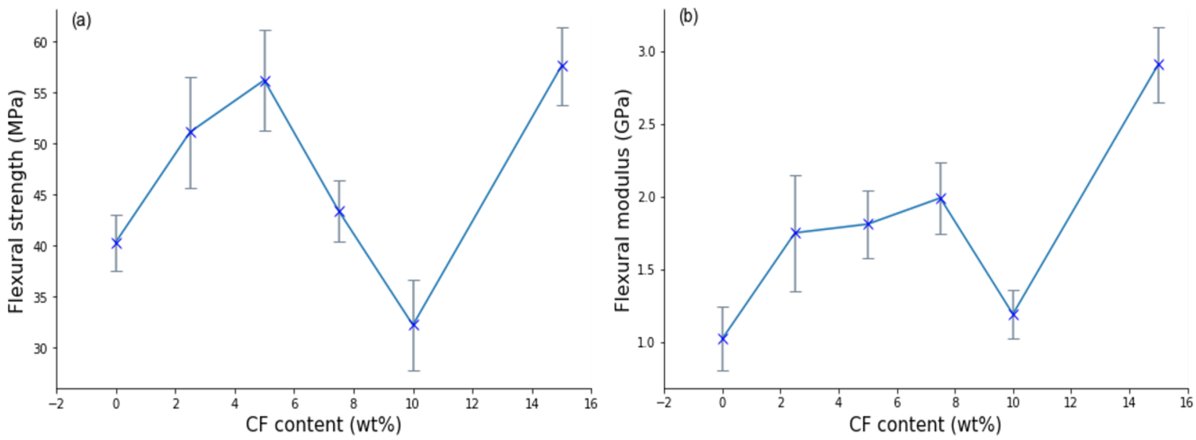

Figure 5.5 Flexural properties of 3D printed CF/PLA composites with varying CF contents: (a) flexural strength and (b) flexural modulus.

5.3.1.3 Hardness

The Rockwell hardness of 3D printed neat PLA and CF/PLA composites as a function of varying fiber contents was investigated since a higher hardness for mechanical applications is favourable to endow the materials with stronger resistance to penetration, wear, cutting and scratching [263]. The results in **Figure 5.6** showed that with the increase of CF contents from 0 wt% to 5 wt%, the hardness of CF/PLA composite was improved by 131.92% compared to the unreinforced PLA sample. By virtue of the high modulus and hardness, CFs were overlapped with each other during the FDM-based printing and formed a skeletal composite structure with increased number of linkage points. It acted as an integrated entity to enhance resistance in deformation under external pressure by impeding the movement of matrix polymer chain [228, 264]. As CF contents increased up to 10 wt%, the hardness of PLA composites exhibited a slight and sustained drop, which can be ascribed to more yielded voids and improper interfacial bonding with higher fiber quantity, leading to the excessive slippage during loading. With the further addition of CF contents from 10 wt% to 15 wt%, the hardness for CF/PLA composite showed an upward trend again due to the beneficial preponderance from the reinforced CF of high stiffness.

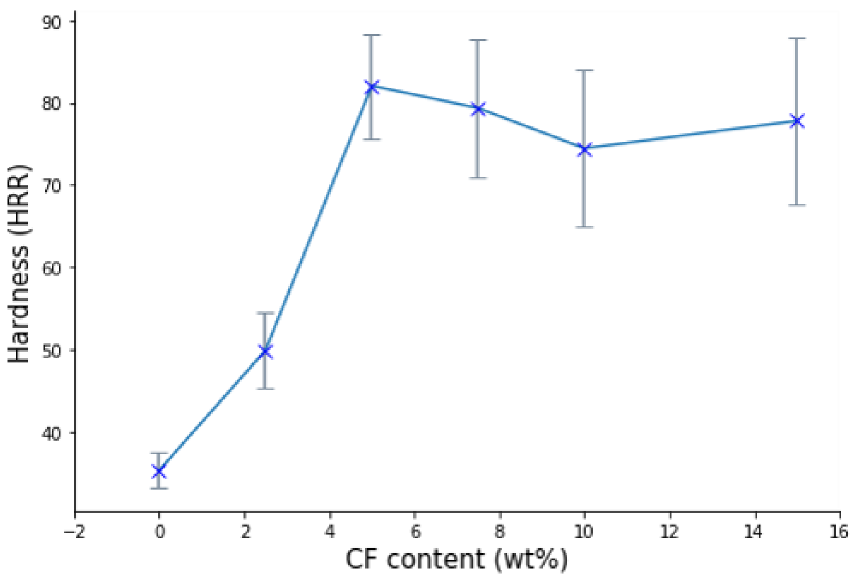

Figure 5.6 Rockwell harness of 3D printed CF/PLA composites with varying CF contents.

5.3.2 Thermal properties

The effect of CF contents on the thermal conductivity of PLA composites were examined and the corresponding results were presented in **Figure 5.7** with the rising content of CF from 0 wt% to 5 wt%, the thermal conductivity gradually increased from 0.1342 W/m·K to 0.1350 W/m·K. The improvement can be foreseeable based on the higher thermal conductivity of CFs than the PLA matrix in this composite structure, where CFs established an interconnected heat network to enhance the conductivity [210]. However, due to the existence of more fiber-matrix interface voids at higher CF contents, a reduction trend for the conductivity was occurred until the thermally conductive CF led the chief advantage after its content exceeded 10 wt%. Less than what was expected, there were not significant differences between each samples with varying CF contents. The addition of fibers indeed can raise the thermal conductivity of the composite but plays a weakening role in the interlayer fusion. This could be owing to the low conformity of CFs to the previous layer, thus decreasing the contact area for each adjoining layer during the FDM printing. This phenomenon has been reflected on the work from Love et al. that the out-of-plane tensile performance of the unreinforced thermoplastic was found to be better than that of CF reinforced composites [204]. Furthermore, fibers tend to align within a layer in the direction of printing and could not cross over the two-dimensional plane, largely restricting the heat flow in the z-direction [290]. It can be clearly seen that thermal conductivity measurements of these 3D printed composites are well consistent with all the above mechanical test results.

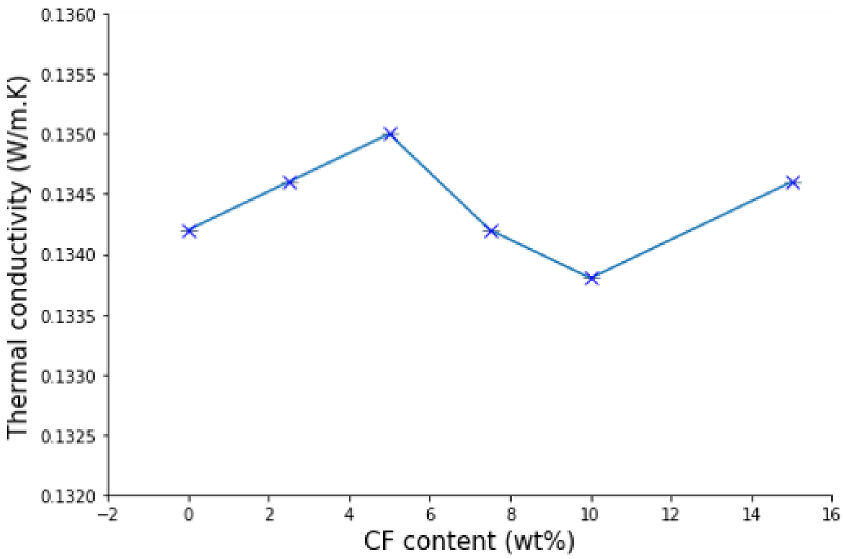

Figure 5.7 Thermal conductivity of 3D printed CF/PLA composites with varying CF contents.

5.3.3 Morphological properties

The fractural surfaces of 3D printed PLA and CF/PLA composites with varying CF contents were demonstrated via SEM analysis. Large voids with triangular shape (i.e. inter-filament pores) were obviously distributed between the deposited filaments during printing (**Figure 5.8a**). According to the layer-by-layer deposition principle highlighted in the FDM process, the melted filament is extruded from the nozzle and squeezed onto the printing bed. Since the deposited filament is still soft from the heat of extrusion, the bottom part is then flattened, and the top part exhibited a circular, convex structure after cooling down. For this void formation mechanism, continuous triangular gaps are formed along the direction of printing. However, as the incorporation of CF into the PLA matrix, various small voids (i.e. intra-filament pores) formed inside the extruded composite filaments. As shown in **Figure 5.9**, the porosity inside these filaments can be categorized into two types: the first type was those hollow holes on the fractural interface from the fiber pull-out during the failure of tested samples, and the second type was the visible gaps existed around the fiber-matrix interface. Both of these two pore types can be attributed to the poor interfacial bonding strength between CFs and the PLA matrix, which may lead to a certain decrease in mechanical, thermal and electrical performance of the 3D printed composite parts. Hence, surface modifications of fibers with suitable physical and chemical treatments are desirable to eliminate small intra-filament pores during the FDM fabrication.

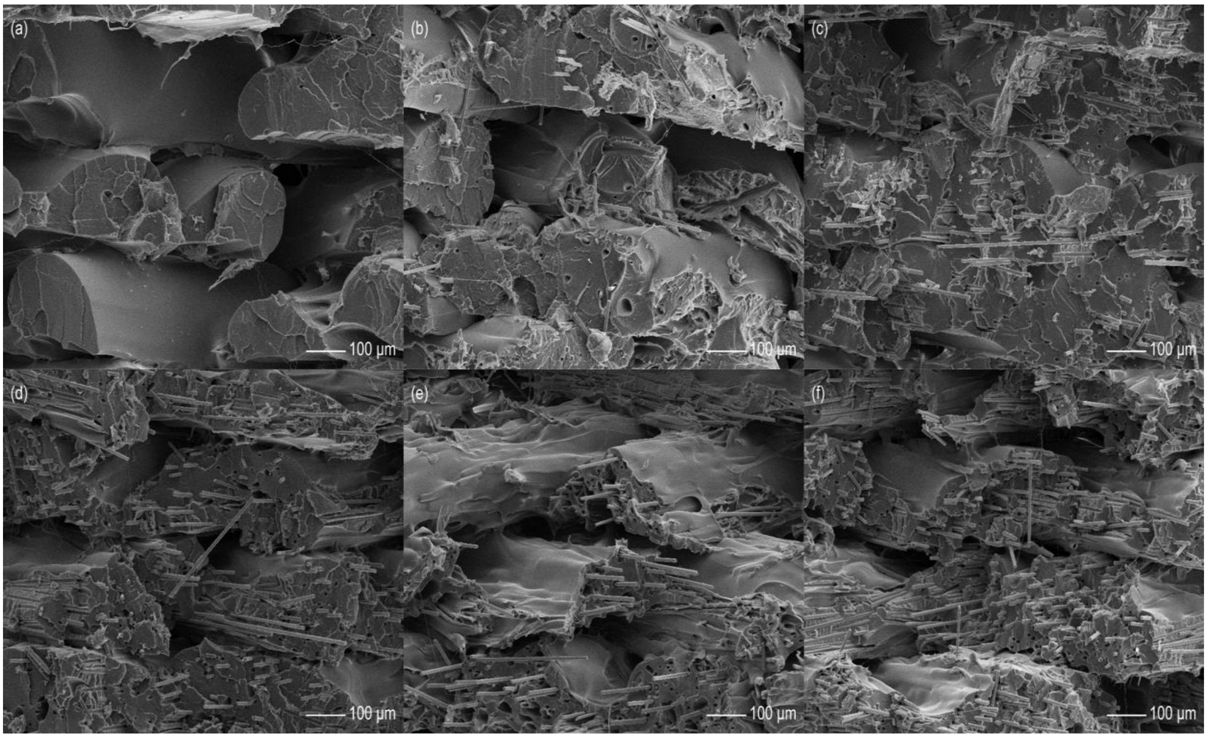

Figure 5.8 The SEM fractural interfaces of CF/PLA composites with (a) 0 wt% CF, (b) 2.5 wt% CF, (c) 5 wt% CF, (d) 7.5 wt% CF, (e) 10 wt% CF and (f) 15 wt% CF at ×300 magnification.

On the other hand, CFs in all these samples were preferentially aligned along the printing direction at a ±45º raster angle between neighbouring layers (**Figure 5.8b-f**). This behaviour was mainly caused by the huge shear rate during the nozzle extrusion. The 3D printing CF/PLA composite filament was pushed forward with external force to the nozzle entrance with a much smaller diameter. With the aid of heating up to a high temperature (i.e. 200 ºC), the composite was melt down and squeezed through the small-sized nozzle, resulting in a large velocity gradient in the flow direction. The huge shear stress generated from this extrusion process then forced CFs in the melt PLA matrix to orient along the flow direction so that the flow resistance can be minimized. It well explained the trend of these fibers to be arranged in the same direction with the matrix flow during extrusion. This phenomenon of aligned CF distribution in FDM fabricated composites has also been demonstrated in other reports [186, 191].

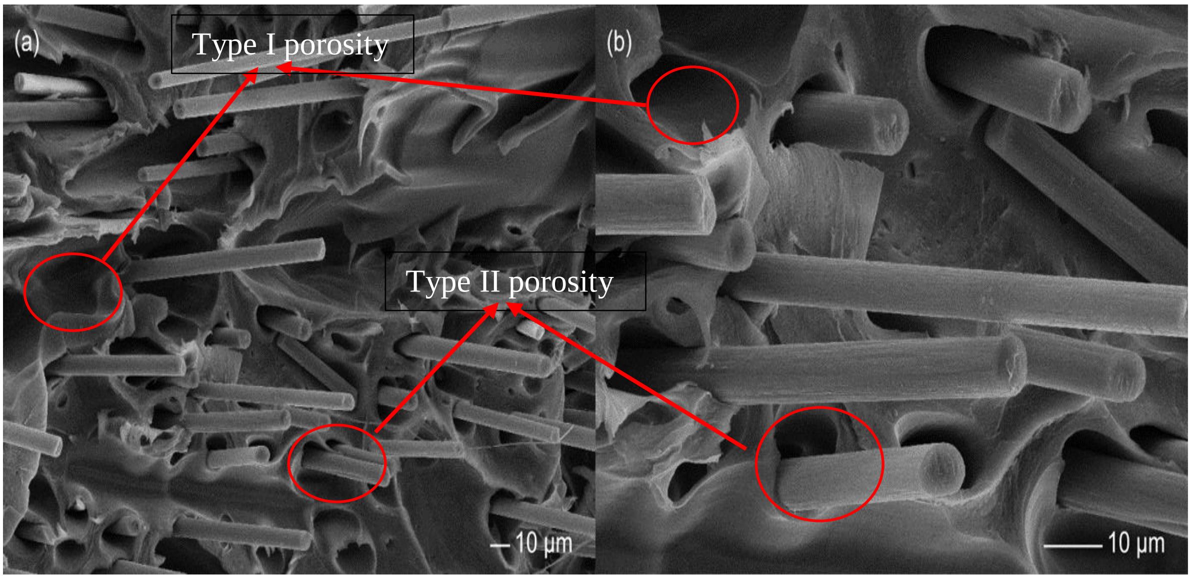

Figure 5.9 The SEM fractural interfaces of 5 wt% CF/PLA composites at (a)×1000 magnification and (b) ×3000 magnification.

As it was seen in **Figure 5.10**, the big size of triangular voids became smaller with the increase of CF contents from 0 wt% to 5wt%. This can be attributed to the improvement of thermal conductivity and reduction of the die swell after the addition of CFs. Although much smaller pores were introduced into the extruded composite filament from the weak fiber-matrix adhesion, the competing effects between the increasing fiber-induced pores and the shrinking of big inter-filament voids contributed to the conspicuous decrease for the entire porosity of 3D printed samples. However, due to the low conformity of CFs and less matrix involvement at higher CF contents (i.e. 7.5 wt %-10 wt%), the contact area between neighbouring deposited filaments was reduced again with enlarged triangular inter-filament voids. The lowest porosity with least stress concentrations was observed at 5 wt% CF/PLA composite, leading to the best performance in the above mechanical and thermal characterizations. Since the extent of CF-induced void enlargement between extruded filaments was limited, 10 wt% CF/PLA composite exhibited a similar porosity with that from the 15 wt% counterpart. Considering all these factors together (i.e. inter-filament voids, intra-filament pores and CF contents), it clearly accounts for the worst mechanical and thermal properties from 10 wt% CF/PLA composite. In short, all of these SEM observations at the fractural surfaces of composite samples well corresponded to the results from the mechanical and thermal tests mentioned in Section 3.1 and 3.2.

Figure 5.10 The SEM fractural interfaces of CF/PLA composites with (a) 0 wt% CF, (b) 2.5 wt% CF, (c) 5 wt% CF, (d) 7.5 wt% CF, (e) 10 wt% CF and (f) 15 wt% CF at ×100 magnification.

5.3.4 Gaussian process modelling

The application of machine learning into the study of FDM composite system provides a promising tool to probe the optimal fiber/polymer composite printing given its faster and smarter computing capacity compared to conventional modelling tools [291-294]. As the data size achieved from experimental analysis was relatively small and multiple output was required, Gaussian Process with different vector valued functions was chosen for the modelling. Compared to other models, it can directly capture uncertainty measurements and provide a distribution for the prediction value. In order to further investigate the mechanical pattern aiming at varying CF contents, the model was applied to perform multi-output learning with the construction of coregionalization matrix via GPy framework. Radius Bias Function (RBF) [295-297] was adopted to be the fundamental kernel function since it expressed the intuition that experimental results at nearby CF contents were more correlated than those at remote CF contents. According to the above experimental data, all of mechanical properties were not considered to be the addictive kernel function. Therefore, three different covariance matrix were built by the combination of following kernel functions: (a) RBF+Matern32, (b) RBF+Polynomial and (c) RBF+RBF.

As it can be seen from **Figure 5.11**, **Figure 5.12** and **Figure 5.13**, all prediction values were very close to the experimental data with a certain level of uncertainty, which might be derived from the experimental errors. Meanwhile, all experimental measurements for mechanical tests fell into the confidence area with regards to all the three different covariance matrices. This could be an indication that the models have captured the general mechanical property patterns for these composites. With the implementation of stochastic process, the optimized performance of these three models were similar given the negative log-likelihood of 65.01, 65.28 and 69.50 respectively. Due to the difficulty in the 3D printing of PLA composite with the CF content above 15 wt%, predictions were mainly focused on the addition of CF between

0 wt% and 15 wt%. The confidence of CF contents in such range was narrower and the predictions were more accurate than those from 15 wt% CF/PLA composite. The reason might be the nature from RBF and two kernel functions of each model were both forced to handle the variation within 0 wt%-15 wt% fiber loadings. Besides, the unavailability of supporting experimental data from above 15 wt% CF contents also resulted in the derivation of these theoretical results, hampering the accurate prediction at higher CF percentages.

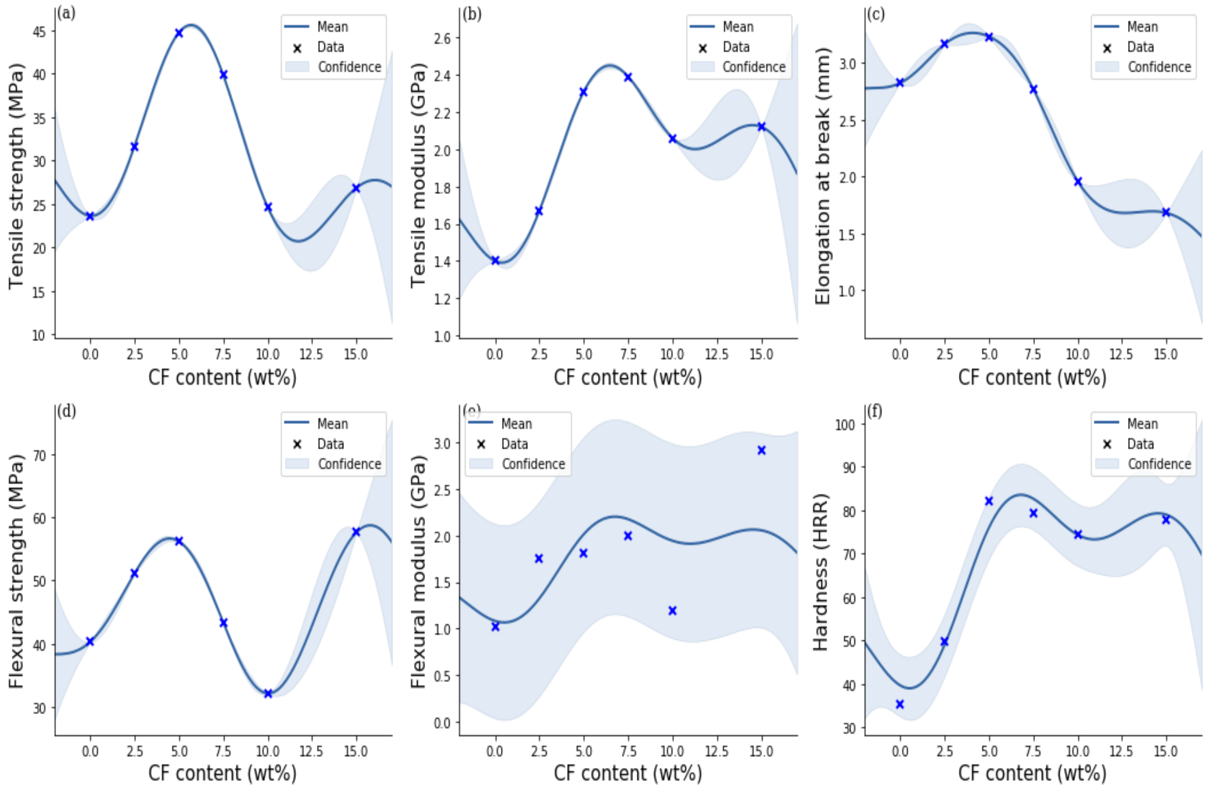

Figure 5.11 Predictions for mechanical properties of 3D printed CF/PLA composites based on RBF+Matern32 model: (a) tensile strength, (b) tensile modulus and (c) elongation at break, (d) flexural strength, (e) flexural modulus and (f) hardness.

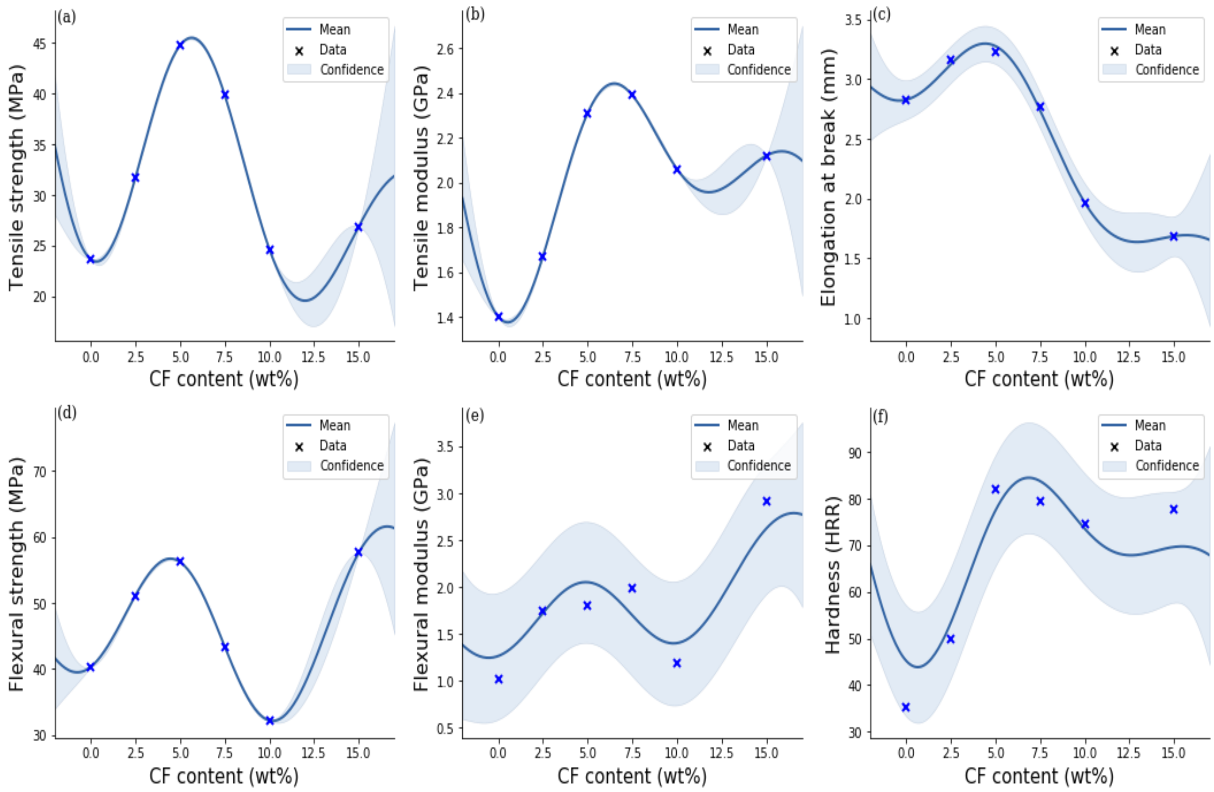

Figure 5.12 Predictions for mechanical properties of 3D printed CF/PLA composites based on RBF+Poly model: (a) tensile strength, (b) tensile modulus and (c) elongation at break, (d) flexural strength, (e) flexural modulus and (f) hardness.

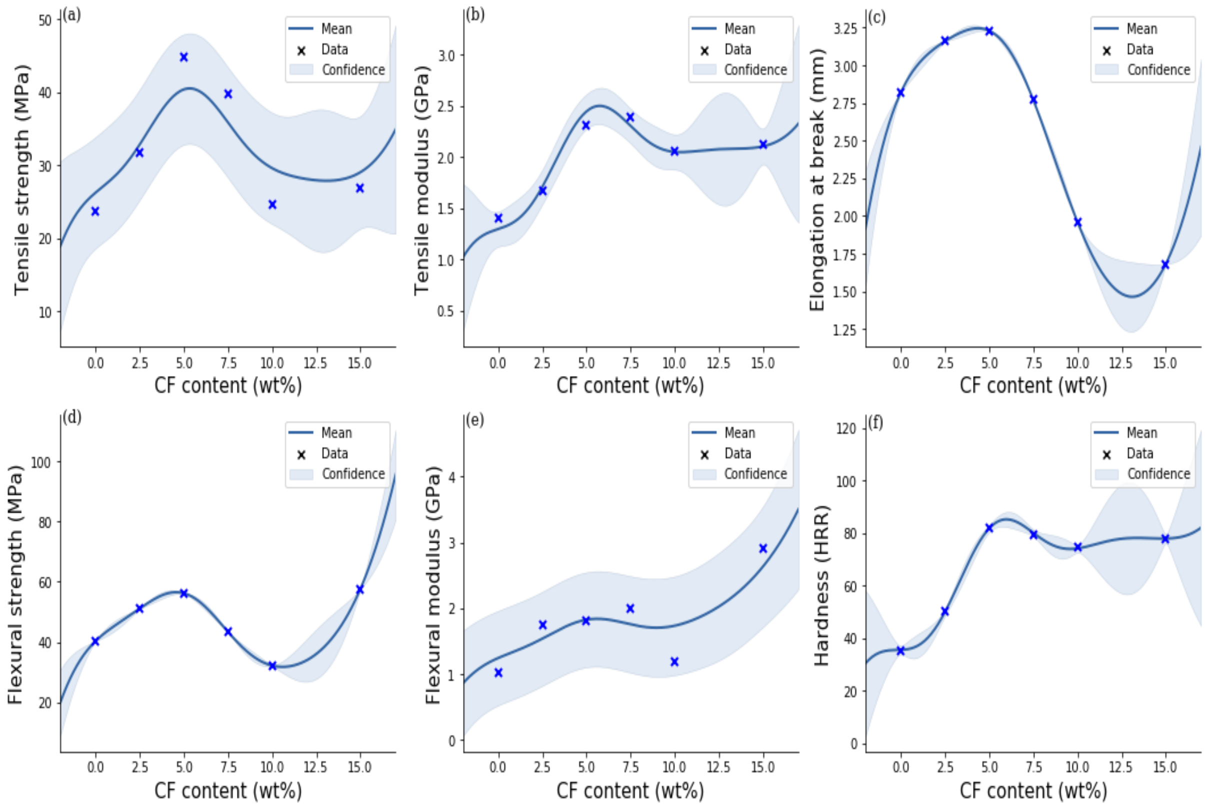

Figure 5.13 Predictions for mechanical properties of 3D printed CF/PLA composites based on RBF+RBF model: (a) tensile strength, (b) tensile modulus and (c) elongation at break, (d) flexural strength, (e) flexural modulus and (f) hardness.

Relied on model predictions, both of the largest tensile modulus and strength for CF/PLA composites can be seen at 6.7 wt% fiber content while the smallest values could be found with the introduction of 12.5% wt% CF. In terms of flexural strength and modulus, both in these models showed upward trends with the rise of fiber contents, indicating that there might be an opportunity to seek for larger flexural performance due to the limited increase of fiber-induced porosities at higher fiber loadings. The largest hardness of PLA composites was also predicted from the model with the incorporation of 6.7 wt% CF. In general, predictions of these three kernel functions were well aligned with the discussion on experimental results.

5.4 Conclusions

In this work, chopped long CF was first chosen as the reinforcement into the PLA matrix to prepare composite filaments via extrusion process and then employed as feedstock to fabricate CF reinforced composites by FDM-based printing. With the view of studying the mechanical properties of these 3D printed CF/PLA composites, tensile, flexural and hardness tests were conducted. Compared to the neat PLA, samples with 5 wt% CF had the largest tensile strength with the enhancement by 89.14% while the largest tensile modulus with the enhancement by 70.71% occurred at samples with 7.5 wt% CF. The flexural strength and modulus were climbed to the highest values at 15 wt% CF reinforced composite with the improvement by 43% and 185.29% respectively. With the increase of CF contents from 0 wt% to 15 wt%, the hardness of 5 wt% CF samples had the biggest increase by 131.92%. On the other hand, the addition of CF also affected the thermal conductivity of PLA composites with the biggest enhancement at 5 wt% CF loading. All these properties exhibited the same upward-downward-upward trend within 0-15 wt% CF contents with the best performance occurred at 5 wt% and the worst at 10 wt% CF/PLA composites, which can be attributed to the compromising competition between inter-/intra-filament porosities and the high stiffness of CF. With the aid of Gaussian Process modelling, the best mechanical performance of PLA composites within above CF range was also predicted at the addition of 6.7 wt% CF. The main limitation of this study was the difficulty of fabricating FDM composite filaments with higher CF contents via twin-screw extrusion due to the application of long fibers. Future work will be conducted on the variation of fiber length after printing and the comprehensive validation of machine learning techniques on printed CF/PLA composites. Without doubt, this research not only gives insightful information on the 3D printing of long CF reinforced composites, but provides an innovative approach to incorporate machine learning into the study of FDM-based composite system.

CHAPTER 6 3D PRINTING OF CHIRAL CARBON FIBER REINFORCED POLYLACTIC ACID COMPOSITES WITH NEGATIVE POISSON'S RATIOS

6.1 Introduction

As man-made materials with elaborately designed structures, mechanical metamaterials have attracted great attentions in recent decades by virtue of their exotic mechanical properties [298]. A typical example is auxetic materials with negative Poisson's ratios (NPR) [299-301]. Compared to conventional materials with positive Poisson's ratio, they exhibit a lateral expansion instead of contraction when stretched in the longitudinal direction, vice versa [302]. The theoretical threshold of Poisson's ratio for isotropic solid materials is -1 while for metamaterials with anisotropic geometries, lower values can be achieved without a specific limit [303]. Based on the counterintuitive behaviour of stretch-expansion deformation, remarkable physical properties are imparted to auxetic materials, such as high facture toughness, elevated shear modulus, superior specific strength, improved indentation resistance, enhanced energy dissipation capacity and controllable permeability with strain [304-310]. These appealing traits existing in auxetic materials have shown a promising application in various industries, including aerospace, automotive, construction, transportation, military defence, biomedicine, sports and so forth [311-314].

The concept of NPR effect can be dated back to 1800s when Voigt and others discovered this exotic phenomenon in some natural materials [315]. Lake was the first one to artificially fabricate the auxetic foam material in 1987 before the terminology of auxetics was coined by Evans four years later [316, 317]. After that, a variety of cellular structures with auxetic features have been proposed and created from the nano- to macro-scale level. According to their deformation mechanism, auxetic structures can be categorized into three main types: re-entrant, chiral and rotating rigid structures [318]. Of all, chiral mechanical metamaterials have deterministic handedness and more robust Poisson's ratio performance under fabrication errors either for small or large deformation [319, 320]. This can credit to its unique mechanism predicated on bending and stretching deformation of chiral units, although the NPR is hard to reach the lower limit of -1 for quasi-isotropic open-cell geometries [321].

Normally, the low mechanical performance of auxetic cellular structures largely restricts their applications, especially in load-bearing fields [322]. Making auxetic structures into composites via the incorporation of high stiffness reinforcements (e.g. high-performance fibers, metals, ceramics and nanofillers) provides an effective strategy to enhance the overall mechanical strength for the auxetic products [9, 323]. Two approaches defined by Alderson *et al.* have been widely employed to produce auxetic composites: (1) the sequential stacking of angle-ply reinforced laminates to realize the NPR effect, and (2) the introduction of auxetic elements (e.g. auxetic matrix, auxetic reinforcement or both) into the composite [324]. For instance, through using the auxetic yarn made of nylon core and carbon fiber wrap, Miller *et al.* for the first time fabricated this hybrid composite with relatively high stiffness (4 GPa) and NPR (-6.8) at 30% fiber volume content [325]. Clarke et al. found the Poisson's ratio with negative values at the ply orientation ranging between 15° and 30° when alternately stacking a series of carbon fiber reinforced epoxy composite laminates with varying ply angles [326]. By staggeringly arranging polyamide filaments, braided cotton yarns and polyester mutifilaments as weft, warp and stitch yarns in the polyurethane matrix, Zhou *et al.* demonstrated that the 3D auxetic textile composite exhibited better impact protective performance compared to the 3D non-auxetic counterpart, which can be ascribed to the higher energy absorption capacity and structural stability for auxetic structures [327].

Different from the above two general methods, other innovative strategies to fabricate auxetic composites have been studied and developed in recent years via organically integrating conventional or advanced manufacturing techniques. Here, we summarize all these strategies as the third approach: the direct building of auxetic structures with the application of composite materials. Using braided composite rods (BCRs) as the basic skeletal materials, Rana and his group explored numerous auxetic structures by placing BCRs onto the auxetic-pattern board with the aid of knotting and curing to produce auxetic composites. They not only exhibited a wide span of NPR values (-0.3~-9.0) based on the different auxetic designs, but also possessed higher tensile strength and work of rupture for the composites with stiffer fibres and more fiber contents [328-330]. Wang et al. fabricated 3D double-arrow-head and re-entrant auxetic composites through pattern-cutting carbon fiber reinforced epoxy composite laminates with computerized numerical control machine and assembling into 3D auxetic structures with interlocking and adhesion methods. These 3D auxetic composites with structural parameter-regulated NPR had higher specific stiffness than both their polymer and metal (steel) made counterparts [331, 332]. However, the techniques applied in these strategies have several constraints, such as complicated manufacturing process, long operation time, and limited size and complexity of structural production.

As a state-of-the-art technology, additive manufacturing (AM), also known as rapid prototyping or 3D printing, is ushering in a new age for the smart manufacturing of architected cellular materials with complex microstructural topologies [42, 333, 334]. In contrast to to conventional subtractive manufacturing methods, AM is a process where complex parts are produced by adding materials layer-by-layer from 3D computer models [271]. By virtue of its merits in mass customization, design freedom, waste minimization and fabrication feasibility of complex geometries with high fidelity, AM has a great potential to manufacture metamaterials with intricate, hierarchical and small repeating structures [335]. In this work, we designed a group of chiral structures with typical auxetic properties based on the polynomial curve. By maintaining a fixed primary dimension, the curvature of the unit cell in lattice structures can be regulated through inputting varying values to the order of *n*. The advanced 3D printing technique was also utilized in the fabrication of these auxetic polylactic acid (PLA) composites with carbon fiber (CF) as the reinforcement. Uniaxial tensile tests were conducted to investigate the effects of polynomial-based chiral geometries and CF on deformation responses and mechanical performance of these fiber reinforced composites. Furthermore, finite element analysis (FEA) [336-339], rather than theoretical solution approaches which are available for problems with simple geometry and loading conditions only [340-346], was introduced to offer additional insights into the underlying mechanism responsible for the observed tensile phenomena. **Fig.1** below provides an overview of the fabrication process of the chiral samples used in this study.

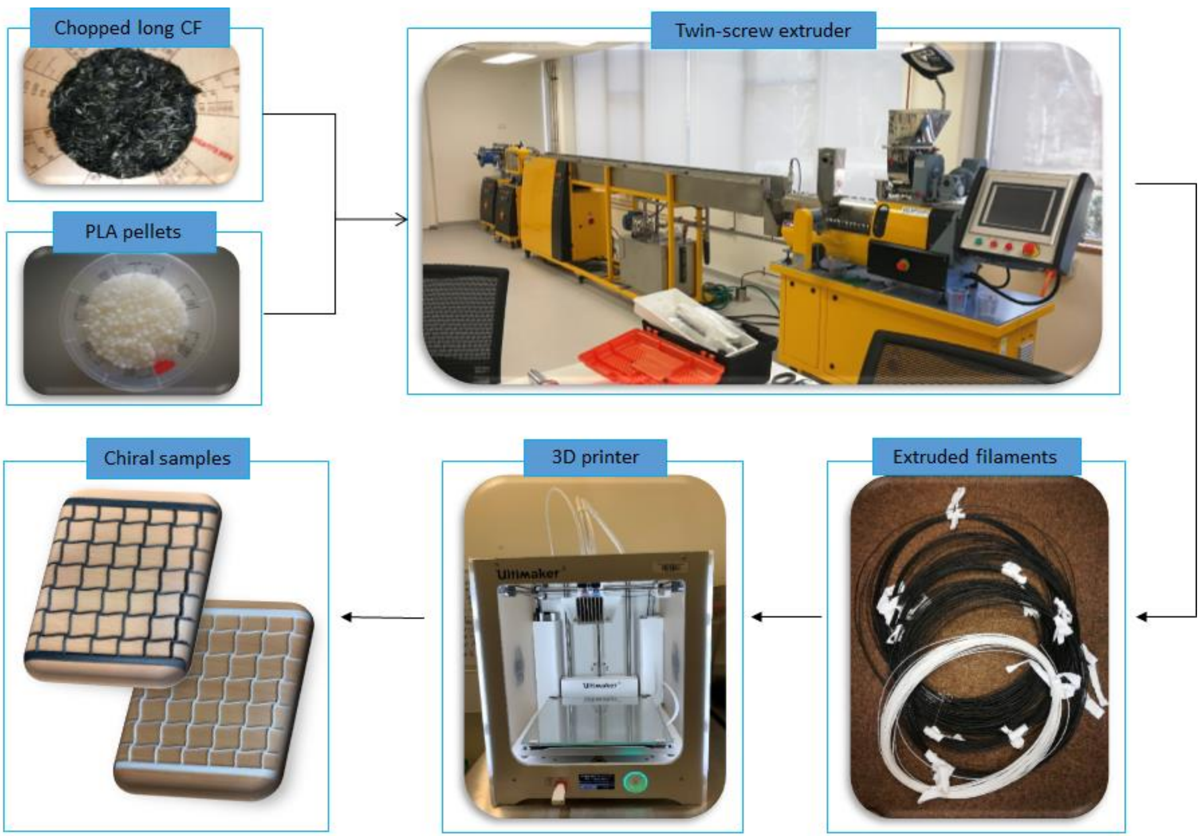

Figure 6.1 The fabrication process of PLA and CF/PLA chiral samples.

6.2 Methodology

6.2.1 Designs

The 2D auxetic lattices of test samples were designed into four templates. All were variations of the four-pronged chiral structure where the branches were in a polynomial shape. This structure contained identical repeating unit cells in translational symmetry. Each unit cell is comprised of four branches joined at the centre of the unit cell with rotational symmetry. **Figure 6.2a** presented a direct overview of the four different unit cell designs overlapped on each other. These variations corresponded to different polynomial orders (*n*) of 1.5, 2, 3, and 4. As the *n* value was increased, the curvature in the branches became more significant. In **Figure 6.2b**, the primary dimension of the unit cell was defined as a = 18 mm, while the width of branches was set as t = 2 mm. The shaded area represented the square core conjoining the four branches, while the curvature of branches was defined in the following polynomial relationship:

$$\frac{y - y_A}{y_B - y_A} = \left(\frac{x - x_A}{x_B - x_A} \right)^n \quad (1)$$

And:

$$\frac{y - y_C}{y_D - y_C} = \left(\frac{x - x_C}{x_D - x_C} \right)^n \quad (2)$$

The auxetic sample with the chiral pattern was shown in **Figure 6.2c**, in which the whole structure was consisted of 6 × 6 repeating units of the four-pronged cell, each rotated 45° around its center.

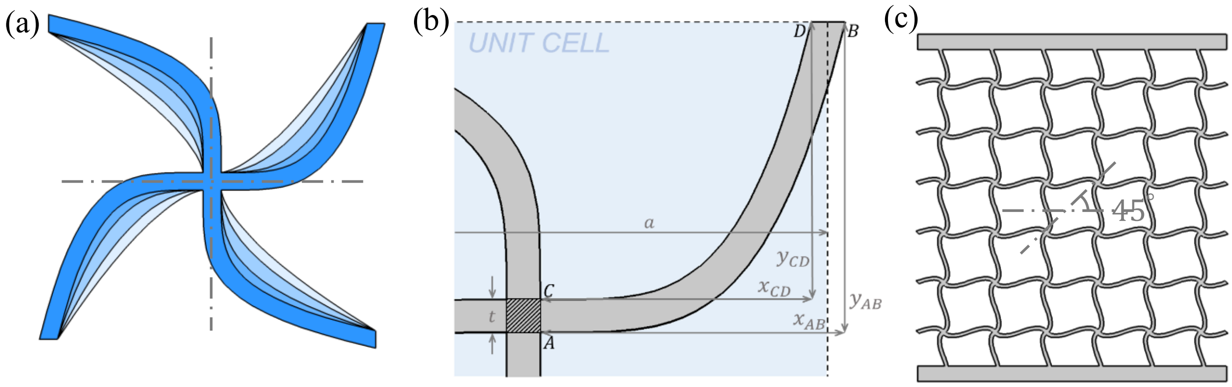

Figure 6.2 Design of the chiral pattern: (a) unit cell variations at n = 1.5, 2, 3 and 4; (b) shape parameters defining the geometry of the unit cell; and (c) the 6 × 6 test sample consisting of repeating units that are rotated 45° around the center.

6.2.2 Materials

The natural PLA pellets were purchased from Aurarum Pty Ltd (Keysborough, Australia) with the melting point ranging between 185 ºC and 220 ºC. The chopped polyacrylonitrile-derived CF was supplied by ACP Composites (Livermore, USA) as the reinforcement for the fabrication of 3D printing composite filaments. The average length of this CF in chopped form is 4.6 mm and its common diameter is 7 µm.

6.2.3 Twin-screw extrusion

The pure PLA filament and CF/PLA composite filament with 5 wt% CF contents were prepared via an industrialized co-rotating twin-screw extrusion system (LTE16-44, Labtech Engineering, Thailand). Specializing in the manufacturing of 3D printing filaments, it consists of four units: 1. the twin-screw extruder unit to melt, mix and extrude the continuous filament; 2. the water bath unit to cool down and solidify the extrudate; 3. the caterpillar hall-off unit to convey the extruded filament; and 4. the wind-up unit to collect the filament onto a spool. The extruder has two screws with the diameter of 16 mm and length/diameter ratio of 44 mm in the 11 temperature zone-controlled barrel. As shown in **Table 6.1**, all processing parameters involved in the fabrication of CF/PLA composite filaments were optimized so as to achieve the uniform circular shape with the average diameter of 2.85 mm for 3D printing.

Table 6.1 Processing parameters employed in the fabrication of 3D printing filaments via the industrialized twin-screw extrusion system.

Heating zones	Z1	Z2	Z3	Z4	Z5	Z6	Z7	Z8	Z9	Z10	Die
Temperature (ºC)	200	200	200	180	180	180	180	180	180	180	180
Screw speed (rpm)						25					
Water bath temperature (ºC)						20					
Hall-off speed (m/min)						3.2					
Wind-up tension (Nm)						1.0					

6.2.4 3D printing

All the chiral structures made by pure PLA and CF/PLA composite were printed by feeding these extruded filaments into a commercial FDM printer (Ultimaker 3, Ultimaker, Netherlands) with the nozzle diameter of 0.4 mm. During printing, the nozzle temperature was set at 200 ºC while the build plate temperature was 60 ºC. The printing speed was controlled at 70 mm/s with the thickness of each layer maintained at 0.1 mm. The raster angle for deposition directions of different layers were +45º and -45º. The infill percentage was set at 100 %. All the processing parameters were regulated by using the Cura software. In order to prevent warping and enhance bed adhesion during printing, the raft that can be easily peeled off was introduced at the bottom of printed samples. The 3D printed chiral structures with varying *n* values are presented in **Figure 6.3**.

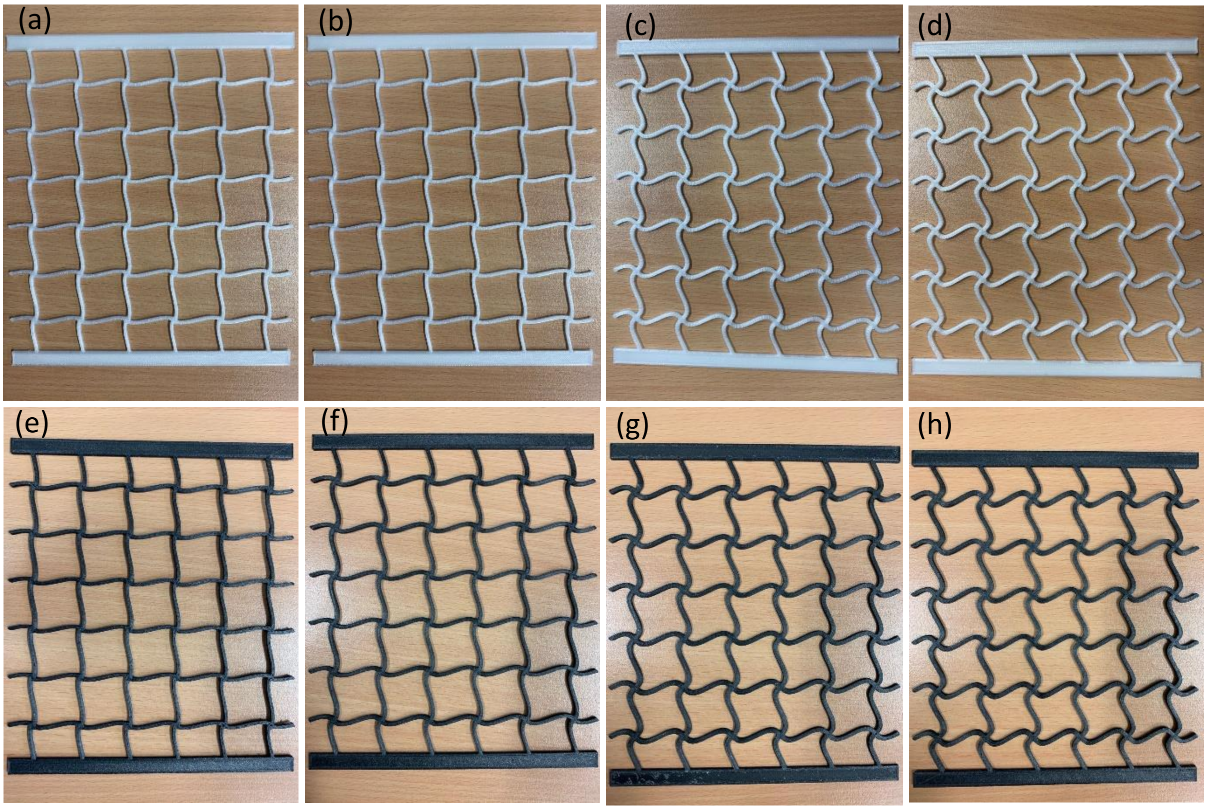

Figure 6.3 3D printed chiral lattices with different polynomial orders of n=1.5, 2, 3 and 4: (a)-(d) neat PLA; (e)-(h) CF/PLA composites.

6.2.5 Sample characterization

The tensile tests for pure auxetic PLA and auxetic CF/PLA composites were conducted using a universal testing machine (Zwick Z010, Zwick GmbH, Germany) with the load cell capacity of 10 KN. The displacement was controlled at a speed of 5 mm/min to keep a quasi-static load condition. All samples were tested with the deformation process being recorded via a 2D digital image correlation (DIC) system in the ambient temperature and humidity (25 ºC, 33%RH). The top and bottom ends of each sample were clamped by a 2 mm-thick aluminium sheet and then loaded into the fixture. Prior to the tests, special black and white paintings were sprayed onto the polished front surface through an airbrush to create speckle patterns[347]. The experimental setup and the speckle pattern of the sample were given in **Figure 6.4**.

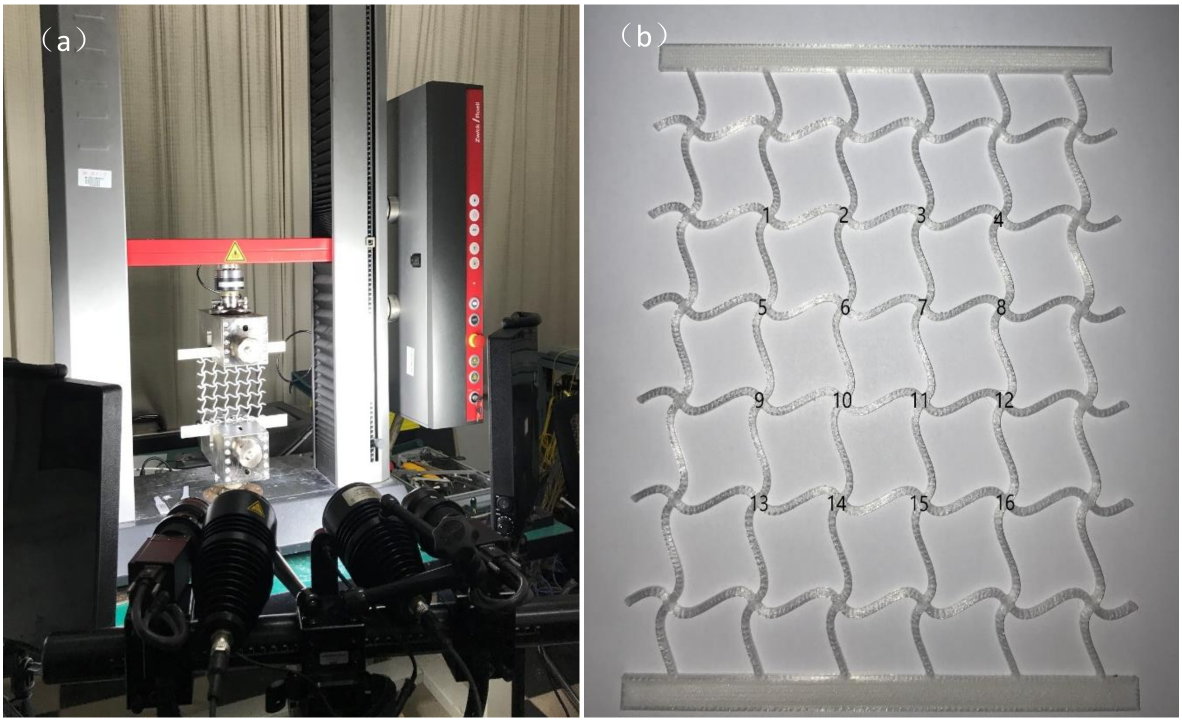

Figure 6.4 Experiment for sample characterization: (a) tensile setup and DIC system; (b) numbers showing the speckle pattern on the sample front surface.

ARAMIS v6.3.1 (GOM mbH, Germany) and VIC-2D (CSI, USA) DIC system were employed to capture the real time full-field strain in the front view of chiral structures. The sampling rate of the camera was set to be three images per second to describe the deformation evolution during the quasi-static tensile test until the sample was fractured with the peak force decreased to 20%. Specifically, a 2448 × 2050 pixels CCD camera equipped with a lens of 50 mm focal length was used to acquire the images. All the measurement results after tests were analysed via the DIC professional software (ARAMIS, Germany). To ensure the accuracy of computation, the facet size and facet step were set to be 9 × 9 pixels and 5 × 5 pixels to calculate the deformation of the front view for these samples.

The fracture surfaces of neat PLA and CF/PLA composites after tensile test were observed by employing a scanning electron microscope (GeminiSEM 500, ZEISS, Germany) with the acceleration voltage of 15 kV. In order to prevent the charging effect on the surface, all samples were sputter coated with a thin layer of gold before imaging to enhance the electric conductivity and SEM resolution.

6.2.6 Finite element methods

To validate our experimental data, finite element simulations [348-351] were employed to assess the elastic behaviour of the chiral auxetic pattern. Commercial FEA package COMSOL 5.3 was used to devise the solid mechanics solver for Poisson’s Ratio calculation. The two-dimensional structure was meshed with triangular elements refined at curvatures and conjunctions to reach convergence. A plane-stress condition was considered to reflect the loading configuration of the tensile testing platform. Due to the complex mechanical anisotropy in 3D-printed specimens caused by various CF orientations, FEA simulations were only conducted using the following mechanical properties of pure PLA, assuming homogeneity.

$$E_x = E_y = 1.40\ GPa;\ \ \nu_{xy} = \nu_{yx} = 0.33;\ \ \ \rho = 1.24\ g/cm^3 \tag{3}$$

To achieve precise stepwise calculation of the Poisson's ratio of the structure, geometric nonlinearity was enforced with additive strain decomposition. The sample model was subject to fixed constraints on boundary at the positive y end of the domain and gradually increased tensile displacement on the negative y boundary (**Figure 6.5**). The loading rate is set at 5mm/min to simulate the scenario of mechanical tensile testing. Internal nodes were monitored to avoid inaccuracy due to Saint-Venant end effects.

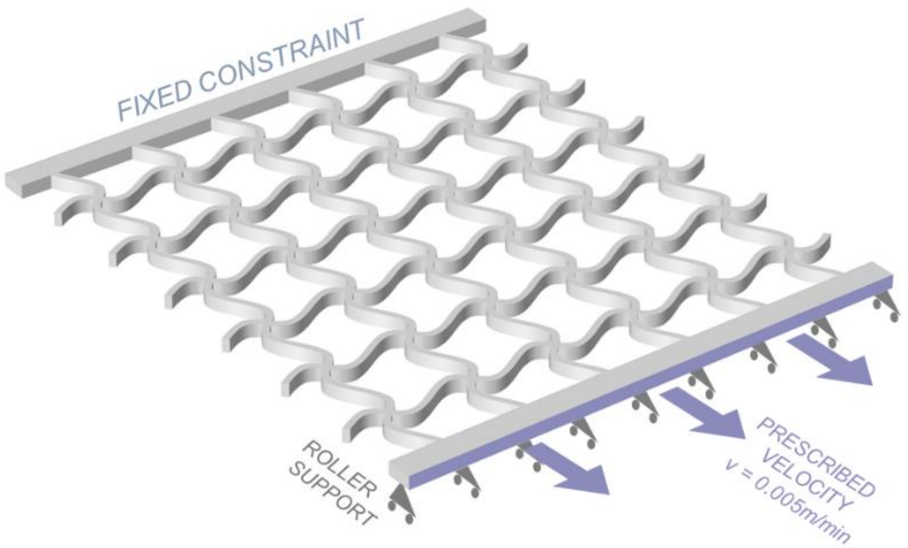

Figure 6.5 Boundary conditions for mechnanical simulation in FEA.

The Poisson's ratio of the structure is calculated from stepwise displacement data. In particular, the Poisson's ratio at time *t*, under tensile loading in the *y* direction can be derived from the local displacement data retrieved from the monitored nodes:

$$u_{0,n} = U_0 * t; \tag{4}$$

$$X = x_1 - x_2 = 3 * a * (2 * \cos\frac{\pi}{4}); \tag{5}$$

$$\Delta X = X(t) - X = u_1 - u_2; \tag{6}$$

$$\varepsilon_x(t) = \frac{\Delta X}{X} = \frac{u_1 - u_2}{3\sqrt{2} * a} \tag{7}$$

Similarly,

$$\varepsilon_y(t) = \frac{\Delta Y}{Y} = \frac{v_1 - v_2}{3\sqrt{2} * a} \tag{8}$$

$$v_{yx}(t) = -\frac{\varepsilon_x(t)}{\varepsilon_y(t)} \tag{9}$$

where u_1, v_1, u_2 and v_2 represents the x- and y-components of local displacement at the two nodes. $u_{0,n}$ is the time-dependant prescribed displacement at the lower end of the specimen.

6.3 Results and discussion

6.3.1 Auxetic behaviour of chiral structures

Under the axial tensile loading, the original chiral structure extended longitudinally and the curved branches gradually became straight. This change was caused by the torque generated from the load, inducing a moment on the branches of each unit cell to bend. The deformation process of the structure would shift from the bending-dominated mode to the one dominated via stretching when the tangential direction of these bending branches were gradually in line with the loading direction. During this deformation process as can be seen in **Figure 6.6b**, the core of unit cell experienced a counter-clockwise rotation because of the bending. Meanwhile, all the four branches uncoiled and were straightened simultaneously, evidenced in **Figure 6.6c**. The deformation caused stress concentration near the surface of the curved branch, typical of engineering materials subject to a bending moment. Therefore, when the unit cell of these chiral structures elongated in the longitudinal direction under the tensile force, it expanded laterally as well, achieving the auxetic feature with the corresponding NPR. As shown in **Figure 6.6a**, when a tensile force *F* was applied, both Δx and Δy appeared positive.

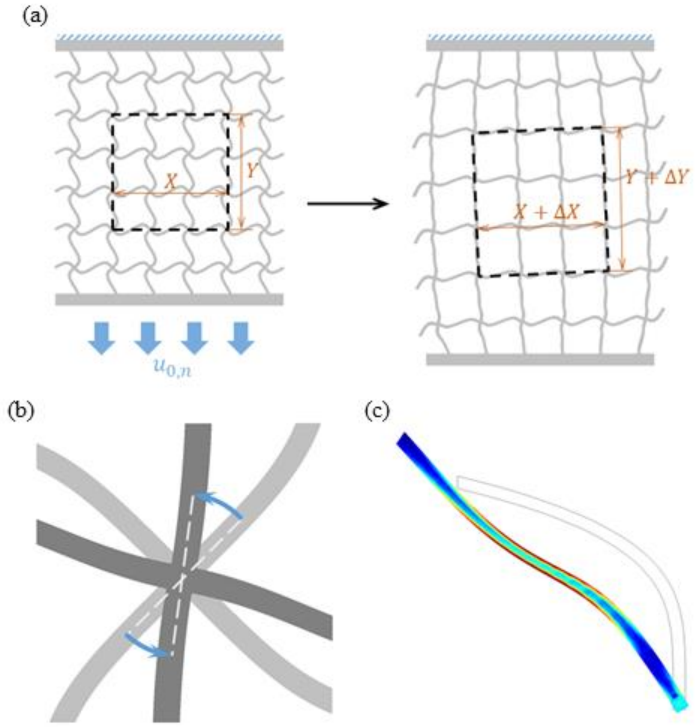

Figure 6.6 Schematics for the deformation of unit cell under the application of tensile loading: (a) expansion in both x- and y-axis direction; (b) counter-clockwise rotation of the unit cell core; and (c) straightened branch under tensional deformation.

6.3.2 The effect of polynomial orders on auxetic behavior

The experimental and theoretical Poisson's ratios for the neat PLA and CF/PLA chiral composites with varying polynomial orders were given in **Figure 6.7** and **Figure 6.8**. It should be noted that all Poisson's ratios were discussed within a narrow range of nominal strain before the first collapse of unit cell occurred in the stretched lattice structure, which can be attributed to the high brittleness of the PLA matrix. As to *n* = 1.5 (**Figure 6.7a**), the Poisson's ratio in the neat PLA sample increased from -0.487 to -0.427 by 12.3% with the increase of longitudinal strain. In contrast, the Poisson's ratio of the chiral structure exhibited a small undulate trend (fluctuation range ≤ 8%) in other polynomial orders (**Figure 6.7b-d**). Conspicuously, the deformation of the structure with the smallest *n* value was more sensitive to the tensile strain. Of all these four templates, the polynomial-derived structure with $n = 2$ had the smallest average Poisson's ratio (-0.493) while the largest average value (-0.452) was found in the $n = 4$ lattice. All these chiral structures maintained the auxetic behaviour within the strain range. Although the measured Poisson's ratios were a little bit smaller than those in FEA prediction, a good agreement between the experiment and simulation still can be seen in **Figure 6.7**. The main reason for this result was mainly due to the inherent defect in FDM printing, in which inter-bead voids can be formed inside the printed part.

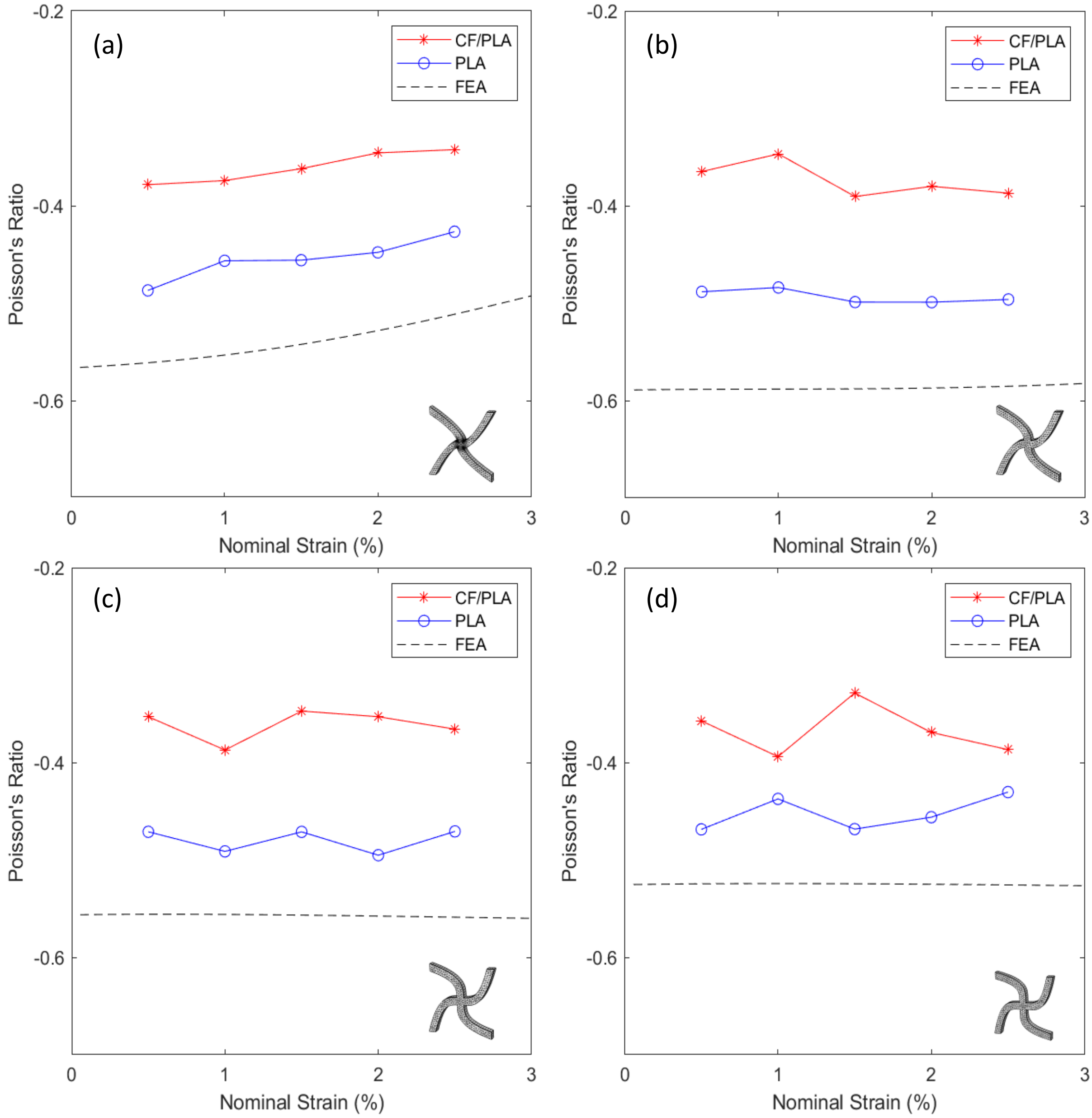

Figure 6.7 Experiment and modelling prediction of Poisson's ratios in neat PLA and CF/PLA chiral composites with different polynomial orders: (a) n = 1.5; (b) n = 2; (c) n = 3; and (d) n = 4.

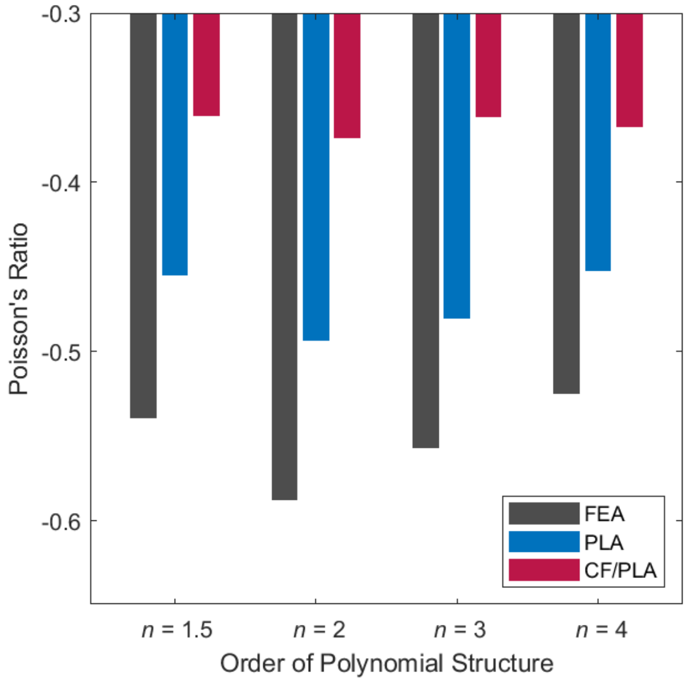

Figure 6.8 Average values of experimental and theoretical Poisson's ratios in neat PLA and CF/PLA chiral composites with different polynomial orders: (a) n = 1.5; (b) n = 2; (c) n = 3; and (d) n = 4.

For the option of these polynomial orders, a primininary test based on finite element simulation was also conducted, as it can be seen in **Figure 6.9**. With the increase of *n* value from 0 to 10, the Poisson's ratio increased to the peak at *n*=2 and then gradually decreased with a tendency to a constant value (-0.47). In addition, an obvious variation of Poisson's ratios appreared around the polynomial order of 2. Therefore, four n values (i.e. 1.5, 2, 3 and 4) were chosen in this study so that the influence of polynomial orders on the auxetic behavior can be clearly reflected whether in the modelling or experimental characterization.

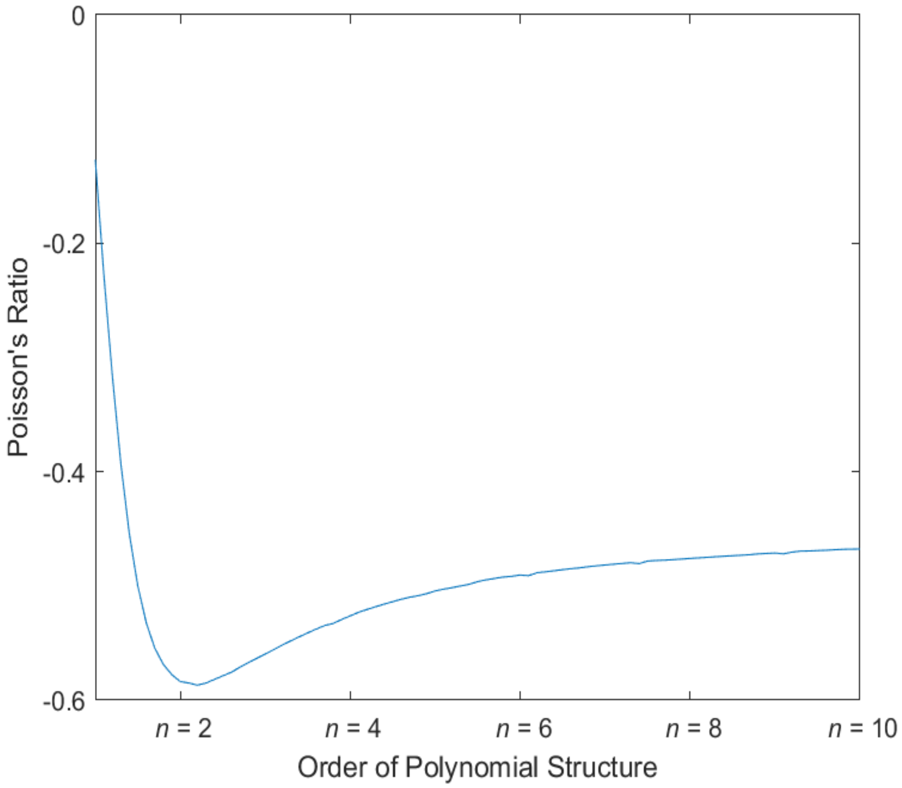

Figure 6.9 The correlation of Poisson's ratios and polynomial orders in the chiral structure.

6.3.3 The effect of CF on auxetic behaviour

The mode and degree of deformation in a cellular lattice not only depend on the topological design of the unit cell, but are related to the material properties of the structure [352]. As shown in the **Figure 6.7** and **Figure 6.8** above, although the chiral composites presented the same trend with the neat PLA counterparts with the variation of polynomial orders, all measured values of Poisson’s ratios in composites were smaller than those in single polymer structures. This could be easily understood by the incorporation of high stiffness fibers (i.e. CF). These chiral composites still exhibited auxetic behavior with NPRs, while this performance became weak owing to the existence of fiber fillers. The high resistance of CF to the lattice deformation and the increased anisotropy inside the printed composite sample resulted in the increased

Poisson's ratios. Besides, these two factors also contributed to the largely improved mechanical properties in composites, which were discussed hereinafter.

6.3.4 Tensile behaviour of chiral structures

The tensile behaviour of these 3D printed neat PLA and CF/PLA chiral composites with varying polynomial orders was shown in **Figure 6.10**. When the structure was stretched in-plane, the bending of curvy branches gave a linear elastic deformation until the lattice reached a critical strain limit. Dependent upon the material properties for the load-bearing capacity, the cells inside the structure started to collapse due to plastic yielding and brittle fracture [353]. During this elastic-plastic collapse process, the chiral lattice not only was influenced by the bending of curvy branches, but underwent stretch-induced tension along the loading direction. This can be attributed to the increased stiffness in the structure, preventing the continuity of branch bending. It can be seen in **Figure 6.10** that all chiral samples exhibited a similar tensile behaviour with an initial linear stress-strain region where unit cells were deformed uniformly. However, a sudden drop occurred after the stress reached its maximum. This can be explained by the instability of polynomial-derived chiral structures during the tensile deformation, in which the locally maximized stress resulted in a catastrophic failure. After that, the stress value increased again with the branch stretch until the next break of a unit cell. The cyclic process for the increase and decrease of the stress lasted to the end because of the succeeding collapse of these chiral cells.

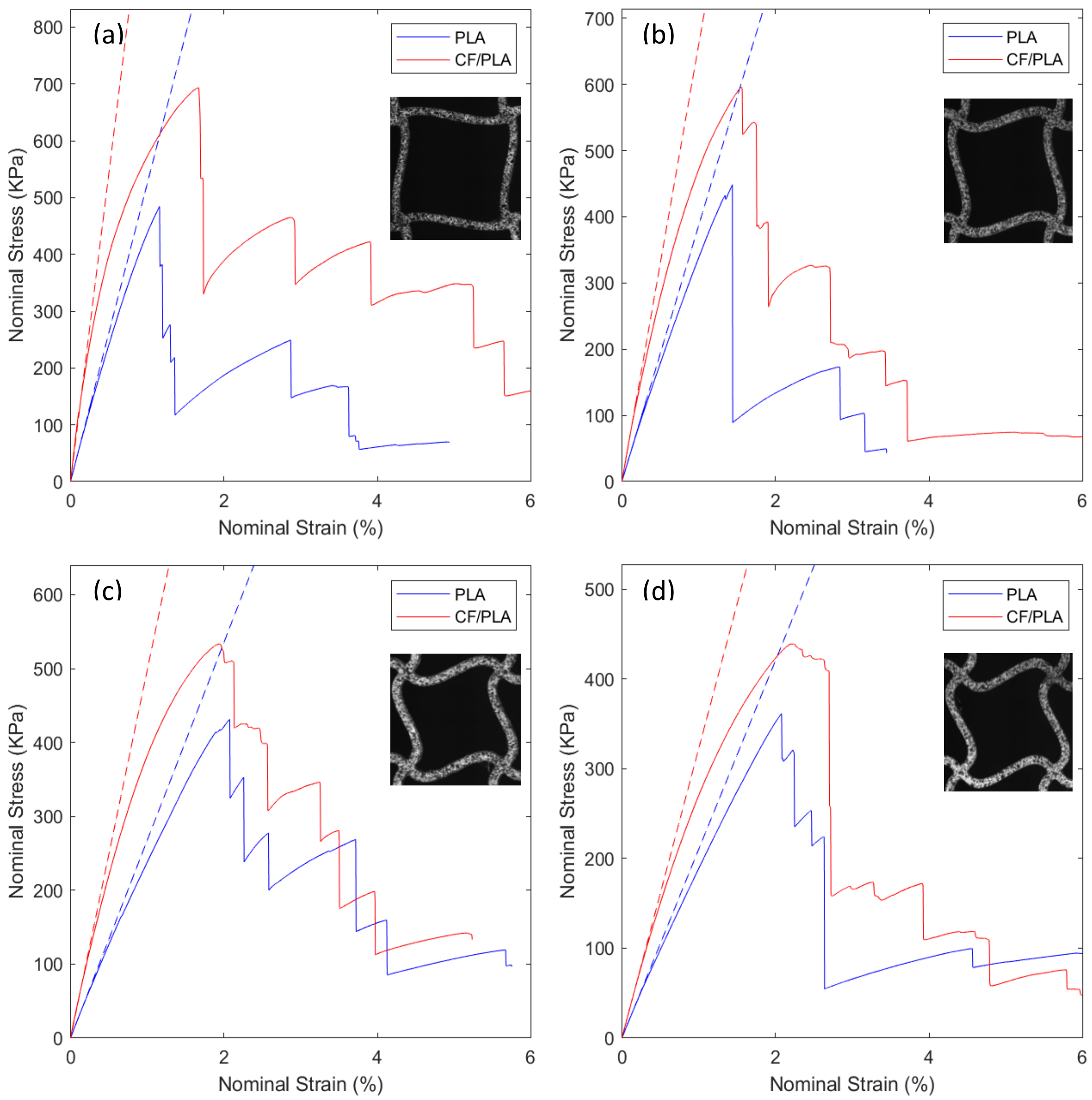

Figure 6.10 Stress-strain curves of 3D printed neat PLA and CF/PLA chiral composites at different polynomial orders: (a) n = 1.5; (b) n = 2; (c) n = 3; and (d) n = 4.

The layer-by-layer printing of FDM also had an additional impact on the zigzag trend of stress-strain curves. Due to the insufficient bonding between adjacent beads in the deposition process, voids were formed in 3D printed parts, leading to the corresponding inner defects as the crack initiation points [354]. The different locations of these porous defects generated the varying propagation paths of crack in these structures, which exhibited different zigzag tensile curves.

Besides, the incorporation of discontinuous CFs into the PLA created the internal voids in extruded beads, as shown in **Figure 6.11**. This inner-bead void defects caused by the weak interfacial bonding between fibers and polymer matrix can produce more stress concentrations as weak points inside the fabricated sample [184]. It to a certain extent, clarified the phenomenon in **Figure 6.10** that the chiral lattices printed by CF reinforced composites had more zigzag breaks in stress-strain curves than those neat PLA counterparts.

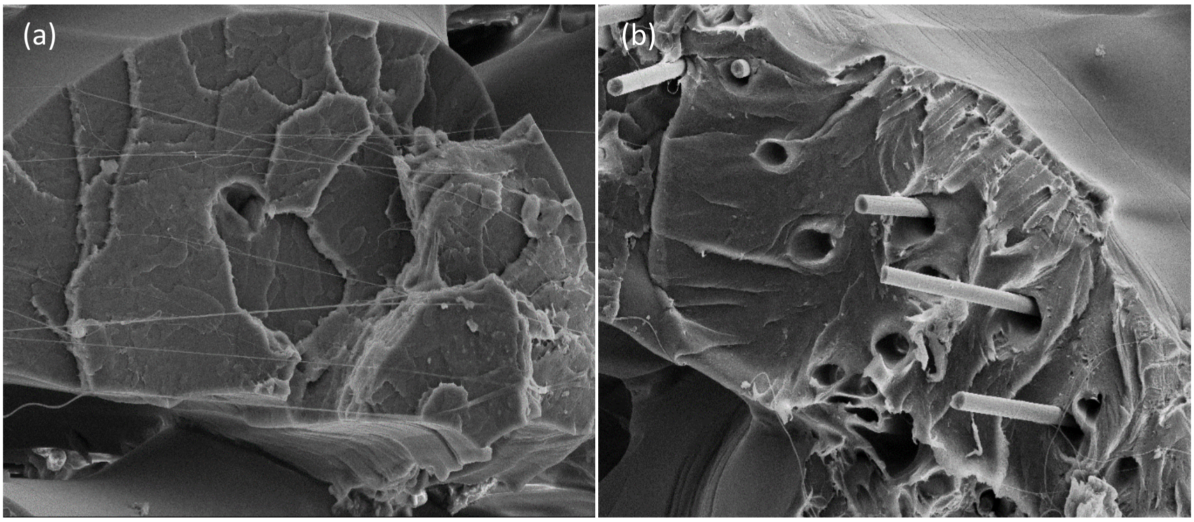

Figure 6.11 SEM images for fractural surfaces of (a) neat PLA and (b) CF/PLA composites at the × 1000 magnification.

3.5 The effect of CF on the tensile properties

With respect to chiral structures made from neat PLA, the tensile modulus decreased by 57.8% from 51 MPa to 21.5 MPa with the polynomial order rising from 1.5 to 4 (**Figure 6.12a**). This result can credit to the transition of lattice shapes from the stretch-dominated tension to bending-dominated one from the increase of *n* value. As a result, the increased curvature in designed structures facilitated the bending and rotation of chiral branches, leading to the decrease of the overall stiffness. Same trend was clearly observed in CF reinforced chiral composites at a reduction by 56.2% from 104.2 MPa to 45.6 MPa with the increase of branch curvature (note that the effective modulus was calculated by adopting the slope of the best fit straight line in the stress-strain curve). However, all the moduli of these fiber composites were > 2-fold higher than those from unreinforced counterparts. Without doubt, the high modulus and strength of CF as the additive endowed the PLA matrix with higher stiffness, thus enhancing the mechanical performance in these auxetic metamaterials [261]. Another reason for this high modulus improvement was the use of long chopped CF (~4.6 mm). Although the shear force existing in twin-screw extrusion and FDM printing could damage the length of some fibers, most of them may still maintain its critical length in final printed composites, which was vital to efficiently transfer the stress from the matrix to the fiber via shear transfer mechanism [262]. Likewise, both of neat PLA and CF/PLA composites showed a downward trend in tensile strength for higher polynomial orders with a drop by 17.4% and 10.7%, respectively. Meanwhile, with the introduction of CF, all the high performance fiber reinforced composites were > 30% stronger than the neat polymer samples with the same structure (**Figure 6.12b**).

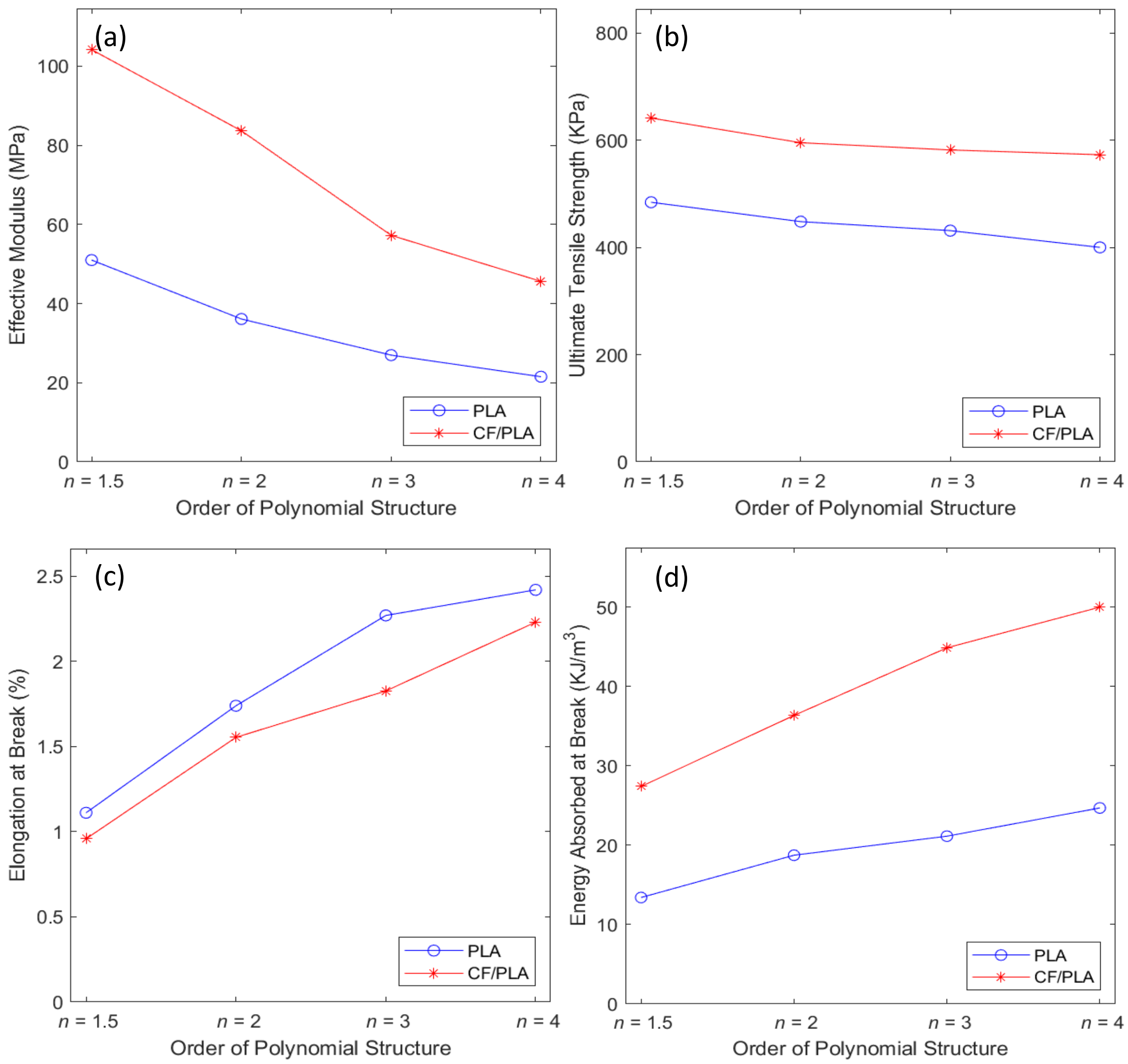

Figure 6.12 Tensile properties of 3D printed neat PLA and CF/PLA chiral composites with varying polynomial orders: (a) effective modulus; (b) ultimate tensile strength; (c) elongation at break; and (d) energy absorbed at break.

On the contrary, the elongation at break, representating the maximum displacement, decreased with the fiber loading since the high stiffness of CF can impair the ductility of PLA matrix. Nevertheless, for higher polynomial orders, the elongation values in both neat PLA and composites exhibited an upward trend with big increases by 118.0% and 132.3% (**Figure 6.12c**). To further understand the underlying mechanism, FEA was performed on the four variations of lattice structures to analyze the stress distributions within the material. As it can be seen in **Figure 6.13** regarding the contour map of the von Mises stress, regions with relatively high values of stress and deformation was found around the corners of branches in polynomial-derived chiral geometries. Highlighted by red color in the contour map, these areas in unit cell were highly stretched under the same strain. These red areas were gradually reduced to near zero when the *n* rose up to 4, demonstrating the corresponding shrinkage of concentrations in stress. It well explained why the larger elongation appeared at higher branch curvature for this designed lattice.

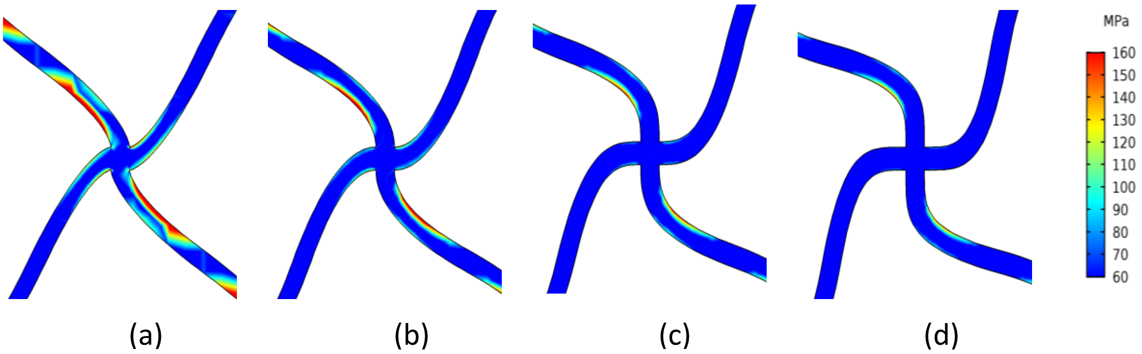

Figure 6.13 The von Mises stress distribution of unit cells in chiral structures with different polynomial orders: (a) n = 1.5; (b) n = 2; (c) n = 3; and (d) n = 4.

The energy required to break the structures was calculated by integrating the area under the force-deformation curve and presented in **Figure 6.12d**. Similar to the elongation at break, the energy absorption at break also increased with the rise of polynomial orders. The highest energy at *n* = 4 absorbed 84.3% and 82.5% more than those at *n* = 1.5 both in PLA and CF/PLA composites. Although the tensile stiffness and strength were decreased with the increase of *n* values, the big improvement in elongation within these competing tensile factors still contributed to the stable increase of absorbed energy at higher curvatures. Moreover, compared to neat PLA samples, around 2-fold energy inputs were needed to damage CF reinforced composites, indicating the great benefit to incorporate high performance fibers into the basic auxetic design so as to achieve better mechanical properties. On the other hand, by combining the von Mises stress analysis presented above, it also provided a remarkable potential to create stronger and tougher metamaterials via optimizing those stress concentration areas in these structures.

6.4 Conclusion

In summary, by combining structural design with additive manufacturing, we created a new class of chiral composites built upon the mathematical polynomial equation. Four typical geometries with the polynomial order ranging from 1.5 to 4 were chosen in this study due to their obvious difference in the variation of Poisson's ratios from the preliminary finite element modeling. Built upon the FDM technique, these chiral lattices were 3D printed into the corresponding polymer composites with chopped CF as the reinforcing filler. The deformation process of these structures changed from bending- to stretching-dominated mode because of the curved branches in unit cell. Auxetic behavior was observed both in neat PLA and CF/PLA chiral composites and the smallest Poisson's ratio appeared at the n =2. The experimental Poisson's ratios in both pure PLA and CF reinforced composites were slightly lower than the theoretical Poisson's ratios. This can be attributed to the inherent void defects existing in FDM printed parts. Due to the high stiffess and the structural heterogeneity induced by the addition of CF, the PLA composites also showed lower values in terms of experimental Poisson's ratios since it to a certain extent restricted the dimensional deformation during the tensile test. In addition, the incorporation of CF into the PLA matrix largely enhanced the tensile strength, modulus and energy absorption in the developed structure. This obvious improvement mainly originated from the high strength and stiffness of the fiber filler. This research opens a new avenue to the design and advanced fabrication of auxetic metamaterials with superior mechanical performance.

CHAPTER 7 CONCLUSIONS AND FUTURE WORK

7.1 Conclusions

In this thesis project, the fabrication of CF reinforced thermoplastic composites was studied by one of the most popular polymer manufacturing technique called HME. As the intermediate processing approach, two other strategies (e.g. IM and FDM) were coupled with HME so as to produce the final FRPCs. Of both, the thesis is more focused on the research of HME+FDM system due to its numerous advantages (e.g. high customization, full automation, minimum waste and high fabrication capacity for complex geometries) that impart great potential to replace many traditional manufacturig methods. The main contributions of this project to the body of knowledge on this research field are:

- *The fabrication and characterization of HDPE composites reinforced by CNT-coated CFs (based on HME+IM system).*
    - The morphological modification of CF was for the first time conducted by spray coating CNTs onto the surface of chopped CFs, which is a simple and encomomical coating treatment widely used in industry.
    - The CNT-coated CFs with varying contents were blended with HDPE matrix and fabricated into hierarchical composites by utilizing the twin-screw extrusion and IM techniques.
    - For CF/HDPE composites without CNT coating, the tensile strengh and modulus were increased by 70.62% and 70.59% with the rise of CF contents from 0 to 25 wt%. The flexural strength and modulus also showed an upward trend with the increasement of 40.38% and 47.51% compared to the neat HDPE sample.

- With the CNT coating onto CFs, both of tensile and flexural properties in CNT-CF/HDPE composites were improved relative to the uncoated counterparts. At 25 wt% CF content, the hardness of this hierarchical composite was 22.67% higher than the HDPE composite without CNT coating.
- The enhancement of overall mechanical performance can be ascribed to the high stiffness and strength of CF as well as the improved interfacial adhesion between CF and HDPE matrix, with the increased surface roughness of CFs from the SEM observation.
- The DSC result showed that both CF and CNT acted as heterogeneous nuclei and restriction sites to regulate the degree of crystallization in the fabricated CNT-CF/HDPE composites.

➢ *The fabrication of long CF reinroced PLA composites via FDM: experimental analysis and machine learning (based on HME+FDM system).*

- Further to nomally applied short CF with length ≤ 1 mm, long CF (~4.6 mm) was successfully introduced into the twin-screw extrusion for the continous composite filament fabrication, which was used as the feedstock for FDM.
- With the increase of CF loadings from 0 to 15 wt%, both of tensile strength and modulus in 3D printed CF/PLA composites exhibited an upward-downward-upward tendency, where the largest tensile strength increased by 89.14% at 5 wt% CF while the largest tensile modulus increased by 70.71% at 7.5 wt% CF.
- The flexural strength and modulus had the same trend with those of tensile properties but both of them rised up to the highest value at 15 wt%, with the enhancement by 43% and 185.29%. Besides, the highest hardness value (increased by 131.92%) appeared at 5 wt% CF/PLA samples.

- The addition of CF contributed to the biggest improvement of thermal conductivity in 5 wt% PLA composites because of the high thermal conductivity of CF and relatively low porosity.
- The variations of all these results can be explained by the compromising competition between the high performance of CF and inter-/intra-bead porosities observed from SEM images.
- The machine learning technique [355] was for the first time employed into the prediction for the mechanical properties of 3D printed composites, in which three convariance matrices from the combination of different kernel functions (RBF+Matern32, RBF+Polynomial and RBF+RBF) were constructed in the model and the optimal CF content for the best overall performance was predicted at 6.7 wt% within the range between 0-15 wt%.

➢ *3D printing of chiral CF reinforced PLA composites with negative Poisson's ratios (based on HME+FDM system).*

- A new class of chiral structures with the auxetic feature was designed by varying the order of *n* in the polynomial equation, in which *n* was set as 1.5, 2, 3 and 4.
- 3D printing was employed to fabricate the neat PLA and CF/PLA composites so as to experimentally investigate the influences of the polynomial orders and the addition of high performance fibers on the mechanical properties.
- The auxetic behavior of these chiral structures relied on the same deformation mechanism in which curved branches in the unit cell bended first and then stretched when the trangential direction of these bended branches was gradually in line with the loading direction, contributing to the expansion of all these chiral branches in *x* and *y* directions.

- The Poisson's ratios exhibited an upward-downward trend with the increase of polynomial orders with the largest value appeared at *n*=2.
- The tensile modulus and strength decreased with the increase of polynomial orders both in neat PLA and CF/PLA composite samples while all values in composites were higher than those without CF as the reinforment, especially for the modulus with over 200% improvement.
- The elongation and energy adsorption at break increased with the rise of polynomial orders both in neat PLA and CF/PLA composite samples, in which the adsorbed energy ar break in chiral composites was around 2-fold higher than that in neat PLA counterparts.
- FEA was also utilized to fully understand the mechanism underlying the auxetic deformation and mechanical performance as well as the preliminary modeling for the option of proper polynomial orders.

7.2 Future work

Although this thesis project has made some important contributions to the research on the fabrication of carbon fiber reinforced thermoplastic composites, future work into the following issues may be rewarding to promote the development in this exciting field:

1. The CNT-coated CF/HDPE composites have been demonstrated improved interfacial bonding between fiber and matrix through mechanical test and SEM observation. In order to further study the spray coating quality, the adhesion capacity between CNTs and fiber surface will be analyzed since it's vital to realize the maximum fiber/matrix bonding during HME and IM processes.

2. The CFs with CNT coating can also been employed into the composite filament fabrication in HME and the following FDM printing to investigate the effect of CNT coating on the interfacial bonding between CF and PLA. Since there are very few reports in this area, how to improve the adhesion between reinforcement and matrix will be crucial to eliminate the defect of inner-bead voids, thus enhancing the overall material properties.
3. Although we chose low rotation speed (25 rpm) to extrude CF/PLA composite filaments during the HME processes, the fiber length could still be decreased in the final printed composite part due to the existence of shear force in HME and FDM operations. In the future work, we can study the influences of processing parameters in HME+FDM system on the CF length and optimize these factors to maximize the fiber length in the final product.
4. With the view of fully integrating the ML technique into the research on the fabrication of CF reinforced composites via HME+FDM, more data needs to be collected from the experiments with the alteration of related parameters. It can create a more comprehensive correlation between the prediction for resultant performance of printed parts and the regulation of various influential factors.
5. Although the novel chiral structure based on polynomial curves was created in this project, the detailed theoretical model for this type of auxetic geometry is still missing, which will be very useful to quantitatively understand the internal mechanisms responsible for the auxetic and mechanical behaviors in this 2D lattice system under uniaxial tension.
6. Based on the von Mises stress analysis, regions with stress concentrations can be eliminated via the topological optimization so that higher mechanical performance can

be achieved in this chiral structure, which will be very promising to explore its application in load-bearing engineering fields.

APPENDIX

As a branch of artifical intelligence, ML was used as a theoretical tool to predict the optimal CF content (ranging from 0 to 15 wt%) in the FDM fabrication of PLA composites so as to achieve the best mechanical performance. The programming code employed in the ML process for the study in the chapter 5 was detailedly given as follows:

```
import pylab as pb
import GPy
import numpy as np
import matplotlib.pyplot as plt

pb.interactive(False)

"""Experiment Data"""
Title = ['Tensile strength', 'Tensile modulus', 'Elongation at break ',
        'Flexural strength', 'Flexural modulus ', 'Hardness (HRR)']
X = np.array([[0], [2.5], [5], [7.5], [10], [15]])
y = np.array([[23.66, 1.4, 2.82, 40.28, 1.02, 35.37], [31.66, 1.67, 3.16, 51.09, 1.75, 49.93],
            [44.75, 2.31, 3.23, 56.19, 1.81, 82.03], [39.86, 2.39, 2.77, 43.39, 1.99, 79.33],
            [24.65, 2.06, 1.96, 32.18, 1.19, 74.44], [26.88, 2.12, 1.68, 57.6, 2.91, 77.78]])

y0 = np.reshape(y[:,0], (6,1))
y1 = np.reshape(y[:,1], (6,1))
```

```
y2 = np.reshape(y[:,2], (6,1))

y3 = np.reshape(y[:,3], (6,1))

y4 = np.reshape(y[:,4], (6,1))

y5 = np.reshape(y[:,5], (6,1))

yy = [y0, y1, y2, y3, y4, y5]


error = np.array([[1.11, 0.04, 0.22, 2.75, 0.22, 2.13], [2.67, 0.09, 0.23, 5.41, 0.4, 4.55],

                 [2.4, 0.16, 0.29, 4.93, 0.23, 6.31], [2.01, 0.12, 0.15, 3.02, 0.25, 8.34],

                [2.68, 0.18, 0.06, 4.48, 0.17, 9.52], [1.39, 0.07, 0.05, 3.81, 0.26, 10.11]])


"""Establish Kernel"""

K1 = GPy.kern.Bias(1)

K2 = GPy.kern.RBF(1, 2.04, 2.5)

K3 = GPy.kern.Matern32(1)

# K2 = GPy.kern.RBF(1,0.11,2.5)

# K3 = GPy.kern.Matern32(1,0.11,2.5)

# m['.*ICM0.*var'].constrain_fixed(1.)

# m['.*ICM0.*W'].constrain_fixed(0)

# m['.*ICM1.*var'].constrain_fixed(1.)

# m['.*ICM1.*W'].constrain_fixed(0)


"""Establish GPy and traing"""

lcm = GPy.util.multioutput.LCM(input_dim=1, num_outputs=6, kernels_list=[K2, K3])

m = GPy.models.GPCoregionalizedRegression([X, X, X, X, X, X], [y0, y1, y2, y3, y4, y5],

kernel=lcm)
```

```
m.optimize()

print(m)


"""Plot the output"""

def plot_2outputs(m,xlim,ylim, num_outputs):

    fig = pb.figure(figsize=(8,20))

    #Output 1

    for i in range(num_outputs):

        ax1 = fig.add_subplot(num_outputs,1,i+1)

        ax1.set_xlim(xlim)

        ax1.set_title(Title[i])


m.plot(plot_limits=xlim,fixed_inputs=[(1,i)],which_data_rows=slice(100,200),ax=ax1)

        ax1.plot(X,yy[i],'bx',mew=2)

    pb.show()




"""Single Output"""

f = GPy.models.GPRegression(X,y1,K2)

f.optimize()

print(f)

plot_2outputs(f, xlim=(-0.1,20),ylim=(20,60), num_outputs = 6)


i = 1

f = GPy.models.GPRegression(X,yy[i],K2)
```

```
f.optimize(messages=True)


fig = pb.figure(figsize=(20,8))

ax1 = fig.add_subplot(111)

ax1.set_xlim((0,20))

ax1.set_title(Title[i])

f.plot(plot_limits=(0 ,20), which_data_rows=slice(100,200),ax=ax1)

ax1.plot(X, yy[i], 'bx', mew=2)

pb.show()
```

REFERENCES

[1] R.F. Gibson, A review of recent research on mechanics of multifunctional composite materials and structures, Composite structures, 92(12) (2010) 2793-2810.

[2] V. Mittal, R. Saini, S. Sinha, Natural fiber-mediated epoxy composites–a review, Composites Part B: Engineering, 99 (2016) 425-435.

[3] X.-Q. Feng, Y.-W. Mai, Q.H. Qin, A micromechanical model for interpenetrating multiphase composites, Computational Materials Science, 28(3) (2003) 486-493.

[4] Q.H. Qin, J. Ye, Toughening mechanisms in composite materials, in, Elsevier, UK, 2015.

[5] Q.H. Qin, Q.S. Yang, Macro-micro theory on multifield coupling behaivor of hetereogenous materials, in, Higher Education Press and Springer, Beijing, 2008.

[6] G.M. Velez-Garcia, Experimental evaluation and simulations of fiber orientation in injection molding of polymers containing short glass fibers, Virginia Tech, 2012.

[7] R.F. Gibson, Principles of composite material mechanics, CRC press, 2016.

[8] M. Boopalan, M. Niranjanaa, M. Umapathy, Study on the mechanical properties and thermal properties of jute and banana fiber reinforced epoxy hybrid composites, Composites Part B: Engineering, 51 (2013) 54-57.

[9] C. Hu, X. Liao, Q.H. Qin, G. Wang, The fabrication and characterization of high density polyethylene composites reinforced by carbon nanotube coated carbon fibers, Composites Part A: Applied Science and Manufacturing, 121 (2019) 149-156.

[10] P. Parandoush, L. Tucker, C. Zhou, D. Lin, Laser assisted additive manufacturing of continuous fiber reinforced thermoplastic composites, Materials & Design, 131 (2017) 186-195.

[11] L. Zhang, X. Wang, J. Pei, Y. Zhou, Review of automated fibre placement and its prospects for advanced composites, Journal of Materials Science, (2020) 1-35.

[12] C. Hu, X. Liao, Q.H. Qin, G. Wang, The Fabrication of Hierarchical Carbon Nanotube/carbon fibre/polyethylene Composites via Twin Screw Extruder, in: MATEC Web of Conferences, EDP Sciences, 2018, pp. 01006.

[13] R.L. Truby, J.A. Lewis, Printing soft matter in three dimensions, Nature, 540(7633) (2016) 371-378.

[14] R. Jiang, R. Kleer, F.T. Piller, Predicting the future of additive manufacturing: A Delphi study on economic and societal implications of 3D printing for 2030, Technological Forecasting and Social Change, 117 (2017) 84-97.

[15] S.H. Huang, P. Liu, A. Mokasdar, L. Hou, Additive manufacturing and its societal impact: a literature review, The International Journal of Advanced Manufacturing Technology, 67(5-8) (2013) 1191-1203.

[16] Y. Qin, Q. Qi, P.J. Scott, X. Jiang, Status, comparison, and future of the representations of additive manufacturing data, Computer-Aided Design, 111 (2019) 44-64.

[17] C.M. González-Henríquez, M.A. Sarabia-Vallejos, J. Rodriguez-Hernandez, Polymers for additive manufacturing and 4D-printing: Materials, methodologies, and biomedical applications, Progress in Polymer Science, (2019).

[18] M. Attaran, The rise of 3-D printing: The advantages of additive manufacturing over traditional manufacturing, Business Horizons, 60(5) (2017) 677-688.

[19] B. Sedacca, Hand built by lasers [additive layer manufacturing], Engineering & Technology, 6(1) (2011) 58-60.

[20] V. Dikshit, A.P. Nagalingam, Y.L. Yap, S.L. Sing, W.Y. Yeong, J. Wei, Investigation of quasi-static indentation response of inkjet printed sandwich structures under various indenter geometries, Materials, 10(3) (2017) 290.

[21] B. Berman, 3-D printing: The new industrial revolution, Business horizons, 55(2) (2012) 155-162.
[22] A. Bandyopadhyay, B. Heer, Additive manufacturing of multi-material structures, Materials Science and Engineering: R: Reports, 129 (2018) 1-16.
[23] C.W. Hull, Apparatus for production of three-dimensional objects by stereolithography, United States Patent, Appl., No. 638905, Filed, (1984).
[24] A. Standard, Standard terminology for additive manufacturing technologies, ASTM International F2792-12a, (2012).
[25] S.C. Ligon, R. Liska, J.r. Stampfl, M. Gurr, R. Mülhaupt, Polymers for 3D printing and customized additive manufacturing, Chemical reviews, 117(15) (2017) 10212-10290.
[26] J.W. Stansbury, M.J. Idacavage, 3D printing with polymers: Challenges among expanding options and opportunities, Dental Materials, 32(1) (2016) 54-64.
[27] E. MacDonald, R. Wicker, Multiprocess 3D printing for increasing component functionality, Science, 353(6307) (2016) aaf2093.
[28] N. Saengchairat, T. Tran, C.-K. Chua, A review: Additive manufacturing for active electronic components, Virtual and Physical Prototyping, 12(1) (2017) 31-46.
[29] S. Bose, D. Ke, H. Sahasrabudhe, A. Bandyopadhyay, Additive manufacturing of biomaterials, Progress in materials science, 93 (2018) 45-111.
[30] S. Lim, R.A. Buswell, T.T. Le, S.A. Austin, A.G. Gibb, T. Thorpe, Developments in construction-scale additive manufacturing processes, Automation in construction, 21 (2012) 262-268.
[31] N. Guo, M.C. Leu, Additive manufacturing: technology, applications and research needs, Frontiers of Mechanical Engineering, 8(3) (2013) 215-243.
[32] H. Smith, GE aviation to grow better fuel nozzles using 3D printing, 3D Printing News and Trends, 17 (2013).
[33] J. Manyika, M. Chui, J. Bughin, R. Dobbs, P. Bisson, A. Marrs, Disruptive technologies: Advances that will transform life, business, and the global economy, McKinsey Global Institute San Francisco, CA, 2013.
[34] P. Parandoush, D. Lin, A review on additive manufacturing of polymer-fiber composites, Composite Structures, 182 (2017) 36-53.
[35] T.D. Ngo, A. Kashani, G. Imbalzano, K.T. Nguyen, D. Hui, Additive manufacturing (3D printing): A review of materials, methods, applications and challenges, Composites Part B: Engineering, 143 (2018) 172-196.
[36] M. Araya-Calvo, I. López-Gómez, N. Chamberlain-Simon, J.L. León-Salazar, T. Guillén-Girón, J.S. Corrales-Cordero, O. Sánchez-Brenes, Evaluation of compressive and flexural properties of continuous fiber fabrication additive manufacturing technology, Additive Manufacturing, 22 (2018) 157-164.
[37] B. Akhoundi, A.H. Behravesh, A. Bagheri Saed, Improving mechanical properties of continuous fiber-reinforced thermoplastic composites produced by FDM 3D printer, Journal of Reinforced Plastics and Composites, 38(3) (2019) 99-116.
[38] C. Kousiatza, D. Tzetzis, D. Karalekas, In-situ characterization of 3D printed continuous fiber reinforced composites: A methodological study using fiber Bragg grating sensors, Composites Science and Technology, 174 (2019) 134-141.
[39] R. Matsuzaki, T. Nakamura, K. Sugiyama, M. Ueda, A. Todoroki, Y. Hirano, Y. Yamagata, Effects of set curvature and fiber bundle size on the printed radius of curvature by a continuous carbon fiber composite 3D printer, Additive Manufacturing, 24 (2018) 93-102.
[40] R. Matsuzaki, M. Ueda, M. Namiki, T.-K. Jeong, H. Asahara, K. Horiguchi, T. Nakamura, A. Todoroki, Y. Hirano, Three-dimensional printing of continuous-fiber composites by in-nozzle impregnation, Scientific reports, 6 (2016) 23058.

[41] G.T. Mark, A.S. Gozdz, Apparatus for fiber reinforced additive manufacturing, in, Google Patents, 2017.
[42] C. Hu, Z. Sun, Y. Xiao, Q.H. Qin, Recent patents in additive manufacturing of continuous fiber reinforced composites, Recent Patents on Mechanical Engineering, 12(1) (2019) 25-36.
[43] A.N. Dickson, J.N. Barry, K.A. McDonnell, D.P. Dowling, Fabrication of continuous carbon, glass and Kevlar fibre reinforced polymer composites using additive manufacturing, Additive Manufacturing, 16 (2017) 146-152.
[44] J. Vera-Sorroche, A. Kelly, E. Brown, P. Coates, N. Karnachi, E. Harkin-Jones, K. Li, J. Deng, Thermal optimisation of polymer extrusion using in-process monitoring techniques, Applied Thermal Engineering, 53(2) (2013) 405-413.
[45] C. Abeykoon, Single screw extrusion control: A comprehensive review and directions for improvements, Control Engineering Practice, 51 (2016) 69-80.
[46] B. Claeys, A. Vervaeck, X.K. Hillewaere, S. Possemiers, L. Hansen, T. De Beer, J.P. Remon, C. Vervaet, Thermoplastic polyurethanes for the manufacturing of highly dosed oral sustained release matrices via hot melt extrusion and injection molding, European Journal of Pharmaceutics and Biopharmaceutics, 90 (2015) 44-52.
[47] M.A. Repka, S. Shah, J. Lu, S. Maddineni, J. Morott, K. Patwardhan, N.N. Mohammed, Melt extrusion: process to product, Expert opinion on drug delivery, 9(1) (2012) 105-125.
[48] E.J. Siochi, D.C. Working, C. Park, P.T. Lillehei, J.H. Rouse, C.C. Topping, A.R. Bhattacharyya, S. Kumar, Melt processing of SWCNT-polyimide nanocomposite fibers, Composites Part B: Engineering, 35(5) (2004) 439-446.
[49] M. Sauceau, J. Fages, A. Common, C. Nikitine, E. Rodier, New challenges in polymer foaming: A review of extrusion processes assisted by supercritical carbon dioxide, Progress in Polymer Science, 36(6) (2011) 749-766.
[50] Y.-L. Kang, Z.-F. Zhang, H.-W. Wang, Q.H. Qin, Experimental investigations of the effect of thickness on fracture toughness of metallic foils, Materials Science and Engineering: A, 394(1) (2005) 312-319.
[51] Q.H. Qin, Hybrid Trefftz finite-element approach for plate bending on an elastic foundation, Applied Mathematical Modelling, 18(6) (1994) 334-339.
[52] Q.H. Qin, Hybrid-Trefftz finite element method for Reissner plates on an elastic foundation, Computer Methods in Applied Mechanics and Engineering, 122(3-4) (1995) 379-392.
[53] Q.H. Qin, Fundamental Solution Based Finite Element Method, J Appl Mech Eng, 2 (2013) e118.
[54] Y.-T. Gao, H. Wang, Q.H. Qin, Orthotropic Seepage Analysis using Hybrid Finite Element Method, Journal of Advanced Mechanical Engineering, 2(1) (2015) 1-13.
[55] Q.H. Qin, Trefftz plane elements of elastoplasticity with p-extension capabilities, Journal of Mechanical Engineering, 56(1) (2005) 40-59.
[56] H. Wang, Q.H. Qin, FE approach with Green's function as internal trial function for simulating bioheat transfer in the human eye, Archives of Mechanics, 62(6) (2010) 493-510.
[57] M. Dhanasekar, J. Han, Q.H. Qin, A hybrid-Trefftz element containing an elliptic hole, Finite Elements in Analysis and Design, 42(14) (2006) 1314-1323.
[58] C. Abeykoon, Polymer extrusion: A study on thermal monitoring techniques and melting issues, Lap Lambert Academic Publishing, 2012.
[59] C. Rauwendaal, Polymer extrusion, Carl Hanser Verlag GmbH Co KG, 2014.
[60] C. Ajinjeru, V. Kishore, Z. Sudbury, J. Lindahl, A. Hassen, B. Post, L. Love, V. Kunc, C. Duty, The Influence of Rheology on Melt Processing Conditions of Carbon Fiber

Reinforced Polyetherimide for Big Area Additive Manufacturing (BAAM), in: SAMPE Conference Proceedings. Seattle WA, 2017.
[61] B. Brenken, E. Barocio, A. Favaloro, V. Kunc, R.B. Pipes, Development and validation of extrusion deposition additive manufacturing process simulations, Additive Manufacturing, 25 (2019) 218-226.
[62] C. Hu, Q.H. Qin, Advances in fused deposition modeling of discontinuous fiber/polymer composites, Current Opinion in Solid State and Materials Science, 24(5) (2020) 100867.
[63] I. Aydin, F. Biglari, B. Briscoe, C. Lawrence, M. Adams, Physical and numerical modelling of ram extrusion of paste materials: conical die entry case, Computational Materials Science, 18(2) (2000) 141-155.
[64] H. Patil, R.V. Tiwari, M.A. Repka, Hot-melt extrusion: from theory to application in pharmaceutical formulation, Aaps Pharmscitech, 17(1) (2016) 20-42.
[65] A. Gaspar-Cunha, J.A. Covas, M.F.P. Costa, L. Costa, Optimization of single screw extrusion, (2018).
[66] S. Singhal, V.K. Lohar, V. Arora, Hot melt extrusion technique, (2011).
[67] R. Chokshi, H. Zia, Hot-melt extrusion technique: a review, (2004).
[68] M. Maniruzzaman, J.S. Boateng, M.J. Snowden, D. Douroumis, A review of hot-melt extrusion: process technology to pharmaceutical products, ISRN pharmaceutics, 2012 (2012).
[69] R. Censi, M.R. Gigliobianco, C. Casadidio, P. Di Martino, Hot melt extrusion: Highlighting physicochemical factors to be investigated while designing and optimizing a hot melt extrusion process, Pharmaceutics, 10(3) (2018) 89.
[70] M. Gale, Mixing in single screw extrusion, ISmithers, 2009.
[71] K. Wilczyński, A. Lewandowski, A. Nastaj, K. Wilczyński, Modeling for Starve Fed/Flood Fed Mixing Single-Screw Extruders, International Polymer Processing, 31(1) (2016) 82-91.
[72] M.A. Repka, N. Langley, J. DiNunzio, Melt extrusion: materials, technology and drug product design, Springer Science & Business Media, 2013.
[73] K. Wilczyński, A. Nastaj, K. Wilczyński, Melting Model for Starve Fed Single Screw Extrusion of Thermoplastics, International Polymer Processing, 28(1) (2013) 34-42.
[74] K. Wilczyński, A. Lewandowski, K.J. Wilczyński, Experimental study for starve-fed single screw extrusion of thermoplastics, Polymer Engineering & Science, 52(6) (2012) 1258-1270.
[75] D.K. Tan, M. Maniruzzaman, A. Nokhodchi, Advanced pharmaceutical applications of hot-melt extrusion coupled with fused deposition modelling (FDM) 3D printing for personalised drug delivery, Pharmaceutics, 10(4) (2018) 203.
[76] K. Wilczynski, J.L. White, Melting model for intermeshing counter-rotating twin-screw extruders, Polymer Engineering & Science, 43(10) (2003) 1715-1726.
[77] J.-M. Bouvier, O.H. Campanella, Extrusion processing technology: food and non-food biomaterials, John Wiley & Sons, 2014.
[78] Z. Tadmor, C.G. Gogos, Principles of polymer processing, John Wiley & Sons, 2013.
[79] M.M. Crowley, F. Zhang, M.A. Repka, S. Thumma, S.B. Upadhye, S. Kumar Battu, J.W. McGinity, C. Martin, Pharmaceutical applications of hot-melt extrusion: part I, Drug development and industrial pharmacy, 33(9) (2007) 909-926.
[80] M. Wilson, M.A. Williams, D.S. Jones, G.P. Andrews, Hot-melt extrusion technology and pharmaceutical application, Therapeutic delivery, 3(6) (2012) 787-797.
[81] W. Thiele, Twin-Screw Extrusion and Screw Design, in: Pharmaceutical Extrusion Technology, CRC Press, 2018, pp. 71-94.

[82] D.E. Crawford, Extrusion–back to the future: Using an established technique to reform automated chemical synthesis, Beilstein journal of organic chemistry, 13(1) (2017) 65-75.
[83] E. Uitterhaegen, Q.H. Nguyen, K. Sampaio, C. Stevens, O. Merah, T. Talou, L. Rigal, P. Evon, Extraction of coriander oil using twin-screw extrusion: Feasibility study and potential press cake applications, Journal of the American Oil Chemists' Society, 92(8) (2015) 1219-1233.
[84] J. Thiry, F. Krier, B. Evrard, A review of pharmaceutical extrusion: Critical process parameters and scaling-up, International journal of pharmaceutics, 479(1) (2015) 227-240.
[85] H.F. Giles Jr, E.M. Mount III, J.R. Wagner Jr, Extrusion: the definitive processing guide and handbook, William Andrew, 2004.
[86] J.M. Keen, C. Martin, A. Machado, H. Sandhu, J.W. McGinity, J.C. DiNunzio, Investigation of process temperature and screw speed on properties of a pharmaceutical solid dispersion using corotating and counter-rotating twin-screw extruders, Journal of Pharmacy and Pharmacology, 66(2) (2014) 204-217.
[87] M.R. Kamal, A.I. Isayev, Injection molding: Technology and fundamentals, Carl Hanser Verlag GmbH Co KG, 2012.
[88] C. Fernandes, A.J. Pontes, J.C. Viana, A. Gaspar-Cunha, Modeling and Optimization of the Injection-Molding Process: A Review, Advances in Polymer Technology, 37(2) (2018) 429-449.
[89] L. Zema, G. Loreti, A. Melocchi, A. Maroni, A. Gazzaniga, Injection molding and its application to drug delivery, Journal of controlled release, 159(3) (2012) 324-331.
[90] B.B. Kanbur, S. Suping, F. Duan, Design and optimization of conformal cooling channels for injection molding: a review, The International Journal of Advanced Manufacturing Technology, 106(7-8) (2020) 3253-3271.
[91] J.M. Park, S.J. Park, Modeling and simulation of fiber orientation in injection molding of polymer composites, Mathematical Problems in Engineering, 2011 (2011).
[92] M.S. Shinde, K.M. Ashtankar, A.M. Kuthe, S.W. Dahake, M.B. Mawale, Direct rapid manufacturing of molds with conformal cooling channels, Rapid Prototyping Journal, (2018).
[93] D.V. Rosato, M.G. Rosato, Injection molding handbook, Springer Science & Business Media, 2012.
[94] M. Spoerk, C. Savandaiah, F. Arbeiter, J. Sapkota, C. Holzer, Optimization of mechanical properties of glass-spheres-filled polypropylene composites for extrusion-based additive manufacturing, Polymer Composites, 40(2) (2019) 638-651.
[95] A. Khudiakova, F. Arbeiter, M. Spoerk, M. Wolfahrt, D. Godec, G. Pinter, Inter-layer bonding characterisation between materials with different degrees of stiffness processed by fused filament fabrication, Additive Manufacturing, 28 (2019) 184-193.
[96] F. Arbeiter, M. Spoerk, J. Wiener, A. Gosch, G. Pinter, Fracture mechanical characterization and lifetime estimation of near-homogeneous components produced by fused filament fabrication, Polymer Testing, 66 (2018) 105-113.
[97] C. Hu, Q.H. Qin, W.N.J. Hau, H. zhou, The twin-screw extrusion of long carbon fibre reinforced polylactic acid filaments for 3D printing, in, 2020.
[98] M.M. Denn, Extrusion instabilities and wall slip, Annual Review of Fluid Mechanics, 33(1) (2001) 265-287.
[99] S.S. Crump, Apparatus and method for creating three-dimensional objects, in, Google Patents, 1992.

[100] B.N. Turner, S.A. Gold, A review of melt extrusion additive manufacturing processes: II. Materials, dimensional accuracy, and surface roughness, Rapid Prototyping Journal, (2015).
[101] N. van de Werken, H. Tekinalp, P. Khanbolouki, S. Ozcan, A. Williams, M. Tehrani, Additively manufactured carbon fiber-reinforced composites: State of the art and perspective, Additive Manufacturing, 31 (2020) 100962.
[102] M.K. Agarwala, V.R. Jamalabad, N.A. Langrana, A. Safari, P.J. Whalen, S.C. Danforth, Structural quality of parts processed by fused deposition, Rapid prototyping journal, (1996).
[103] J.M. Nasereddin, N. Wellner, M. Alhijjaj, P. Belton, S. Qi, Development of a simple mechanical screening method for predicting the feedability of a pharmaceutical FDM 3D printing filament, Pharmaceutical research, 35(8) (2018) 151.
[104] A. Szmidt, A. Rębosz-Kurdek, New approaches of improving FDM/FFF printing technology, Mechanik, 90(3) (2017) 258-261.
[105] V.E. Kuznetsov, A.N. Solonin, O.D. Urzhumtsev, R. Schilling, A.G. Tavitov, Strength of PLA components fabricated with fused deposition technology using a desktop 3D printer as a function of geometrical parameters of the process, Polymers, 10(3) (2018) 313.
[106] T.N.A.T. Rahim, A.M. Abdullah, H. Md Akil, Recent developments in fused deposition modeling-based 3D printing of polymers and their composites, Polymer Reviews, 59(4) (2019) 589-624.
[107] C. Kim, D. Espalin, A. Cuaron, M.A. Perez, E. MacDonald, R.B. Wicker, A study to detect a material deposition status in fused deposition modeling technology, in: 2015 IEEE International Conference on Advanced Intelligent Mechatronics (AIM), IEEE, 2015, pp. 779-783.
[108] B.P. Heller, Effects of nozzle geometry and extrudate swell on fiber orientation in Fused Deposition Modeling nozzle flow, 2015.
[109] Y. Tlegenov, Y. San Wong, G.S. Hong, A dynamic model for nozzle clog monitoring in fused deposition modelling, Rapid Prototyping Journal, (2017).
[110] H. Wu, Z. Yu, Y. Wang, Real-time FDM machine condition monitoring and diagnosis based on acoustic emission and hidden semi-Markov model, The International Journal of Advanced Manufacturing Technology, 90(5-8) (2017) 2027-2036.
[111] Z. Yang, L. Jin, Y. Yan, Y. Mei, Filament breakage monitoring in fused deposition modeling using acoustic emission technique, Sensors, 18(3) (2018) 749.
[112] J. Go, S.N. Schiffres, A.G. Stevens, A.J. Hart, Rate limits of additive manufacturing by fused filament fabrication and guidelines for high-throughput system design, Additive Manufacturing, 16 (2017) 1-11.
[113] J. Go, A.J. Hart, Fast desktop-scale extrusion additive manufacturing, Additive Manufacturing, 18 (2017) 276-284.
[114] P. Kulkarni, A. Marsan, D. Dutta, A review of process planning techniques in layered manufacturing, Rapid prototyping journal, (2000).
[115] F. Alabdullah, Fused deposition modeling (FDM) mechanism, Int. J. Sci. Eng. Res, 7(5) (2016).
[116] B.N. Turner, R. Strong, S.A. Gold, A review of melt extrusion additive manufacturing processes: I. Process design and modeling, Rapid Prototyping Journal, (2014).
[117] S.-U. Zhang, J. Han, H.-W. Kang, Temperature-dependent mechanical properties of ABS parts fabricated by fused deposition modeling and vapor smoothing, International Journal of Precision Engineering and Manufacturing, 18(5) (2017) 763-769.

[118] R. Jerez-Mesa, G. Gomez-Gras, J.A. Travieso-Rodriguez, V. Garcia-Plana, A comparative study of the thermal behavior of three different 3D printer liquefiers, Mechatronics, 56 (2018) 297-305.
[119] A. Lanzotti, D.M. Del Giudice, A. Lepore, G. Staiano, M. Martorelli, On the geometric accuracy of RepRap open-source three-dimensional printer, Journal of Mechanical Design, 137(10) (2015).
[120] L. Brouwers, A. Teutelink, F.A. van Tilborg, M.A. de Jongh, K.W. Lansink, M. Bemelman, Validation study of 3D-printed anatomical models using 2 PLA printers for preoperative planning in trauma surgery, a human cadaver study, European Journal of Trauma and Emergency Surgery, 45(6) (2019) 1013-1020.
[121] P. Chesser, B.K. Post, R. Lind, P. Lloyd, L.J. Love, Changing Print Resolution on BAAM Via Selectable Nozzles, in: Solid Freeform Fabrication Symposium, 2017.
[122] E.A. Papon, A. HAQUE, R.S. MA, Effect of nozzle geometry on melt flow simulation and structural property of thermoplastic nanocomposites in fused deposition modeling, in: Proc. American society for composites, Thirty-second technical conference, 2017.
[123] H. Bikas, P. Stavropoulos, G. Chryssolouris, Additive manufacturing methods and modelling approaches: a critical review, The International Journal of Advanced Manufacturing Technology, 83(1-4) (2016) 389-405.
[124] A. Pandey, S.K. Pradhan, Investigations into complete liquefier dynamics and optimization of process parameters for fused deposition modeling, Materials Today: Proceedings, 5(5) (2018) 12940-12955.
[125] O. Günel, E. Koc, G. Tiryaki, Investigation of Heat Sink Geometry Effect on Cooling Performance for a FDM 3D Printer Liquefier, (2017).
[126] A. Bellini, S.u. Gu¨ c¸ eri, M. Bertoldi, Liquefier dynamics in fused deposition, J. Manuf. Sci. Eng., 126(2) (2004) 237-246.
[127] H. Ramanath, C. Chua, K. Leong, K. Shah, Melt flow behaviour of poly-ε-caprolactone in fused deposition modelling, Journal of Materials Science: Materials in Medicine, 19(7) (2008) 2541-2550.
[128] M. AtifYardimci, T. Hattori, S.I. Guceri, S.C. Danforth, Thermal analysis of fused deposition, in: 1997 International Solid Freeform Fabrication Symposium, 1997.
[129] R. Jerez-Mesa, J.A. Travieso-Rodriguez, X. Corbella, R. Busqué, G. Gómez-Gras, Finite element analysis of the thermal behavior of a RepRap 3D printer liquefier, Mechatronics, 36 (2016) 119-126.
[130] J. Nixon, B. Dryer, I. Lempert, D. Bigio, Three parameter analysis of fiber orientation in fused deposition modeling geometries, in: Proc. of PPS conference, 2014.
[131] B.P. Heller, D.E. Smith, D.A. Jack, Effects of extrudate swell and nozzle geometry on fiber orientation in Fused Filament Fabrication nozzle flow, Additive Manufacturing, 12 (2016) 252-264.
[132] J.R. Raney, B.G. Compton, J. Mueller, T.J. Ober, K. Shea, J.A. Lewis, Rotational 3D printing of damage-tolerant composites with programmable mechanics, Proceedings of the National Academy of Sciences, 115(6) (2018) 1198-1203.
[133] B. Brenken, E. Barocio, A. Favaloro, V. Kunc, R.B. Pipes, Fused filament fabrication of fiber-reinforced polymers: A review, Additive Manufacturing, 21 (2018) 1-16.
[134] D. Pollard, C. Ward, G. Herrmann, J. Etches, Filament temperature dynamics in fused deposition modelling and outlook for control, Procedia Manufacturing, 11 (2017) 536-544.
[135] J.E. Seppala, S.H. Han, K.E. Hillgartner, C.S. Davis, K.B. Migler, Weld formation during material extrusion additive manufacturing, Soft Matter, 13(38) (2017) 6761-6769.

[136] D.A. Anderegg, H.A. Bryant, D.C. Ruffin, S.M. Skrip Jr, J.J. Fallon, E.L. Gilmer, M.J. Bortner, In-situ monitoring of polymer flow temperature and pressure in extrusion based additive manufacturing, Additive Manufacturing, 26 (2019) 76-83.
[137] G. Goh, Y. Yap, H. Tan, S. Sing, G. Goh, W. Yeong, Process–structure–properties in polymer additive manufacturing via material extrusion: A review, Critical Reviews in Solid State and Materials Sciences, 45(2) (2020) 113-133.
[138] C. Bellehumeur, M. Bisaria, J. Vlachopoulos, An experimental study and model assessment of polymer sintering, Polymer Engineering & Science, 36(17) (1996) 2198-2207.
[139] O. Pokluda, C.T. Bellehumeur, J. Vlachopoulos, Modification of Frenkel's model for sintering, AIChE journal, 43(12) (1997) 3253-3256.
[140] P.K. Gurrala, S.P. Regalla, Part strength evolution with bonding between filaments in fused deposition modelling: This paper studies how coalescence of filaments contributes to the strength of final FDM part, Virtual and Physical Prototyping, 9(3) (2014) 141-149.
[141] Q. Sun, G. Rizvi, C. Bellehumeur, P. Gu, Effect of processing conditions on the bonding quality of FDM polymer filaments, Rapid Prototyping Journal, (2008).
[142] C. Bellehumeur, L. Li, Q. Sun, P. Gu, Modeling of bond formation between polymer filaments in the fused deposition modeling process, Journal of Manufacturing Processes, 6(2) (2004) 170-178.
[143] D. Bhalodi, K. Zalavadiya, P.K. Gurrala, Influence of temperature on polymer parts manufactured by fused deposition modeling process, Journal of the Brazilian Society of Mechanical Sciences and Engineering, 41(3) (2019) 113.
[144] L. Li, Q. Sun, C. Bellehumeur, P. Gu, Investigation of bond formation in FDM process, Solid Freeform Fabrication Proceedings,(403), 400407 (2002).
[145] A. Bellini, S. Güçeri, Mechanical characterization of parts fabricated using fused deposition modeling, Rapid Prototyping Journal, (2003).
[146] J. Thomas, J. Rodríguez, Modeling the Fracture Strength between Fused-Deposition Extruded Roads 16, in: 2000 International Solid Freeform Fabrication Symposium, 2000.
[147] M. Domingo-Espin, J.M. Puigoriol-Forcada, A.-A. Garcia-Granada, J. Llumà, S. Borros, G. Reyes, Mechanical property characterization and simulation of fused deposition modeling Polycarbonate parts, Materials & Design, 83 (2015) 670-677.
[148] H. Li, S. Zhang, Z. Yi, J. Li, A. Sun, J. Guo, G. Xu, Bonding quality and fracture analysis of polyamide 12 parts fabricated by fused deposition modeling, Rapid Prototyping Journal, (2017).
[149] A.K. Ravi, A. Deshpande, K.H. Hsu, An in-process laser localized pre-deposition heating approach to inter-layer bond strengthening in extrusion based polymer additive manufacturing, Journal of Manufacturing Processes, 24 (2016) 179-185.
[150] J. Wang, H. Xie, Z. Weng, T. Senthil, L. Wu, A novel approach to improve mechanical properties of parts fabricated by fused deposition modeling, Materials & Design, 105 (2016) 152-159.
[151] J.F. Rodríguez, J.P. Thomas, J.E. Renaud, Mechanical behavior of acrylonitrile butadiene styrene (ABS) fused deposition materials. Experimental investigation, Rapid Prototyping Journal, (2001).
[152] S. Costa, F. Duarte, J. Covas, Thermal conditions affecting heat transfer in FDM/FFE: a contribution towards the numerical modelling of the process: This paper investigates convection, conduction and radiation phenomena in the filament deposition process, Virtual and Physical Prototyping, 10(1) (2015) 35-46.

[153] P.-H. Lee, H. Chung, S.W. Lee, J. Yoo, J. Ko, Dimensional accuracy in additive manufacturing processes, in: ASME 2014 International Manufacturing Science and Engineering Conference collocated with the JSME 2014 International Conference on Materials and Processing and the 42nd North American Manufacturing Research Conference, American Society of Mechanical Engineers Digital Collection, 2014.
[154] W. Wu, P. Geng, J. Zhao, Y. Zhang, D. Rosen, H. Zhang, Manufacture and thermal deformation analysis of semicrystalline polymer polyether ether ketone by 3D printing, Materials Research Innovations, 18(sup5) (2014) S5-12-S15-16.
[155] A. Armillotta, M. Bellotti, M. Cavallaro, Warpage of FDM parts: Experimental tests and analytic model, Robotics and Computer-Integrated Manufacturing, 50 (2018) 140-152.
[156] T.-M. Wang, J.-T. Xi, Y. Jin, A model research for prototype warp deformation in the FDM process, The International Journal of Advanced Manufacturing Technology, 33(11-12) (2007) 1087-1096.
[157] Y. Zhang, K. Chou, A parametric study of part distortions in fused deposition modelling using three-dimensional finite element analysis, Proceedings of the Institution of Mechanical Engineers, Part B: Journal of Engineering Manufacture, 222(8) (2008) 959-968.
[158] Y. Zhang, Y. Chou, Three-dimensional finite element analysis simulations of the fused deposition modelling process, Proceedings of the Institution of Mechanical Engineers, Part B: Journal of Engineering Manufacture, 220(10) (2006) 1663-1671.
[159] A. Kantaros, D. Karalekas, Fiber Bragg grating based investigation of residual strains in ABS parts fabricated by fused deposition modeling process, Materials & Design, 50 (2013) 44-50.
[160] O.A. Mohamed, S.H. Masood, J.L. Bhowmik, Experimental investigation of creep deformation of part processed by fused deposition modeling using definitive screening design, Additive Manufacturing, 18 (2017) 164-170.
[161] T.W. Kerekes, H. Lim, W.Y. Joe, G.J. Yun, Characterization of process–deformation/damage property relationship of fused deposition modeling (FDM) 3D-printed specimens, Additive Manufacturing, 25 (2019) 532-544.
[162] G. Alaimo, S. Marconi, L. Costato, F. Auricchio, Influence of meso-structure and chemical composition on FDM 3D-printed parts, Composites Part B: Engineering, 113 (2017) 371-380.
[163] C. Theunissen, M. Kimpen, CHIMIA Report/Company News.
[164] S.-S. Yao, F.-L. Jin, K.Y. Rhee, D. Hui, S.-J. Park, Recent advances in carbon-fiber-reinforced thermoplastic composites: A review, Composites Part B: Engineering, 142 (2018) 241-250.
[165] A.D. Valino, J.R.C. Dizon, A.H. Espera Jr, Q. Chen, J. Messman, R.C. Advincula, Advances in 3D printing of thermoplastic polymer composites and nanocomposites, Progress in Polymer Science, (2019) 101162.
[166] I. Gibson, D.W. Rosen, B. Stucker, Additive manufacturing technologies, Springer, 2014.
[167] D. Bourell, J.P. Kruth, M. Leu, G. Levy, D. Rosen, A.M. Beese, A. Clare, Materials for additive manufacturing, CIRP Annals, 66(2) (2017) 659-681.
[168] J. Frketic, T. Dickens, S. Ramakrishnan, Automated manufacturing and processing of fiber-reinforced polymer (FRP) composites: An additive review of contemporary and modern techniques for advanced materials manufacturing, Additive Manufacturing, 14 (2017) 69-86.
[169] M. Spoerk, C. Holzer, J. Gonzalez-Gutierrez, Material extrusion-based additive manufacturing of polypropylene: A review on how to improve dimensional inaccuracy and warpage, Journal of Applied Polymer Science, 137(12) (2020) 48545.

[170] S. Wojtyła, P. Klama, T. Baran, Is 3D printing safe? Analysis of the thermal treatment of thermoplastics: ABS, PLA, PET, and nylon, Journal of occupational and environmental hygiene, 14(6) (2017) D80-D85.
[171] M. Rinaldi, T. Ghidini, F. Cecchini, A. Brandao, F. Nanni, Additive layer manufacturing of poly (ether ether ketone) via FDM, Composites Part B: Engineering, 145 (2018) 162-172.
[172] K.-j. Cheng, Y.-f. Liu, R. Wang, J.-x. Zhang, X.-f. Jiang, X.-t. Dong, X. Xu, Topological optimization of 3D printed bone analog with PEKK for surgical mandibular reconstruction, Journal of the Mechanical Behavior of Biomedical Materials, (2020) 103758.
[173] M. Spoerk, F. Arbeiter, I. Raguž, G. Weingrill, T. Fischinger, G. Traxler, S. Schuschnigg, L. Cardon, C. Holzer, Polypropylene Filled With Glass Spheres in Extrusion-Based Additive Manufacturing: Effect of Filler Size and Printing Chamber Temperature, Macromolecular Materials and Engineering, 303(7) (2018) 1800179.
[174] R. Zaldivar, D. Witkin, T. McLouth, D. Patel, K. Schmitt, J. Nokes, Influence of processing and orientation print effects on the mechanical and thermal behavior of 3D-Printed ULTEM® 9085 Material, Additive Manufacturing, 13 (2017) 71-80.
[175] G. Cicala, G. Ognibene, S. Portuesi, I. Blanco, M. Rapisarda, E. Pergolizzi, G. Recca, Comparison of Ultem 9085 used in fused deposition modelling (FDM) with polytherimide blends, Materials, 11(2) (2018) 285.
[176] S. Gantenbein, K. Masania, W. Woigk, J.P. Sesseg, T.A. Tervoort, A.R. Studart, Three-dimensional printing of hierarchical liquid-crystal-polymer structures, Nature, 561(7722) (2018) 226-230.
[177] U. Kalsoom, P.N. Nesterenko, B. Paull, Recent developments in 3D printable composite materials, RSC advances, 6(65) (2016) 60355-60371.
[178] D. Depuydt, M. Balthazar, K. Hendrickx, W. Six, E. Ferraris, F. Desplentere, J. Ivens, A.W. Van Vuure, Production and characterization of bamboo and flax fiber reinforced polylactic acid filaments for fused deposition modeling (FDM), Polymer Composites, 40(5) (2019) 1951-1963.
[179] V.K. Balla, K.H. Kate, J. Satyavolu, P. Singh, J.G.D. Tadimeti, Additive manufacturing of natural fiber reinforced polymer composites: Processing and prospects, Composites Part B: Engineering, (2019) 106956.
[180] A.G. Facca, M.T. Kortschot, N. Yan, Predicting the tensile strength of natural fibre reinforced thermoplastics, Composites Science and Technology, 67(11-12) (2007) 2454-2466.
[181] D. Stoof, K. Pickering, Sustainable composite fused deposition modelling filament using recycled pre-consumer polypropylene, Composites Part B: Engineering, 135 (2018) 110-118.
[182] G.D. Goh, Y.L. Yap, S. Agarwala, W.Y. Yeong, Recent progress in additive manufacturing of fiber reinforced polymer composite, Advanced Materials Technologies, 4(1) (2019) 1800271.
[183] E.A. Papon, A. Haque, Fracture toughness of additively manufactured carbon fiber reinforced composites, Additive Manufacturing, 26 (2019) 41-52.
[184] F. Ning, W. Cong, J. Qiu, J. Wei, S. Wang, Additive manufacturing of carbon fiber reinforced thermoplastic composites using fused deposition modeling, Composites Part B: Engineering, 80 (2015) 369-378.
[185] M. Chapiro, Current achievements and future outlook for composites in 3D printing, Reinforced Plastics, 60(6) (2016) 372-375.

[186] R.T.L. Ferreira, I.C. Amatte, T.A. Dutra, D. Bürger, Experimental characterization and micrography of 3D printed PLA and PLA reinforced with short carbon fibers, Composites Part B: Engineering, 124 (2017) 88-100.
[187] Y. Arao, S. Yumitori, H. Suzuki, T. Tanaka, K. Tanaka, T. Katayama, Mechanical properties of injection-molded carbon fiber/polypropylene composites hybridized with nanofillers, Composites Part A: Applied Science and Manufacturing, 55 (2013) 19-26.
[188] H.L. Tekinalp, V. Kunc, G.M. Velez-Garcia, C.E. Duty, L.J. Love, A.K. Naskar, C.A. Blue, S. Ozcan, Highly oriented carbon fiber–polymer composites via additive manufacturing, Composites Science and Technology, 105 (2014) 144-150.
[189] L.G. Blok, M.L. Longana, H. Yu, B.K. Woods, An investigation into 3D printing of fibre reinforced thermoplastic composites, Additive Manufacturing, 22 (2018) 176-186.
[190] R.-M. Wang, S.-R. Zheng, Y.G. Zheng, Polymer matrix composites and technology, Elsevier, 2011.
[191] S. Mortazavian, A. Fatemi, Effects of fiber orientation and anisotropy on tensile strength and elastic modulus of short fiber reinforced polymer composites, Composites part B: engineering, 72 (2015) 116-129.
[192] C. Duty, J. Failla, S. Kim, T. Smith, J. Lindahl, V. Kunc, Z-Pinning approach for 3D printing mechanically isotropic materials, Additive Manufacturing, 27 (2019) 175-184.
[193] A. Le Duigou, M. Castro, R. Bevan, N. Martin, 3D printing of wood fibre biocomposites: From mechanical to actuation functionality, Materials & Design, 96 (2016) 106-114.
[194] G. Sodeifian, S. Ghaseminejad, A.A. Yousefi, Preparation of polypropylene/short glass fiber composite as Fused Deposition Modeling (FDM) filament, Results in Physics, 12 (2019) 205-222.
[195] W. Zhong, F. Li, Z. Zhang, L. Song, Z. Li, Short fiber reinforced composites for fused deposition modeling, Materials Science and Engineering: A, 301(2) (2001) 125-130.
[196] D. Filgueira, S. Holmen, J.K. Melbø, D. Moldes, A.T. Echtermeyer, G. Chinga-Carrasco, Enzymatic-assisted modification of thermomechanical pulp fibers to improve the interfacial adhesion with poly (lactic acid) for 3D printing, ACS Sustainable Chemistry & Engineering, 5(10) (2017) 9338-9346.
[197] J. Karger-Kocsis, H. Mahmood, A. Pegoretti, Recent advances in fiber/matrix interphase engineering for polymer composites, Progress in Materials Science, 73 (2015) 1-43.
[198] S. Keszei, S. Matkó, G. Bertalan, P. Anna, G. Marosi, A. Toth, Progress in interface modifications: from compatibilization to adaptive and smart interphases, European Polymer Journal, 41(4) (2005) 697-705.
[199] F.R. Jones, Interphase in Fiber-Reinforced Composites, Wiley encyclopedia of composites, (2011) 1-6.
[200] A.N. Netravali, K.L. Mittal, Fiber surface treatment: Relevance to interfacial characteristics, Wiley encyclopedia of composites, (2011) 1-19.
[201] F. Ning, W. Cong, Y. Hu, H. Wang, Additive manufacturing of carbon fiber-reinforced plastic composites using fused deposition modeling: Effects of process parameters on tensile properties, Journal of Composite Materials, 51(4) (2017) 451-462.
[202] A. Anwer, H.E. Naguib, Multi-functional flexible carbon fiber composites with controlled fiber alignment using additive manufacturing, Additive Manufacturing, 22 (2018) 360-367.
[203] D. Jiang, D.E. Smith, Anisotropic mechanical properties of oriented carbon fiber filled polymer composites produced with fused filament fabrication, Additive Manufacturing, 18 (2017) 84-94.
[204] L.J. Love, V. Kunc, O. Rios, C.E. Duty, A.M. Elliott, B.K. Post, R.J. Smith, C.A. Blue, The importance of carbon fiber to polymer additive manufacturing, Journal of Materials Research, 29(17) (2014) 1893-1898.

[205] M. Shofner, F.J. Rodríguez-Macías, R. Vaidyanathan, E.V. Barrera, Single wall nanotube and vapor grown carbon fiber reinforced polymers processed by extrusion freeform fabrication, Composites Part A: Applied Science and Manufacturing, 34(12) (2003) 1207-1217.

[206] M. Shofner, K. Lozano, F. Rodríguez-Macías, E. Barrera, Nanofiber-reinforced polymers prepared by fused deposition modeling, Journal of applied polymer science, 89(11) (2003) 3081-3090.

[207] W. Zhang, C. Cotton, J. Sun, D. Heider, B. Gu, B. Sun, T.-W. Chou, Interfacial bonding strength of short carbon fiber/acrylonitrile-butadiene-styrene composites fabricated by fused deposition modeling, Composites Part B: Engineering, 137 (2018) 51-59.

[208] T. Hofstätter, I.W. Gutmann, T. Koch, D.B. Pedersen, G. Tosello, G. Heinz, H.N. Hansen, Distribution and orientation of carbon fibers in polylactic acid parts produced by fused deposition modeling, in: ASPE Summer Topical Meeting 2016, ASPE–The American Society for Precision Engineering, 2016.

[209] V. Kishore, X. Chen, C. Ajinjeru, A.A. Hassen, J.M. Lindahl, J. Failla, V. Kunc, C.E. Duty, Additive manufacturing of high performance semicrystalline thermoplastics and their composites, Oak Ridge National Lab.(ORNL), Oak Ridge, TN (United States), 2016.

[210] G. Liao, Z. Li, Y. Cheng, D. Xu, D. Zhu, S. Jiang, J. Guo, X. Chen, G. Xu, Y. Zhu, Properties of oriented carbon fiber/polyamide 12 composite parts fabricated by fused deposition modeling, Materials & Design, 139 (2018) 283-292.

[211] J. Naranjo-Lozada, H. Ahuett-Garza, P. Orta-Castañón, W.M. Verbeeten, D. Sáiz-González, Tensile properties and failure behavior of chopped and continuous carbon fiber composites produced by additive manufacturing, Additive Manufacturing, 26 (2019) 227-241.

[212] O.S. Carneiro, A. Silva, R. Gomes, Fused deposition modeling with polypropylene, Materials & Design, 83 (2015) 768-776.

[213] R.W. Gray, D.G. Baird, J.H. Bøhn, Effects of processing conditions on short TLCP fiber reinforced FDM parts, Rapid Prototyping Journal, (1998).

[214] A.R.T. Perez, D.A. Roberson, R.B. Wicker, Fracture surface analysis of 3D-printed tensile specimens of novel ABS-based materials, Journal of Failure Analysis and Prevention, 14(3) (2014) 343-353.

[215] F. Calignano, D. Manfredi, E.P. Ambrosio, S. Biamino, M. Lombardi, E. Atzeni, A. Salmi, P. Minetola, L. Iuliano, P. Fino, Overview on additive manufacturing technologies, Proceedings of the IEEE, 105(4) (2017) 593-612.

[216] S.-H. Park, B.-K. Kang, J.E. Lee, S.W. Chun, K. Jang, Y.H. Kim, M.A. Jeong, Y. Kim, K. Kang, N.K. Lee, Design and fabrication of a thin-walled free-form scaffold on the basis of medical image data and a 3D printed template: its potential use in bile duct regeneration, ACS applied materials & interfaces, 9(14) (2017) 12290-12298.

[217] S.J. Park, J.E. Lee, J.H. Park, N.K. Lee, M.-Y. Lyu, K. Park, M.S. Koo, S.H. Cho, Y. Son, S.-H. Park, Enhanced solubility of the support in an FDM-based 3D printed structure using hydrogen peroxide under ultrasonication, Advances in Materials Science and Engineering, 2018 (2018).

[218] E. Pei, C. Duran, V. Subbian, M.T. Giovanetti, J.R. Simkins, F.R. Beyette Jr, Experimental desktop 3D printing using dual extrusion and water-soluble polyvinyl alcohol, Rapid Prototyping Journal, (2015).

[219] C.C. Kuo, Y.C. Tsou, B.C. Chen, Enhancing the efficiency of removing support material from rapid prototype parts, Materialwissenschaft und Werkstofftechnik, 43(3) (2012) 234-240.

[220] P.-C. Ma, N.A. Siddiqui, G. Marom, J.-K. Kim, Dispersion and functionalization of carbon nanotubes for polymer-based nanocomposites: a review, Composites Part A: Applied Science and Manufacturing, 41(10) (2010) 1345-1367.
[221] Z. Qin, Q.H. Qin, X.-Q. Feng, Mechanical property of carbon nanotubes with intramolecular junctions: Molecular dynamics simulations, Physics Letters A, 372(44) (2008) 6661-6666.
[222] W. Qiu, Q. Li, Z.-K. Lei, Q.H. Qin, W.-L. Deng, Y.-L. Kang, The use of a carbon nanotube sensor for measuring strain by micro-Raman spectroscopy, Carbon, 53 (2013) 161-168.
[223] Q. Rong, J. Wang, Y. Kang, Y. Li, Q.H. Qin, A damage mechanics model for twisted carbon nanotube fibers, Acta Mechanica Solida Sinica, 25(4) (2012) 342-347.
[224] Y.-H. Zeng, W.-G. Jiang, Q.H. Qin, Influence of helical rise on the self-excited oscillation behavior of zigzag@ zigzag double-wall carbon nanotubes, Acta Physica Sinica, 65(14) (2016) 148802.
[225] C. Vasile, M. Pascu, Practical guide to polyethylene, iSmithers Rapra Publishing, 2005.
[226] J.D. Menczel, R.B. Prime, Thermal analysis of polymers: fundamentals and applications, John Wiley & Sons, 2009.
[227] F. Li, Y. Hua, C.-B. Qu, J.-H. Ji, Y.-Q. Li, N. Hu, S.-Y. Fu, Effectively enhanced mechanical properties of injection molded short carbon fiber reinforced polyethersulfone composites by phenol-formaldehyde resin sizing, Composites Part B: Engineering, 139 (2018) 216-226.
[228] W. Luo, Q. Liu, Y. Li, S. Zhou, H. Zou, M. Liang, Enhanced mechanical and tribological properties in polyphenylene sulfide/polytetrafluoroethylene composites reinforced by short carbon fiber, Composites Part B: Engineering, 91 (2016) 579-588.
[229] Q. An, A.N. Rider, E.T. Thostenson, Hierarchical composite structures prepared by electrophoretic deposition of carbon nanotubes onto glass fibers, ACS applied materials & interfaces, 5(6) (2013) 2022-2032.
[230] B. Vieille, M. Chabchoub, C. Gautrelet, Influence of matrix ductility and toughness on strain energy release rate and failure behavior of woven-ply reinforced thermoplastic structures at high temperature, Composites Part B: Engineering, 132 (2018) 125-140.
[231] A. Godara, L. Gorbatikh, G. Kalinka, A. Warrier, O. Rochez, L. Mezzo, F. Luizi, A. Van Vuure, S. Lomov, I. Verpoest, Interfacial shear strength of a glass fiber/epoxy bonding in composites modified with carbon nanotubes, Composites Science and Technology, 70(9) (2010) 1346-1352.
[232] H. Cen, Y. Kang, Z. Lei, Q.H. Qin, W. Qiu, Micromechanics analysis of Kevlar-29 aramid fiber and epoxy resin microdroplet composite by Micro-Raman spectroscopy, Composite Structures, 75(1) (2006) 532-538.
[233] M. Sharma, S. Gao, E. Mäder, H. Sharma, L.Y. Wei, J. Bijwe, Carbon fiber surfaces and composite interphases, Composites Science and Technology, 102 (2014) 35-50.
[234] H. Guo, Y. Huang, L. Meng, L. Liu, D. Fan, D. Liu, Interface property of carbon fibers/epoxy resin composite improved by hydrogen peroxide in supercritical water, Materials Letters, 63(17) (2009) 1531-1534.
[235] V.P. Veedu, A. Cao, X. Li, K. Ma, C. Soldano, S. Kar, P.M. Ajayan, M.N. Ghasemi-Nejhad, Multifunctional composites using reinforced laminae with carbon-nanotube forests, Nature materials, 5(6) (2006) 457.
[236] V. Chandrasekaran, S. Advani, M. Santare, Role of processing on interlaminar shear strength enhancement of epoxy/glass fiber/multi-walled carbon nanotube hybrid composites, Carbon, 48(13) (2010) 3692-3699.

[237] Z. Fan, M.H. Santare, S.G. Advani, Interlaminar shear strength of glass fiber reinforced epoxy composites enhanced with multi-walled carbon nanotubes, Composites Part A: Applied science and manufacturing, 39(3) (2008) 540-554.
[238] L. Chang, Z. Zhang, Tribological properties of epoxy nanocomposites: Part II. A combinative effect of short carbon fibre with nano-TiO2, Wear, 260(7) (2006) 869-878.
[239] S. Zhao, L.S. Schadler, R. Duncan, H. Hillborg, T. Auletta, Mechanisms leading to improved mechanical performance in nanoscale alumina filled epoxy, Composites Science and Technology, 68(14) (2008) 2965-2975.
[240] C. Chen, A.B. Morgan, Mild processing and characterization of silica epoxy hybrid nanocomposite, Polymer, 50(26) (2009) 6265-6273.
[241] M.F. De Volder, S.H. Tawfick, R.H. Baughman, A.J. Hart, Carbon nanotubes: present and future commercial applications, science, 339(6119) (2013) 535-539.
[242] W. Qiu, Y.L. Kang, Z.K. Lei, Q.H. Qin, Q. Li, Q. Wang, Experimental study of the Raman strain rosette based on the carbon nanotube strain sensor, Journal of Raman Spectroscopy, 41(10) (2010) 1216-1220.
[243] M. Li, Y. Gu, Y. Liu, Y. Li, Z. Zhang, Interfacial improvement of carbon fiber/epoxy composites using a simple process for depositing commercially functionalized carbon nanotubes on the fibers, Carbon, 52 (2013) 109-121.
[244] T.-W. Chou, L. Gao, E.T. Thostenson, Z. Zhang, J.-H. Byun, An assessment of the science and technology of carbon nanotube-based fibers and composites, Composites Science and Technology, 70(1) (2010) 1-19.
[245] M. Kim, Y.-B. Park, O.I. Okoli, C. Zhang, Processing, characterization, and modeling of carbon nanotube-reinforced multiscale composites, Composites Science and Technology, 69(3-4) (2009) 335-342.
[246] X. He, F. Zhang, R. Wang, W. Liu, Preparation of a carbon nanotube/carbon fiber multi-scale reinforcement by grafting multi-walled carbon nanotubes onto the fibers, Carbon, 45(13) (2007) 2559-2563.
[247] D.-L. Shi, X.-Q. Feng, Y.Y. Huang, K.-C. Hwang, H. Gao, The effect of nanotube waviness and agglomeration on the elastic property of carbon nanotube-reinforced composites, Journal of Engineering Materials and Technology, 126(3) (2004) 250-257.
[248] A.M. Díez-Pascual, M. Naffakh, C. Marco, M.A. Gómez-Fatou, G.J. Ellis, Multiscale fiber-reinforced thermoplastic composites incorporating carbon nanotubes: A review, Current Opinion in Solid State and Materials Science, 18(2) (2014) 62-80.
[249] M. Alsawat, T. Altalhi, A. Santos, D. Losic, Facile and controllable route for nitrogen doping of carbon nanotubes composite membranes by catalyst-free chemical vapour deposition, Carbon, 106 (2016) 295-305.
[250] A.N. Rider, Q. An, N. Brack, E.T. Thostenson, A comparison of mechanical and electrical properties in hierarchical composites prepared using electrophoretic or chemical vapor deposition of carbon nanotubes, MRS Advances, 1(12) (2016) 785-790.
[251] K. Kepple, G. Sanborn, P. Lacasse, K. Gruenberg, W. Ready, Improved fracture toughness of carbon fiber composite functionalized with multi walled carbon nanotubes, Carbon, 46(15) (2008) 2026-2033.
[252] X. Yao, X. Gao, J. Jiang, C. Xu, C. Deng, J. Wang, Comparison of carbon nanotubes and graphene oxide coated carbon fiber for improving the interfacial properties of carbon fiber/epoxy composites, Composites Part B: Engineering, 132 (2018) 170-177.
[253] X. Sui, J. Shi, H. Yao, Z. Xu, L. Chen, X. Li, M. Ma, L. Kuang, H. Fu, H. Deng, Interfacial and fatigue-resistant synergetic enhancement of carbon fiber/epoxy hierarchical composites via an electrophoresis deposited carbon nanotube-toughened transition layer, Composites Part A: Applied Science and Manufacturing, 92 (2017) 134-144.

[254] Q. Zhang, J. Liu, R. Sager, L. Dai, J. Baur, Hierarchical composites of carbon nanotubes on carbon fiber: Influence of growth condition on fiber tensile properties, Composites Science and Technology, 69(5) (2009) 594-601.
[255] S.-B. Lee, O. Choi, W. Lee, J.-W. Yi, B.-S. Kim, J.-H. Byun, M.-K. Yoon, H. Fong, E.T. Thostenson, T.-W. Chou, Processing and characterization of multi-scale hybrid composites reinforced with nanoscale carbon reinforcements and carbon fibers, Composites Part A: Applied Science and Manufacturing, 42(4) (2011) 337-344.
[256] N.A. Siddiqui, E.L. Li, M.-L. Sham, B.Z. Tang, S.L. Gao, E. Mäder, J.-K. Kim, Tensile strength of glass fibres with carbon nanotube–epoxy nanocomposite coating: effects of CNT morphology and dispersion state, Composites Part A: Applied Science and Manufacturing, 41(4) (2010) 539-548.
[257] S. Gao, E. Mäder, R. Plonka, Nanostructured coatings of glass fibers: improvement of alkali resistance and mechanical properties, Acta Materialia, 55(3) (2007) 1043-1052.
[258] S.-L. Gao, E. Mäder, R. Plonka, Nanocomposite coatings for healing surface defects of glass fibers and improving interfacial adhesion, Composites Science and Technology, 68(14) (2008) 2892-2901.
[259] H. Zhang, Y. Liu, M. Kuwata, E. Bilotti, T. Peijs, Improved fracture toughness and integrated damage sensing capability by spray coated CNTs on carbon fibre prepreg, Composites Part A: Applied Science and Manufacturing, 70 (2015) 102-110.
[260] S.-Y. Fu, X.-Q. Feng, B. Lauke, Y.-W. Mai, Effects of particle size, particle/matrix interface adhesion and particle loading on mechanical properties of particulate–polymer composites, Composites Part B: Engineering, 39(6) (2008) 933-961.
[261] L.A. Savas, U. Tayfun, M. Dogan, The use of polyethylene copolymers as compatibilizers in carbon fiber reinforced high density polyethylene composites, Composites Part B: Engineering, 99 (2016) 188-195.
[262] M.S. Huda, L.T. Drzal, A.K. Mohanty, M. Misra, Chopped glass and recycled newspaper as reinforcement fibers in injection molded poly (lactic acid)(PLA) composites: a comparative study, Composites science and technology, 66(11-12) (2006) 1813-1824.
[263] J. Echeberria, N. Rodríguez, J. Vleugels, K. Vanmeensel, A. Reyes-Rojas, A. Garcia-Reyes, C. Dominguez-Rios, A. Aguilar-Elguezabal, M. Bocanegra-Bernal, Hard and tough carbon nanotube-reinforced zirconia-toughened alumina composites prepared by spark plasma sintering, Carbon, 50(2) (2012) 706-717.
[264] Y. Zhang, Y. Zhang, Y. Liu, X. Wang, B. Yang, A novel surface modification of carbon fiber for high-performance thermoplastic polyurethane composites, Applied Surface Science, 382 (2016) 144-154.
[265] N.G. Karsli, A. Aytac, Effects of maleated polypropylene on the morphology, thermal and mechanical properties of short carbon fiber reinforced polypropylene composites, Materials & Design, 32(7) (2011) 4069-4073.
[266] L. Wang, J. Qiu, E. Sakai, X. Wei, The relationship between microstructure and mechanical properties of carbon nanotubes/polylactic acid nanocomposites prepared by twin-screw extrusion, Composites Part A: Applied Science and Manufacturing, 89 (2016) 18-25.
[267] M.L. Manchado, L. Valentini, J. Biagiotti, J. Kenny, Thermal and mechanical properties of single-walled carbon nanotubes–polypropylene composites prepared by melt processing, Carbon, 43(7) (2005) 1499-1505.
[268] Y. Zhao, Y. Gu, M. Li, Z. Zhang, Double vacuum assisted resin infusion molding and property of carbon nanotubeglass fiber/epoxy resin laminates, Fuhe Cailiao Xuebao(Acta Materiae Compositae Sinica), 28(3) (2011) 13-19.

[269] V. Dikshit, A. Nagalingam, Y. Yap, S. Sing, W. Yeong, J. Wei, Investigation of quasi-static indentation response of inkjet printed sandwich structures under various indenter geometries, Materials, 10(3) (2017) 290.
[270] C. Chu, G. Graf, D.W. Rosen, Design for additive manufacturing of cellular structures, Computer-Aided Design and Applications, 5(5) (2008) 686-696.
[271] X. Wang, M. Jiang, Z. Zhou, J. Gou, D. Hui, 3D printing of polymer matrix composites: A review and prospective, Composites Part B: Engineering, 110 (2017) 442-458.
[272] H. Gu, C. Ma, J. Gu, J. Guo, X. Yan, J. Huang, Q. Zhang, Z. Guo, An overview of multifunctional epoxy nanocomposites, Journal of Materials Chemistry C, 4(25) (2016) 5890-5906.
[273] K.V. Wong, A. Hernandez, A review of additive manufacturing, ISRN Mechanical Engineering, 2012 (2012).
[274] Y. AbouHashem, M. Dayal, S. Savanah, G. Štrkalj, The application of 3D printing in anatomy education, Medical education online, 20(1) (2015) 29847.
[275] S. Derakhshanfar, R. Mbeleck, K. Xu, X. Zhang, W. Zhong, M. Xing, 3D bioprinting for biomedical devices and tissue engineering: A review of recent trends and advances, Bioactive materials, 3(2) (2018) 144-156.
[276] J. Chacón, M.A. Caminero, E. García-Plaza, P.J. Núñez, Additive manufacturing of PLA structures using fused deposition modelling: Effect of process parameters on mechanical properties and their optimal selection, Materials & Design, 124 (2017) 143-157.
[277] J. Saroia, Y. Wang, Q. Wei, M. Lei, X. Li, Y. Guo, K. Zhang, A review on 3D printed matrix polymer composites: its potential and future challenges, The International Journal of Advanced Manufacturing Technology, 106(5-6) (2020) 1695-1721.
[278] Q.-S. Yang, Q.H. Qin, Fiber interactions and effective elasto-plastic properties of short-fiber composites, Composite structures, 54(4) (2001) 523-528.
[279] Q.-S. Yang, Q.H. Qin, Modelling the effective elasto-plastic properties of unidirectional composites reinforced by fibre bundles under transverse tension and shear loading, Materials Science and Engineering: A, 344(1-2) (2003) 140-145.
[280] H. Wang, Q.H. Qin, Y. Xiao, Special n-sided Voronoi fiber/matrix elements for clustering thermal effect in natural-hemp-fiber-filled cement composites, International Journal of Heat and Mass Transfer, 92 (2016) 228-235.
[281] S. Tsai, Introduction to composite materials, Routledge, 2018.
[282] Q.-S. Yang, Q.H. Qin, X.-R. Peng, Size effects in the fiber pullout test, Composite structures, 61(3) (2003) 193-198.
[283] I. Cooperstein, E. Sachyani-Keneth, E. Shukrun-Farrell, T. Rosental, X. Wang, A. Kamyshny, S. Magdassi, Hybrid Materials for Functional 3D Printing, Advanced Materials Interfaces, 5(22) (2018).
[284] G.C. Pidcock, M. in het Panhuis, Extrusion printing of flexible electrically conducting carbon nanotube networks, Advanced Functional Materials, 22(22) (2012) 4790-4800.
[285] S.J. Leigh, R.J. Bradley, C.P. Purssell, D.R. Billson, D.A. Hutchins, A simple, low-cost conductive composite material for 3D printing of electronic sensors, PloS one, 7(11) (2012) e49365.
[286] R.M. Jones, Mechanics of composite materials, CRC press, 2014.
[287] M. Milosevic, D. Stoof, K. Pickering, Characterizing the mechanical properties of fused deposition modelling natural fiber recycled polypropylene composites, Journal of Composites Science, 1(1) (2017) 7.
[288] S. Waheed, J.M. Cabot, P. Smejkal, S. Farajikhah, S. Sayyar, P.C. Innis, S. Beirne, G. Barnsley, T.W. Lewis, M.C. Breadmore, Three-Dimensional Printing of Abrasive, Hard, and Thermally Conductive Synthetic Microdiamond–Polymer Composite Using

Low-Cost Fused Deposition Modeling Printer, ACS applied materials & interfaces, 11(4) (2019) 4353-4363.
[289] G.D. Goh, V. Dikshit, A.P. Nagalingam, G.L. Goh, S. Agarwala, S.L. Sing, J. Wei, W.Y. Yeong, Characterization of mechanical properties and fracture mode of additively manufactured carbon fiber and glass fiber reinforced thermoplastics, Materials & Design, 137 (2018) 79-89.
[290] B.G. Compton, B.K. Post, C.E. Duty, L. Love, V. Kunc, Thermal analysis of additive manufacturing of large-scale thermoplastic polymer composites, Additive Manufacturing, 17 (2017) 77-86.
[291] L. Cao, Q.H. Qin, N. Zhao, An RBF–MFS model for analysing thermal behaviour of skin tissues, International Journal of Heat and Mass Transfer, 53(7) (2010) 1298-1307.
[292] H. Wang, Q.H. Qin, Meshless approach for thermo-mechanical analysis of functionally graded materials, Engineering Analysis with Boundary Elements, 32(9) (2008) 704-712.
[293] J. Wang, L. Yuan, L. Wang, Y. Cui, Q.H. Qin, Numerical study on helical fiber fragmentation in chiral biological materials, Transactions of Tianjin University, 24(1) (2018) 51-58.
[294] N. Zhao, L.-L. Cao, Q.H. Qin, Application of Trefftz Method to Heat Conduction Problem in Functionally Graded Materials, Recent Patents on Space Technology, 1(2) (2011) 158-166.
[295] H. Wang, Q.H. Qin, Some problems with the method of fundamental solution using radial basis functions, Acta Mechanica Solida Sinica, 20(1) (2007) 21-29.
[296] L.-L. Cao, Q.H. Qin, N. Zhao, A new RBF-Trefftz meshless method for partial differential equations, in: IOP Conference Series: Materials Science and Engineering, IOP Publishing, 2010, pp. 012217.
[297] C.-Y. Lee, H. Wang, Q.H. Qin, Method of fundamental solutions for 3D elasticity with body forces by coupling compactly supported radial basis functions, Engineering Analysis with Boundary Elements, 60 (2015) 123-136.
[298] X. Zheng, H. Lee, T.H. Weisgraber, M. Shusteff, J. DeOtte, E.B. Duoss, J.D. Kuntz, M.M. Biener, Q. Ge, J.A. Jackson, Ultralight, ultrastiff mechanical metamaterials, Science, 344(6190) (2014) 1373-1377.
[299] C. Huang, L. Chen, Negative Poisson's ratio in modern functional materials, Advanced Materials, 28(37) (2016) 8079-8096.
[300] K. Cai, J. Luo, Y. Ling, J. Wan, Q.H. Qin, Effects of size and surface on the auxetic behaviour of monolayer graphene kirigami, Scientific Reports, 6 (2016) 35157.
[301] H. Wang, Y. Zhang, W. Lin, Q.H. Qin, A novel two-dimensional mechanical metamaterial with negative Poisson’s ratio, Computational Materials Science, 171 (2020) 109232.
[302] X. Ren, R. Das, P. Tran, T.D. Ngo, Y.M. Xie, Auxetic metamaterials and structures: A review, Smart materials and structures, 27(2) (2018) 023001.
[303] G.N. Greaves, A. Greer, R.S. Lakes, T. Rouxel, Poisson's ratio and modern materials, Nature materials, 10(11) (2011) 823.
[304] K.E. Evans, A. Alderson, Auxetic materials: functional materials and structures from lateral thinking!, Advanced materials, 12(9) (2000) 617-628.
[305] Y. Yao, Y. Luo, Y. Xu, B. Wang, J. Li, H. Deng, H. Lu, Fabrication and characterization of auxetic shape memory composite foams, Composites Part B: Engineering, 152 (2018) 1-7.
[306] K.K. Saxena, R. Das, E.P. Calius, Three decades of auxetics research− materials with negative Poisson's ratio: a review, Advanced Engineering Materials, 18(11) (2016) 1847-1870.

[307] R.S. Lakes, Negative-Poisson's-ratio materials: auxetic solids, Annual review of materials research, 47 (2017) 63-81.
[308] N. Grimmelsmann, H. Meissner, A. Ehrmann, 3D printed auxetic forms on knitted fabrics for adjustable permeability and mechanical properties, in: IOP Conference Series: Materials Science and Engineering, IOP Publishing, 2016, pp. 012011.
[309] H.M. Kolken, A. Zadpoor, Auxetic mechanical metamaterials, RSC Advances, 7(9) (2017) 5111-5129.
[310] A. Clausen, F. Wang, J.S. Jensen, O. Sigmund, J.A. Lewis, Topology optimized architectures with programmable Poisson's ratio over large deformations, Advanced Materials, 27(37) (2015) 5523-5527.
[311] M. Sanami, N. Ravirala, K. Alderson, A. Alderson, Auxetic materials for sports applications, Procedia Engineering, 72 (2014) 453-458.
[312] S. Bhullar, H. Mawanane, A. Alderson, K. Alderson, B. Martin, Influence of negative Poisson's ratio on stent applications, Adv. Mater, 2(3) (2013) 42-47.
[313] Z. Wang, A. Zulifqar, H. Hu, Auxetic composites in aerospace engineering, in: Advanced composite materials for aerospace engineering, Elsevier, 2016, pp. 213-240.
[314] N. Novak, M. Vesenjak, Z. Ren, Auxetic cellular materials-a review, Strojniški vestnik-Journal of Mechanical Engineering, 62(9) (2016) 485-493.
[315] W. Voigt, Bestimmung der Elasticitätsconstanten für das chlorsaure Natron, Annalen der Physik, 285(8) (1893) 719-723.
[316] R. Lakes, Foam structures with a negative Poisson's ratio, Science, 235 (1987) 1038-1041.
[317] K.E. Evans, M. Nkansah, I. Hutchinson, S. Rogers, Molecular network design, Nature, 353(6340) (1991) 124.
[318] Y. Xue, W. Wang, F. Han, Enhanced compressive mechanical properties of aluminum based auxetic lattice structures filled with polymers, Composites Part B: Engineering, 171 (2019) 183-191.
[319] F. Wang, O. Sigmund, J.S. Jensen, Design of materials with prescribed nonlinear properties, Journal of the Mechanics and Physics of Solids, 69 (2014) 156-174.
[320] J.N. Grima, S. Winczewski, L. Mizzi, M.C. Grech, R. Cauchi, R. Gatt, D. Attard, K.W. Wojciechowski, J. Rybicki, Tailoring graphene to achieve negative Poisson's ratio properties, Advanced materials, 27(8) (2015) 1455-1459.
[321] Y. Jiang, Y. Li, 3D printed auxetic mechanical metamaterial with chiral cells and re-entrant cores, Scientific reports, 8(1) (2018) 1-11.
[322] Z. Wang, H. Hu, Auxetic materials and their potential applications in textiles, Textile Research Journal, 84(15) (2014) 1600-1611.
[323] C. Hu, J. Dong, J. Luo, Q.H. Qin, G. Sun, 3D printing of chiral carbon fiber reinforced polylactic acid composites with negative Poisson's ratios, Composites Part B: Engineering, 201 (2020) 108400.
[324] K. Alderson, V. Simkins, V. Coenen, P. Davies, A. Alderson, K. Evans, How to make auxetic fibre reinforced composites, physica status solidi (b), 242(3) (2005) 509-518.
[325] W. Miller, Z. Ren, C. Smith, K. Evans, A negative Poisson's ratio carbon fibre composite using a negative Poisson's ratio yarn reinforcement, Composites Science and Technology, 72(7) (2012) 761-766.
[326] J. Clarke, R. Duckett, P. Hine, I. Hutchinson, I. Ward, Negative Poisson's ratios in angle-ply laminates: theory and experiment, Composites, 25(9) (1994) 863-868.
[327] L. Zhou, J. Zeng, L. Jiang, H. Hu, Low-velocity impact properties of 3D auxetic textile composite, Journal of materials science, 53(5) (2018) 3899-3914.

[328] P. Subramani, S. Rana, D.V. Oliveira, R. Fangueiro, J. Xavier, Development of novel auxetic structures based on braided composites, Materials & Design, 61 (2014) 286-295.
[329] R. Magalhaes, P. Subramani, T. Lisner, S. Rana, B. Ghiassi, R. Fangueiro, D.V. Oliveira, P.B. Lourenco, Development, characterization and analysis of auxetic structures from braided composites and study the influence of material and structural parameters, Composites Part A: Applied Science and Manufacturing, 87 (2016) 86-97.
[330] P. Subramani, S. Rana, B. Ghiassi, R. Fangueiro, D.V. Oliveira, P.B. Lourenco, J. Xavier, Development and characterization of novel auxetic structures based on re-entrant hexagon design produced from braided composites, Composites Part B: Engineering, 93 (2016) 132-142.
[331] X.-T. Wang, Y.-L. Chen, L. Ma, The manufacture and characterization of composite three-dimensional re-entrant auxetic cellular structures made from carbon fiber reinforced polymer, Journal of Composite Materials, 52(23) (2018) 3265-3273.
[332] X.-T. Wang, B. Wang, Z.-H. Wen, L. Ma, Fabrication and mechanical properties of CFRP composite three-dimensional double-arrow-head auxetic structures, Composites Science and Technology, 164 (2018) 92-102.
[333] A. Vyatskikh, S. Delalande, A. Kudo, X. Zhang, C.M. Portela, J.R. Greer, Additive manufacturing of 3D nano-architected metals, Nature communications, 9(1) (2018) 593.
[334] J.T. Muth, P.G. Dixon, L. Woish, L.J. Gibson, J.A. Lewis, Architected cellular ceramics with tailored stiffness via direct foam writing, Proceedings of the National Academy of Sciences, 114(8) (2017) 1832-1837.
[335] X. Wu, Y. Su, J. Shi, Perspective of additive manufacturing for metamaterials development, Smart Materials and Structures, 28(9) (2019) 093001.
[336] J. Jirousek, Q.H. Qin, Application of hybrid-Trefftz element approach to transient heat conduction analysis, Computers & Structures, 58(1) (1996) 195-201.
[337] Q.H. Qin, Transient plate bending analysis by hybrid Trefftz element approach, Communications in Numerical Methods in Engineering, 12(10) (1996) 609-616.
[338] H. Wang, Q.H. Qin, Voronoi Polygonal Hybrid Finite Elements and Their Applications, in: Current Trends in Mathematical Analysis and Its Interdisciplinary Applications, Springer, 2019, pp. 521-563.
[339] H. Wang, Q.H. Qin, A Numerical Method for Analysing Heat Conduction in Composites Containing Encapsulated Phase Change Materials, in: MATEC Web of Conferences, EDP Sciences, 2018, pp. 02012.
[340] Q.H. Qin, Y.-W. Mai, S.-W. Yu, Some problems in plane thermopiezoelectric materials with holes, International Journal of Solids and Structures, 36(3) (1999) 427-439.
[341] Q.H. Qin, Y.-W. Mai, S.-W. Yu, Effective moduli for thermopiezoelectric materials with microcracks, International Journal of Fracture, 91(4) (1998) 359-371.
[342] Q.H. Qin, Y.-W. Mai, A closed crack tip model for interface cracks in thermopiezoelectric materials, International Journal of Solids and Structures, 36(16) (1999) 2463-2479.
[343] Q.H. Qin, Y.-W. Mai, Thermoelectroelastic Green's function and its application for bimaterial of piezoelectric materials, Archive of Applied Mechanics, 68(6) (1998) 433-444.
[344] Q.H. Qin, Y. Mai, Crack growth prediction of an inclined crack in a half-plane thermopiezoelectric solid, Theoretical and Applied Fracture Mechanics, 26(3) (1997) 185-191.
[345] Q.H. Qin, Advanced mechanics of piezoelectricity, in, Higher Education Press and Springer, Beijing, 2013.

[346] Q.H. Qin, Thermoelectroelastic Green's function for a piezoelectric plate containing an elliptic hole, Mechanics of Materials, 30(1) (1998) 21-29.
[347] G. Sun, X. Liu, G. Zheng, Z. Gong, Q. Li, On fracture characteristics of adhesive joints with dissimilar materials–An experimental study using digital image correlation (DIC) technique, Composite Structures, 201 (2018) 1056-1075.
[348] M. Dhanasekar, K.Y. Wang, Q.H. Qin, Y.L. Kang, Contact analysis using Trefftz and interface finite elements, Computer Assisted Mechanics and Engineering Sciences, 13(3) (2006) 457-471.
[349] H. Wang, Q.H. Qin, Hybrid FEM with fundamental solutions as trial functions for heat conduction simulation, Acta Mechanica Solida Sinica, 22(5) (2009) 487-498.
[350] H. Wang, Q.H. Qin, Fundamental solution-based hybrid finite element analysis for non-linear minimal surface problems, Recent Developments in Boundary Element Methods: A Volume to Honour Professor John T. Katsikadelis, (2010) 309.
[351] H. Wang, Q.H. Qin, W. Yao, Improving accuracy of opening-mode stress intensity factor in two-dimensional media using fundamental solution based finite element model, Australian Journal of Mechanical Engineering, 10(1) (2012) 41-52.
[352] D.Y. Fozdar, P. Soman, J.W. Lee, L.H. Han, S. Chen, Three-dimensional polymer constructs exhibiting a tunable negative Poisson's ratio, Advanced functional materials, 21(14) (2011) 2712-2720.
[353] A. Ingrole, A. Hao, R. Liang, Design and modeling of auxetic and hybrid honeycomb structures for in-plane property enhancement, Materials & Design, 117 (2017) 72-83.
[354] M. Lei, W. Hong, Z. Zhao, C. Hamel, M. Chen, H. Lu, H.J. Qi, 3D printing of auxetic metamaterials with digitally reprogrammable shape, ACS applied materials & interfaces, 11(25) (2019) 22768-22776.
[355] J. Dong, Q.H. Qin, Y. Xiao, Nelder-Mead optimization of elastic metamaterials via machine-learning-aided surrogate modelling, International Journal of Applied Mechanics, 12(1) (2020) 2050011.